



**Aircraft and Rotorcraft Pilot Couplings – Tools and Techniques for Alleviation and Detection**

**ACPO-GA-2010-266073**

**Deliverable No. D5.1  
Design guidelines for A/RPC prevention**

Contractual delivery date:  
September/2013

Actual delivery date:  
September/2013

Partner responsible for the Deliverable: ONERA

Author(s):

Marilena D. Pavel (TUD), Deniz Yilmaz (TUD),  
Binh Dang-Vu (ONERA),  
Pierangelo Masarati, Giuseppe Quaranta (POLIMI),  
Massimo Gennaretti, Jacopo Serafini (UROMA3),  
Michael Jump, Lu Linghai, Michael Jones (UoL),  
Hafid Smaili (NLR),  
Achim Ionita, Andreea Afloare (STRAERO),  
Larisa Zaichik (TsAGI)

Dissemination level		
PU	Public	
PP	Restricted to other programme participants (including the Commission Services)	
RE	Restricted to a group specified by the consortium (including the Commission Services)	
CO	Confidential, only for members of the consortium (including the Commission Services)	X



## Document Information Table

<b>Grant agreement no.</b>	ACPO-GA-2010-266073
<b>Project full title</b>	ARISTOTEL – Aircraft and Rotorcraft Pilot Couplings – Tools and Techniques for Alleviation and Detection
<b>Deliverable number</b>	D5.1
<b>Deliverable title</b>	Design guidelines for A/RPC prevention
<b>Nature</b>	R <sup>1</sup>
<b>Dissemination level</b>	CO <sup>2</sup>
<b>Version</b>	1.0
<b>Work package number</b>	WP5
<b>Work package leader</b>	NLR
<b>Partner responsible for Deliverable</b>	ONERA
<b>Reviewer(s)</b>	

The research leading to these results has received funding from the European Community's Seventh Framework Programme (FP7/2007-2013) under grant agreement n° 266073.

The author is solely responsible for its content, it does not represent the opinion of the European Community and the Community is not responsible for any use that might be made of data appearing therein.

<sup>1</sup> **R**=Report, **P**=Prototype, **D**=Demonstrator, **O**=Other

<sup>2</sup> **PU**=Public, **PP**=Restricted to other programme participants (including the Commission Services), **RE**=Restricted to a group specified by the consortium (including the Commission Services), **CO**=Confidential, only for members of the consortium (including the Commission Services)

## Revision Table

Version	Date	Modified Page/Section	Author(s)	Comments
1.0	15.09.13		Binh Dang-Vu	
2.0	30.09.2013		See list	
2.1	4.10.2013	Revision	MD Pavel	

## Executive Summary

In this report, a synthesis of the main results deduced from pilot-vehicle system modelling and prediction criteria for both rigid-body and aero-elastic A/RPC is performed and completed by a sensitivity analysis of the critical design parameters of the pilot-vehicle system. The results are converted into guidelines to help designers to assess, early in the design process, the flying qualities, biodynamic effects and susceptibility of new aircraft/rotorcraft to adverse A/RPCs.

## Table of Contents

Document Information Table .....	2
Revision Table .....	3
Executive Summary .....	3
1. Introduction .....	5
2. Current design guidelines for A/RPC prevention .....	5
3. Updated/additional design guidelines for A/RPC prevention.....	10
3.1 Design considerations for rigid-body RPC prevention .....	11
3.2 Design considerations for aeroelastic RPC prevention.....	12
3.3 Design considerations for aeroelastic APC prevention .....	13
4. Conclusion .....	14
5. References.....	14
6. List of Abbreviations.....	15
Appendix A: Design space investigation for handling qualities (TUD).....	16
Appendix B: Sensitivity analysis of RPC to design parameters (ONERA).....	29
Appendix C: Robust Stability Analysis of RPC sensitivity to pilot biodynamic feedthrough and design parameters (POLIMI) .....	48
Appendix D: Pilot-Vehicle System modelling requirements and RPC/PAO sensitivity to structural parameters (UROMA3) .....	72
Appendix E: A general methodology for boundary-triggered PIO investigations (UoL) .....	87
Appendix F: Aero-servo-elastic RPC criteria investigation (STRAERO).....	103
Appendix G: Design guidelines for APC prevention (TsAGI, in cooperation with NLR) .....	118

## 1. Introduction

An objective of the ARISTOTEL project is to provide guidelines to designers and simulator programs to reveal A/RPC aspects of new aircraft/rotorcraft to be designed [1]. For this purpose, a synthesis of the main results deduced from pilot-vehicle system modelling and prediction criteria for both rigid-body and aero-elastic A/RPC [2, 3] is performed, and it is completed by a sensitivity analysis of the critical design parameters of the pilot-vehicle system. The results are converted into guidelines to help designers to assess, early in the design process, the flying qualities, biodynamic effects and susceptibility of new aircraft/rotorcraft to adverse A/RPCs. The guidelines concern the conceptual/preliminary design phases of the aircraft/rotorcraft development which are the early phases where the manufacturer has still considerable freedom to modify the aircraft/rotorcraft design without strong influences on cost. The aerodynamic characteristics, actuator performance, or flight control system structure may be modified, since the final configuration has not been frozen at that time.

Section 2 presents the current design guidelines for A/RPC prevention.

Section 3 presents revised or additional guidance derived from ARISTOTEL work, the explanatory material being detailed in previous deliverables and in the additional appendices included in this report.

## 2. Current design guidelines for A/RPC prevention

The ARISTOTEL consortium organized two workshops, on March 9<sup>th</sup> 2011 in Milan and on October 5<sup>th</sup> 2011 in Salon de Provence, where rotorcraft manufacturers were asked how they address adverse RPC in the design process. The trend is that the manufacturers have a “*certain degree of knowledge about the problem but do not design rotorcraft to particularly avoid RPC*”. Difficulties in obtaining information on design practices are due to handling qualities design being kept as in-house know-how by manufacturers, and RPC characteristics of rotorcraft being treated by industry as proprietary or classified performance data. For this reason, this report presents only the design guidelines for A/RPC prevention that can be found in the literature. They are summarized herein and expressed rather in the form of general recommended processes [4], best practices [5] and recommendations [6].

Figure 1 from Ref. [4] shows a design process for avoiding adverse APC events. It is assumed that the same process can be extended to RPC events.

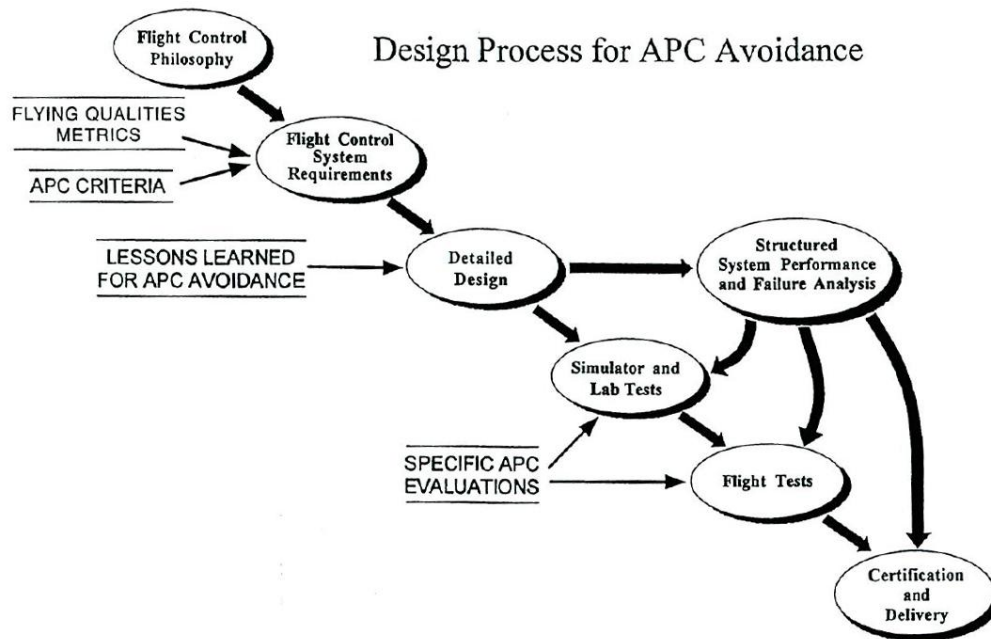


Figure 1: Design process for avoiding adverse APC events [4].

Prior to flight tests and certification, the steps in the process that focus on the elimination of adverse A/RPC events are:

- Establishing flight control philosophy and objectives
- Defining flying qualities requirements
- Detailed flight control design
- Structured analysis of system performance
- Simulation considerations.

The control philosophy may include for example the aircraft-pilot interface (inceptors, displays, etc.). Good handling qualities (HQ) defined in the form of requirements with relevant metrics are a primary condition to prevent A/RPC. To augment the design process, the list of HQ requirements should be completed with additional criteria and metrics that address specifically A/RPC. Once HQ requirements have been established, a well-structured process for developing control laws should be implemented. The next phase is the structured analysis of system performance where the effects on HQ of many factors are assessed in detail (flight conditions, aircraft loading, structural influences, etc.). Next, the simulators play a significant role in developing the flight control system (FCS) and reducing the risk of adverse A/RPC. A strong consensus exists on the importance of selecting simulation tasks for detecting A/RPC tendencies [7].

According to the AGARD Working Group 23 "Flight Control Design – Best Practices" [5], the best approach to minimise the probability of occurrence of in-flight accidents due to design errors, e.g. adverse pilot-vehicle coupling phenomena, is designing for good flying qualities, not designing particularly for PIO avoidance. However the Working Group concluded also that PIOs can be predicted to happen in flight by applying certain criteria and that a better approach is to prevent the

occurrence of PIOs by design. Figure 2 shows the design process of a flight control system as presented in Ref. [5].

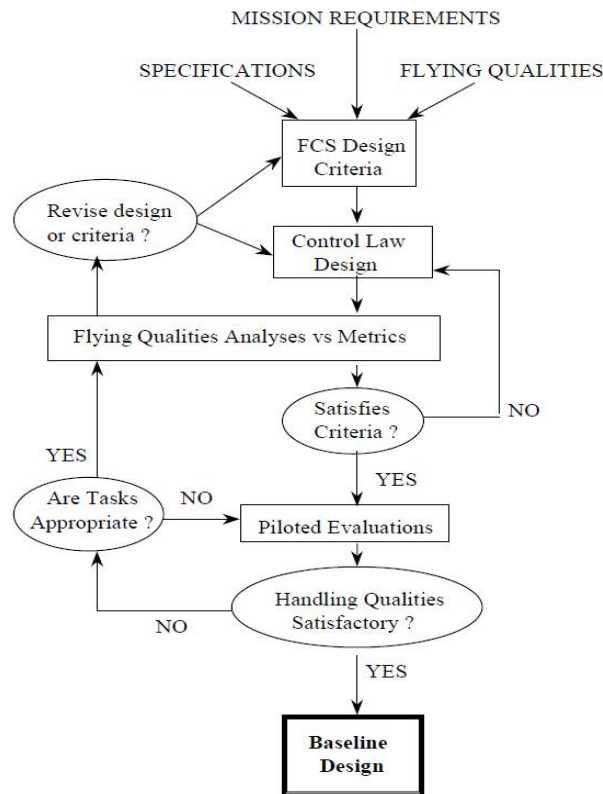


Figure 2: Flight control system design process [5].

It shows a logical process, starting with consideration of the various requirements, to establish a well-defined set of FCS design criteria. This is the point at which consideration of aero-servo-elasticity or nonlinearities for example should start. Design goals should be formulated such as to include appropriate structural dynamics models, to minimize phase delays caused by rate-limiting effects, etc. The loop of analyses ensures that the control law design meets the criteria that were established. As mentioned above, to augment the design process, the list of HQ requirements should be completed with additional criteria and metrics that address specifically A/RPC. Not all of the criteria are equally appropriate for all control designs and aircraft types. Each criterion can provide a piece of insights, but none is sufficient to predict with absolute accuracy the presence or absence of A/RPC. A mix of criteria should be used for design assessment [4]. A detailed description of these criteria can be found in Deliverable 2.6 [7].

The set of design guidelines established by AGARD WG23 is expressed in terms of desirable practices and presented in terms of flight control law design sub-processes under the following headings [5]:

1. Establishing the aerodynamic design and system performance requirements.
2. Modelling and analysis of the unaugmented vehicle.
3. Design criteria and flying qualities specifications.
4. Control laws design and development.
5. Control laws functional specification, implementation and verification.
6. Piloted simulation and handling qualities.
7. Aeroservoelasticity and structural mode filter design.
8. Design robustness and flight clearance.
9. Developments during flight testing.
10. Management aspects.

Although the application of the above best practices will help to avoid pilot involved oscillations, specific design considerations for PIO prevention were also given by the Working Group. The prevention of high order PIO can be summarised by the following: “the PIO frequency cannot be too high, the PIO gain cannot be too low, the phase delay cannot be too small, and the large amplitude response cannot be linearized too much”. The design considerations for Categories I, II and III PIO prevention are summarized below.

### **Category I PIO prevention**

The basic guidelines for control system design to prevent Cat. I PIO are:

- Proper shaping of both the feedback and feed-forward paths to provide good short-term response, irrespective of the long-term manoeuvre demand type, with a suitable compromise between K/s-like attitude control and satisfactory flight path control properties, depending on flight condition and task phase.
- Absolute minimisation of high order phase delay, which is very strongly, though not exclusively, dominated by the feed-forward path from stick to control actuator and which determines how well connected with the aircraft the pilot feels, through the angular acceleration response. This is coupled with maximising the attitude response frequency and minimising its gain at the 180-degree lag frequency.
- Proper manipulation of the command path gain to counter high gain feedback in manoeuvres at lower frequencies, to prevent excessive control deflections at higher frequencies where there is little or no feedback signal and particularly at the 180 degrees attitude phase lag frequency, and to ensure satisfactory response sensitivity.

### **Category II PIO prevention**

The basic guidelines for control system design to prevent Cat. II PIO are:

- It is essential to investigate the response in the region of 180 degrees attitude phase lag, with the maximum possible stick inputs, however unrealistic this may seem.
- The more the command path gain is attenuated at potential PIO frequencies, the less is the risk of control rate saturation. The control angles that can be demanded here should not exceed those typical of a normal mechanical control system, for example, and should be considerably less in many flight conditions.
- If large amplitude dynamic response changes are unavoidable, they should be limited as far as possible and should blend smoothly and gradually from the linear response.

- The provision of sufficient actuator rate capability to postpone rate saturation onset, up to or beyond the frequency for 180 degrees phase lag in the linear attitude response with cyclic stop-to-stop stick inputs, will essentially prevent Cat. II PIO altogether.

### **Category III PIO prevention**

It is considered that by eliminating Cat. I 1 and II, that Cat. III will not occur. This statement holds true for all known examples of PIO to date.

The above guidelines are applicable to rigid body aircraft. Design guidelines in relation to aeroelasticity were given by AGARD WG23 in the Section “Aeroservoelasticity and structural mode filter design” recalled below.

### **Aeroservoelasticity and structural mode filter design**

The application of modern high bandwidth flight control systems and advanced aerodynamic configurations has led to an increase in the levels of interaction between the airframe and its FCS. The aeroservoelasticity specialist has the task of defining a set of structural mode filters that provide sufficient attenuation of the structural mode content of motion feedback signals. For this aspect of the flight control law design process, the following best practices are identified:

- Sensors should be located to minimise structural mode pick-up and the sensor installation must follow good mechanical practice, with the sensors being rigidly mounted to the primary structure. Anti-vibration mountings should only be used if justified and proven.
- Good quality flexible aircraft models are required, supported by ground vibration testing and airframe/FCS ‘structural coupling’ ground testing. In-flight validation of the models is desirable if phase stabilisation of structural modes is necessary. Frequency sweep or similar methods, with high fidelity response measurement and recording facilities, are beneficial for identification during ground and flight testing. Highly automated test and analysis facilities are essential.
- Establish understandable guidelines and requirements for airframe/FCS structural mode attenuation. These must be agreed with the whole Integrated Project Team, including the customer.
- A balanced design of structural mode and rigid body control filters is needed, in order to optimise aircraft stability margins. This needs to take into account the conflicting requirements of controlling the aircraft’s rigid modes (a requirement to minimise the low frequency phase lag due to the structural mode filtering) and flexible modes (a requirement to provide sufficient attenuation at higher frequencies). The structural mode filtering needs to provide satisfactory attenuation for all fuel states, stores configurations and failure states, across the flight envelope and during ground operations. The definition of the maximum allowable end-to-end gains for the different control law feedback paths, from a structural coupling point of view, gives an early indication of problematic areas and allows the control law designer to include this as a constraint from the very beginning.
- Digital effects such as the frequency warping of notch filters and fold-back due to aliasing, need careful attention. A detailed understanding of the digital FCS is essential and knowledge of its interfaces with flight.

The GARTEUR Action Group HC-AG16 “Rigid Body and Aeroelastic Rotorcraft-Pilot Coupling (RPC) – Prediction Tools and Means for Prevention” [6], gave an overview of means for rigid body and aeroelastic RPC prevention including a short discussion about drawbacks and difficulties. Furthermore, attention was given to whether the means of interest allow retro-fit solutions.

### 3. Updated/additional design guidelines for A/RPC prevention

This section presents revised or additional design guidelines derived from ARISTOTEL work. A synthesis of the results obtained from WP1 to WP4 is performed and completed by a sensitivity analysis of the critical design parameters of the pilot-vehicle system. Apart from the work reported in the deliverables already issued, the additional contributions of the ARISTOTEL partners concern various topics of interest and are detailed in the appendices of the present report. Briefly,

- TUD: Investigation of effects of rotorcraft preliminary design parameters on Handling Qualities (HQ) and Bandwidth Phase Delay (BPD) criterion.
- ONERA: Sensitivity analysis of rigid-body Category II RPC to design parameters, using the Open Loop Onset Point (OLOP) criterion. Sensitivity analysis of aeroelastic RPC to design parameters using eigenvalues analysis.
- POLIMI: Application of Robust Stability Analysis (RSA) to assess the sensitivity of pilot-vehicle interaction to pilot biodynamic feedthrough (BDFT) and vehicle design parameters.
- UROMA3: Identification of modelling requirements for accurate and reliable RPC/PAO simulations. Analysis of critical parameters in terms of unfavourable rotorcraft-pilot coupling and aero-servo-elastic instabilities.
- UoL: General methodology for assessing the pilot-aircraft performance and susceptibility of the PIOs for a Point-Tracking (PT) dominant task subject to boundary constraints.
- STRAERO: Aero-servo-elastic RPC criteria investigation.
- TsAGI, in cooperation with NLR: Guidelines and methodologies for fixed-wing aircraft APC/PIO prevention and for pilot manipulator systems to prevent adverse biodynamical interference with the large aircraft dynamics.

A first observation is that the results are heterogeneous in the level of experimental validation. Some can be considered as design guidelines in the traditional sense, but some other pure theoretical results should be considered only as suggestions for design guidelines. For homogeneity purposes, the results are rather expressed in the following sections in terms of design considerations and presented under the following headings:

- Rigid-body RPC
- Aeroelastic RPC
- Aeroelastic APC

In each heading the design guidelines are organized into the following topic categories:

- Pilot-Vehicle System modelling
- Pilot-Vehicle coupling prediction
- Conceptual design

### 3.1 Design considerations for rigid-body RPC prevention

#### 3.1.1 Design considerations in relation to Pilot-vehicle system modelling

See Deliverable D4.6 [9]:

- Pilot models identified from simulator tests should be used in complement of existing models for rigid body RPC prediction.

See Appendix E:

- Modelling the Boundary-Avoidance Tracking (BAT) process can be improved by an extension of the Hess's pilot model.

#### 3.1.2 Design considerations in relation to RPC prediction

See Deliverable D4.10 [2]:

- Enhanced Real-time Oscillation Verifier (ROVER) should be used as a complementary algorithm to detect RPC;
- Phase Aggression Criterion (PAC) should be used as a complementary criterion to detect and predict RPC;
- Bifurcation analysis should be used as a complementary analysis technique to predict Category II RPC and BAT RPC.

#### 3.1.3 Design considerations in relation to Conceptual preliminary design

See Appendix A. In a design space based on a BO105 helicopter configuration, Handling Qualities (HQ) and Category I PIO assessment based on Bandwidth Phase Delay (BPD) reveals that:

- The lowest tip speed values and the lowest disc loading values have the best BPD based HQs;
- Good HQs are also predicted for configurations with low aspect ratios and low blade loading coefficients.

See Appendix B. In a design space based on a BO105 helicopter configuration, Category II PIO assessment based on Open Loop Onset Point (OLOP) reveals that:

- In the roll axis, hover is the dimensioning flight condition for determining the minimum rate limit;
- Lowest minimum rate limits are obtained for configurations with high tip speed values and high disc loading values;
- In the design process a compromise has to be found between good BPD handling qualities and low rate limits.

## 3.2 Design considerations for aeroelastic RPC prevention

### 3.2.1 Design considerations in relation to Pilot-vehicle system modelling

See Deliverable D4.4 [10]:

- Biodynamic pilot models identified from simulator tests should be used in complement of existing models for aeroelastic RPC prediction.

See Appendix D:

- Although widely-applied quasi-steady sectional rotor aerodynamic modelling yields helicopter dynamics and RPC/PAO simulations that are generally close to those obtained by more sophisticated aerodynamic solvers, some significant differences may appear in predicting critical behaviours: thus, for next generation helicopters design focused on RPC prevention, the application of accurate, three-dimensional, unsteady, interactional rotor aerodynamic modelling is suggested;
- Pilot workload may play a relevant role in pilot passive response to perturbation, and thus it has to be taken into account when modelling pilot behaviour for RPC/PAO stability analyses;
- The inclusion of active pilot modelling for PAO simulation purposes may be neglected, unless intensive actuation of automatic flight control system (AFCS) occurs.

See Appendix F:

- The advantage of the Hess structural pilot model compared to the crossover model is that it involves a refined observation of the human central nervous and neuromuscular systems. Compared with Bandwidth Phase Delay criterion, in the structural pilot model criterion the human pilot is tuned to the control system by means of the crossover frequency, so the assumption made for the gains in control system are less important for the predicted results.

### 3.2.2 Design considerations in relation to RPC prediction

See Appendix C. The application of Robust Stability Analysis (RSA) to increasingly complex models of helicopter collective bounce supports the following considerations:

- RSA highlights the dependence and sensitivity of rotorcraft models to pilot biodynamic feedthrough (BDFT);
- When an analytical BDFT model is used, sensitivity to specific parameters of the model can be evaluated;
- When numerical or experimental frequency response data are available, proneness to RPC can be assessed using a very simple and practical graphical approach.

See Appendix D:

- System eigenvalue analysis has been proven to be an efficient way to assess the overall RPC/PAO stability behaviour, especially for design purposes, even when complex rotor aerodynamic models are applied (with the support of a methodology for the identification of aeroelastic/aerodynamic rotor transfer functions);

- Nonlinear time-marching analysis should be introduced, anyway, for design verification purposes, in that capable to examine detailed effects that may play a non-marginal role in the occurrence of adverse RPC/PAO events.

### 3.2.3 Design considerations in relation to Conceptual preliminary design

See Appendix B. In a design space based on an IAR330 helicopter configuration, PAO assessment based on eigenvalue analysis reveals that:

- PAO via the collective control is worsened with high forward speed, low helicopter weight, high rotor speed, and low lead-lag damping;
- PAO via the collective control is little affected by blade chord and blade stiffness;
- No PAO via the lateral cyclic control is observed but flight mechanics modes of RPC are worsened with low forward speed, low rotor speed, and low lead-lag damping;
- Flight mechanics modes of RPC via the lateral cyclic control are little affected by helicopter weight, blade chord and blade stiffness.

See Appendix D:

- Airframe stiffness is a parameter that may significantly affect the RPC/PAO stability of helicopters: more rigid airframe tends to stabilize vertical bouncing (however, the opposite effect might be observed on some rotor modes);
- Airframe damping does not significantly affect RPC/PAO stability;
- Rotor stiffness barely affects vertical bouncing, while the introduction of a flap damper may be beneficial;
- Blade torsional compliance significantly affects RPC/PAO occurrence: rotors with rigid torsion blades tend to alleviate RPC/PAO instability;
- The modification of servoelastic system parameters scarcely affects RPC/PAO stability behaviour.

## 3.3 Design considerations for aeroelastic APC prevention

See Appendix G. A Manual is proposed to the aircraft designer to assess possible pilot rating worsening of the elastic aircraft at the first stages of its development:

- Handling quality criterion is developed which allows estimation, at the early stages of aircraft development, of the effect of the structural elasticity and other aircraft characteristics on HQ of an elastic aircraft;
- The HQ criterion is validated by experimental data received on flight simulator for the generic aircraft model with variation in a wide range of all aircraft characteristics, which can affect HQ of an elastic aircraft: structural elasticity characteristics (number of modes, their amplitude and frequency, roll control sensitivity, control inceptor types and feel system characteristics). Good agreement between the calculated and experimental data proves the validity of mathematical expressions in the HQ criterion and all assumptions made for the pilot model transfer functions used in the criterion;
- Biodynamical experiments showed that tendency to biodynamical interaction in the pilot-aircraft system is more pronounced in the control systems with a sidestick and center stick;
- For the control systems with sidesticks, the biodynamical effect of the high-frequency accelerations caused by aircraft structural elasticity can be reduced by introduction of the

additional damping into the sidestick loading system. (The conclusion can be addressed as well to the control systems with center sticks);

- The main ideas of the developed HQ criterion can be applied to different control axes and to different types of vehicle (including rotorcraft), since it is based on the fundamental principles of pilot's perception.

## 4. Conclusion

This report presents current design guidelines for A/RPC and additional design guidelines derived from ARISTOTEL work.

Concerning current design guidelines, difficulties in obtaining information on design practices are due to handling qualities design being kept as in-house know-how by manufacturers, and A/RPC characteristics of aircraft/rotorcraft being treated by industry as proprietary or classified performance data. Instead, only the design guidelines for A/RPC prevention that can be found in the literature have been presented in the report.

Concerning additional design guidelines, a synthesis of the main ARISTOTEL results deduced from pilot-vehicle system modelling and prediction criteria for both rigid-body and aero-elastic A/RPC is performed and completed by a sensitivity analysis of the critical design parameters of the pilot-vehicle system. Some results can be considered as design guidelines in the traditional sense, but some other pure theoretical results should be considered only as suggestions for design guidelines. For homogeneity purposes, the results are rather expressed in terms of design considerations. However, these considerations can help designers to assess, early in the design process, the flying qualities, biodynamic effects and susceptibility of new aircraft/rotorcraft to adverse A/RPCs.

## 5. References

- [1] ARISTOTEL, Annex I – Description of work, Jun. 2010.
- [2] ARISTOTEL, Report detailing the new/updated rigid body RPC prediction criteria, Deliverable D4.10, Aug. 2013.
- [3] ARISTOTEL, Validation of models and criteria for aero-servo elastic A/RPC predictions, Deliverable D4.11, Aug. 2013.
- [4] McRuer, D.T. et al., Aviation Safety and Pilot Control. Understanding and Preventing Unfavorable Pilot-Vehicle Interactions, ASEB National Research Council, National Academy Press, Washington D.C., 1997.
- [5] RTO, Flight Control Design – Best Practices, RTO-TR-029, Dec. 2000.

- [6] GARTEUR HC-AG16, Rigid Body and Aeroelastic Rotorcraft-Pilot Coupling (RPC) – Prediction Tools and Means for Prevention, TP No. 167, Oct. 2008.
- [7] ARISTOTEL, Simulation guidelines for A/RPC prediction, Deliverable D5.2, Sep. 2013.
- [8] ARISTOTEL, Initial database of RPC predictions, Deliverable D2.6, Jan. 2012.
- [9] ARISTOTEL, Simulator test data analysis of the 1st test campaign, Deliverable D4.6, Feb. 2013.
- [10] ARISTOTEL, Complete bio-dynamical test data analysis and critical review, Deliverable D4.4, Feb. 2013.

## 6. List of Abbreviations

AFCS	Automatic Flight Control System
APC	Aircraft Pilot Coupling
A/RPC	Aircraft/Rotorcraft Pilot Coupling
BAT	Boundary Avoidance Tracking
BDFT	BioDynamic FeedThrough
BPD	Bandwidth Phase Delay
FCS	Flight Control System
HQ	Handling Qualities
OLOP	Open Loop Onset Point
PAC	Phase Aggression Criterion
PAO	Pilot-Assisted Oscillations
PIO	Pilot-Induced Oscillation
PVS	Pilot Vehicle System
RSA	Robust Stability Analysis
ROVER	Real-time Oscillation Verifier
RPC	Rotorcraft Pilot Coupling
WG	Working Group
WP	Work Package

## Appendix A: Design space investigation for handling qualities (TUD)

This appendix describes the investigation of effects of rotorcraft preliminary design parameters on handling qualities and RPC criteria. The methodology of the investigation is summarized below.

### 1. Define the goal

Generally, RPC assessment of any vehicle is carried out at very late phases of the flight programs. Prior to RPC tests, the vehicle most likely has reached the final design step, during which software and avionics systems are utilized. However, combating with RPC tendencies with software features may not always be favourable, e.g. FBW adjustments may lead to severe PIOs [Ref. McRuer F-22 landing case]. After the detection of RPC tendencies, the correction could include expensive and long term modifications, which would treat the whole vehicle development program. Thus, any vehicle development program could definitely benefit from assessing the RPC tendency during the design process “as early as possible”.

Within the ARISTOTEL project, TUD was interested in investigating the preliminary rotorcraft design parameters from handling qualities and RPC perspective.

The research question was: ‘Which preliminary design parameters are effective on RPC tendencies of a rotorcraft design? ‘

### 2. Design envelope creation

A design envelope was first created while considering various parameter constraints. Table 1 shows the parameter boundaries and summary of the descriptions of these constraints [1] (as related to the BO105 helicopter). For example, Figure 1 depicts the disc loading interval that was used during the investigation.

Table 1. Design parameter envelope boundaries.

Design Parameters	Values	Constraint Descriptions
Aspect Ratio (-) $AR = \frac{R}{c}$	Min. 14	Aerodynamic performance (high induced drag)
	Max. 20	Structural efficiency
Solidity (-) $\sigma = \frac{Nc}{\pi R}$	Min. 0.06	Hover performance
	Max. 0.12	Manoeuvrability
Tip Speed (ft/s) $V_{tip} = \Omega R$	Min. 400	Compressibility, noise issues
	Max. 780	Retreating blade stall, autorotation issues
Disc Loading (kg/(m <sup>2</sup> )) $DL = \frac{W}{\pi R^2}$	Min. Figure 1	Rotor size
	Max. Figure 1	Autorotation landing capability
Blade Loading Coef. (-) $BL = \frac{Wg}{\rho NcR(\Omega R)^2}$	Min. 0.05	Structural efficiency
	Max. 0.1	Onset of blade stall, increase of vibratory loads

Table 2 shows the intervals of varied main rotor sizing parameters and gross weights.

Table 2. Design interval of independent parameters

Parameters		Min.	Max.
Radius (m)	$R$	3	7
Omega (rad/s)	$\Omega$	20	80
Weight (kg)	$W$	1500	3500
Number blades	$N$	3	5

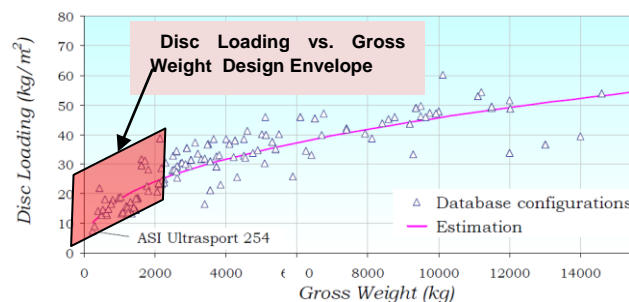


Figure 1 Disc loading design envelope with gross weight, plotted on the database configurations

An algorithm was developed to perform the sweep of main rotor parameters and rotorcraft weight within the assigned design interval which is listed in *Table 2*. After defining the design interval, a calculation loop swept from lower to higher values of each design interval, while storing the design points which satisfy the boundaries in *Table 1*. As a result, a subspace of satisfactory design points was obtained within the desired design constraints of *Table 1* and in *Table 2*. These envelopes practically guide the designer to elaborate any available design point for any helicopter within this design envelope.

The obtained design envelopes are shown in Figure 2 to Figure 4.

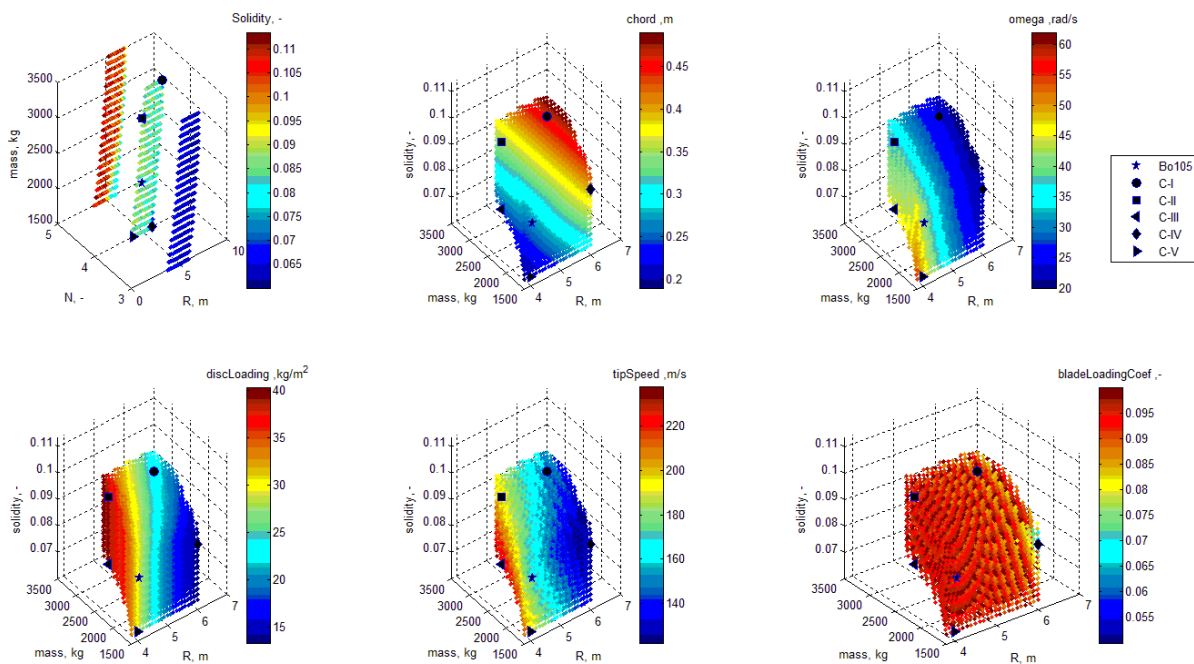


Figure 2 Design envelopes of N=4 blades configurations with five design points and BO105 parameters for reference.

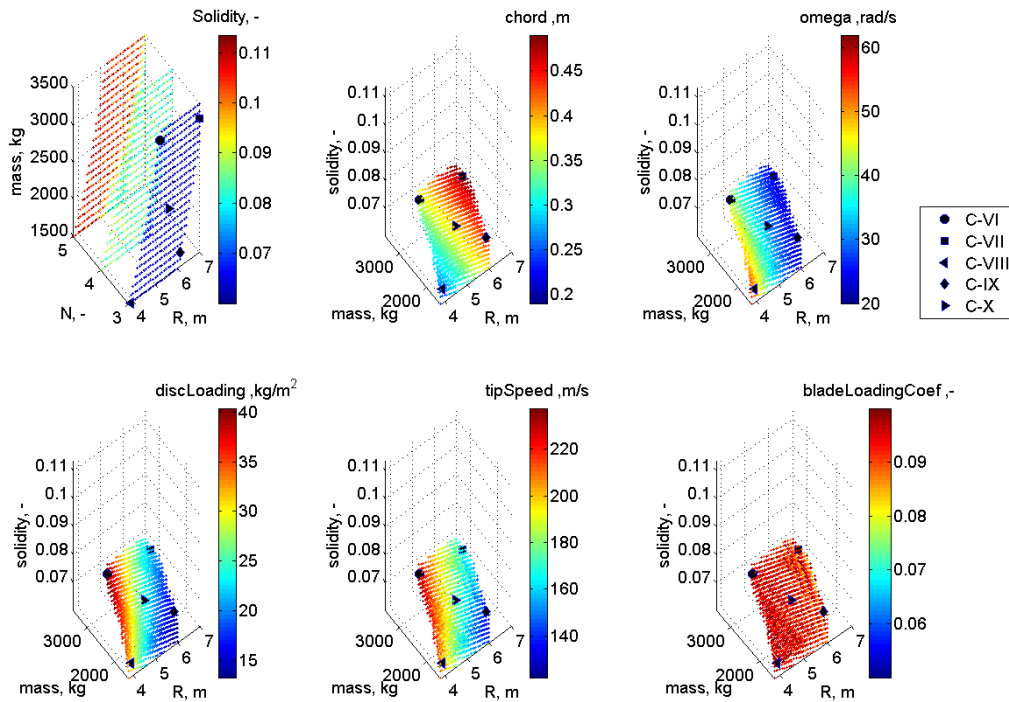


Figure 3 Design envelopes of N=3 blades configurations with five design points.

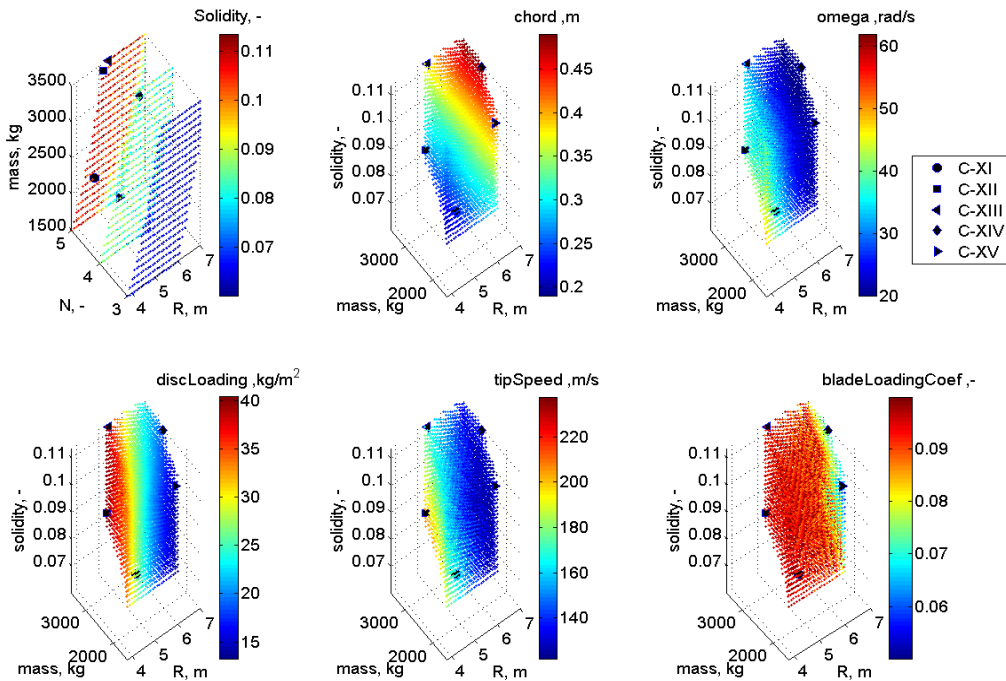


Figure 4 Design envelopes of N=5 blades configurations with five design points

Five design points for each number of blade configurations were selected, as shown in Figure 2 to Figure 4. Considering the solidity variation maps, five design points were chosen in order to represent the peaks of each parameter map.

### 3. Simulation model development

Figure 5 summarizes this procedure to obtain the frequency domain design model with varied preliminary design parameters. First, chosen design points were input to the simulation framework, step 1 in Figure 5.

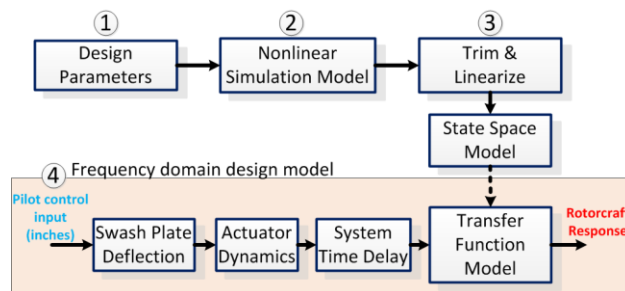


Figure 5 Flow chart of obtaining frequency domain rotorcraft models with varied design parameters.

As for step 2 in Figure 5, a non-linear BO105 simulation model was applied within ARISTOTEL project after being validated against flight test data [2]. This model was utilized by variable design parameter features. Then, this model was trimmed and linearized (as shown step 3 in Figure 5) and the resultant linearized 18 degree of model (body, rotor flap, lead-lag, inflow, and tail rotor states) were reduced to 8 degree of freedom (body states with coupled quasi-linear rotor states) models with adjustable design parameter options.

During the variation of design parameters such as those listed in Table 2 , physical dimensions of BO105 (except the rotor) were kept constant. Body inertias are scaled with respect to corresponding design weight. It was assumed that flight control system was able to provide the required trim control input for any design configuration.

According to ADS-33, velocities up to 45 knots are considered as low speed and higher velocities are categorized as forward speed [3]. Hence, linearized simulation models were obtained for hover, 30 and 60 knots, in order to cover fundamental velocity regimes. Then, linearized models were used to obtain state space model matrices, namely stability matrix A and control matrix B. This state space representation of the system inherently provides aerodynamic damping values in body axes. Moreover, transfer functions of this state space models were obtained in order to be used in frequency domain criteria analysis, as shown step 4 in Figure 5.

First order low pass filter structure was used to model the actuator dynamics, with a time constant of 0.04s [4]. During the transfer function model extraction of the simulation model, 200ms time delay was added to the whole helicopter system, in order to present a regular system delay in helicopters. Finally, step 4 in Figure 5 shows the block diagram of comprehensive frequency domain simulation model which includes aspects that were listed above.

In order to compare trim control inputs and Euler angles of all design configurations, Figure 6 is plotted with all chosen design point trim values.

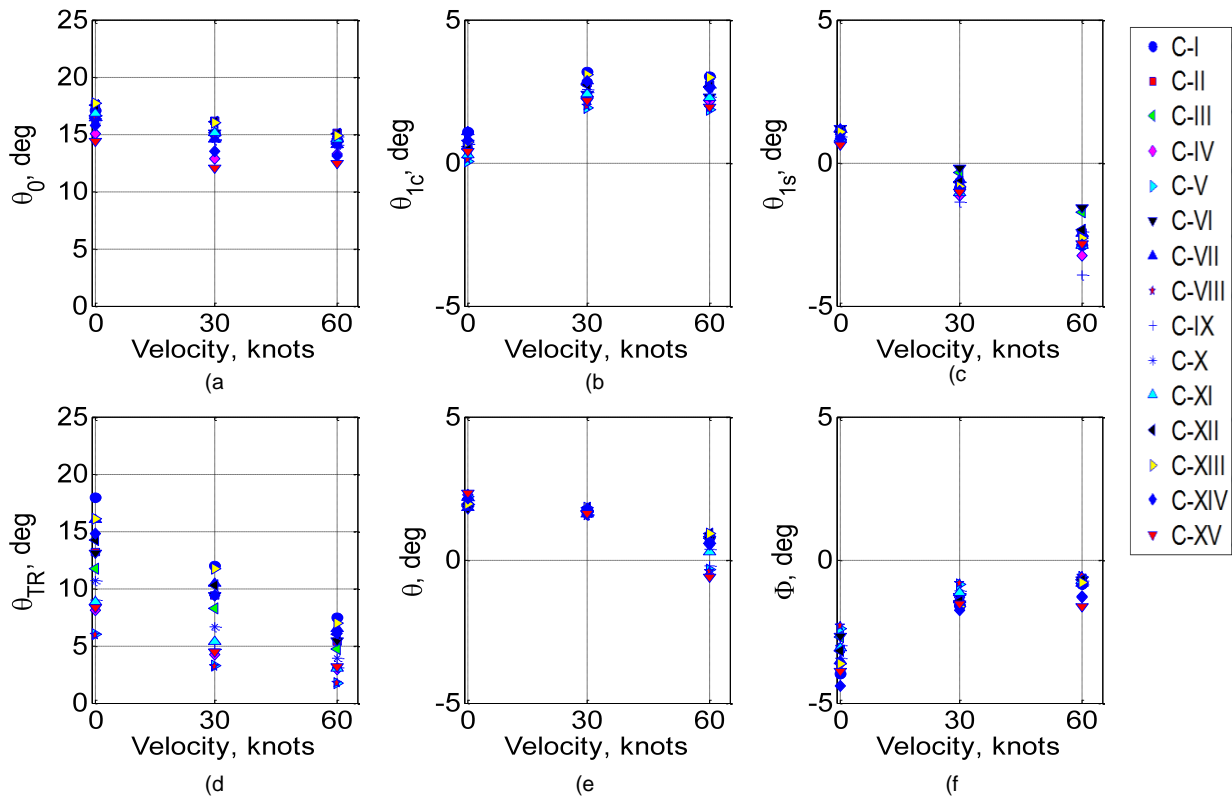


Figure 6 Design configuration trim values of four control inputs, which are collective (a), lateral (b) and longitudinal (c) wash plates, and pedal inputs (d), and Euler angles for pitch (e) and roll (f).

It was observed from Figure 6 that trim values were close enough to assume the full functionality of the flight control system for all configurations.

At this final stage, time and frequency domain representations of designed rotorcraft configurations were obtained to be used in RPC analysis methods, which will be discussed in following sections.

#### 4. Application of Bandwidth Phase Delay Criteria (BPD)

Design configurations, which were discussed in previous section, and their transfer function representations were used to calculate BPD of each configuration per axis. Pitch and roll axes are considered in this study, since varied preliminary design parameters were primarily effective on longitudinal and lateral response of the rotorcraft. Determinations of bandwidth of each design configuration are shown in Figure 7.

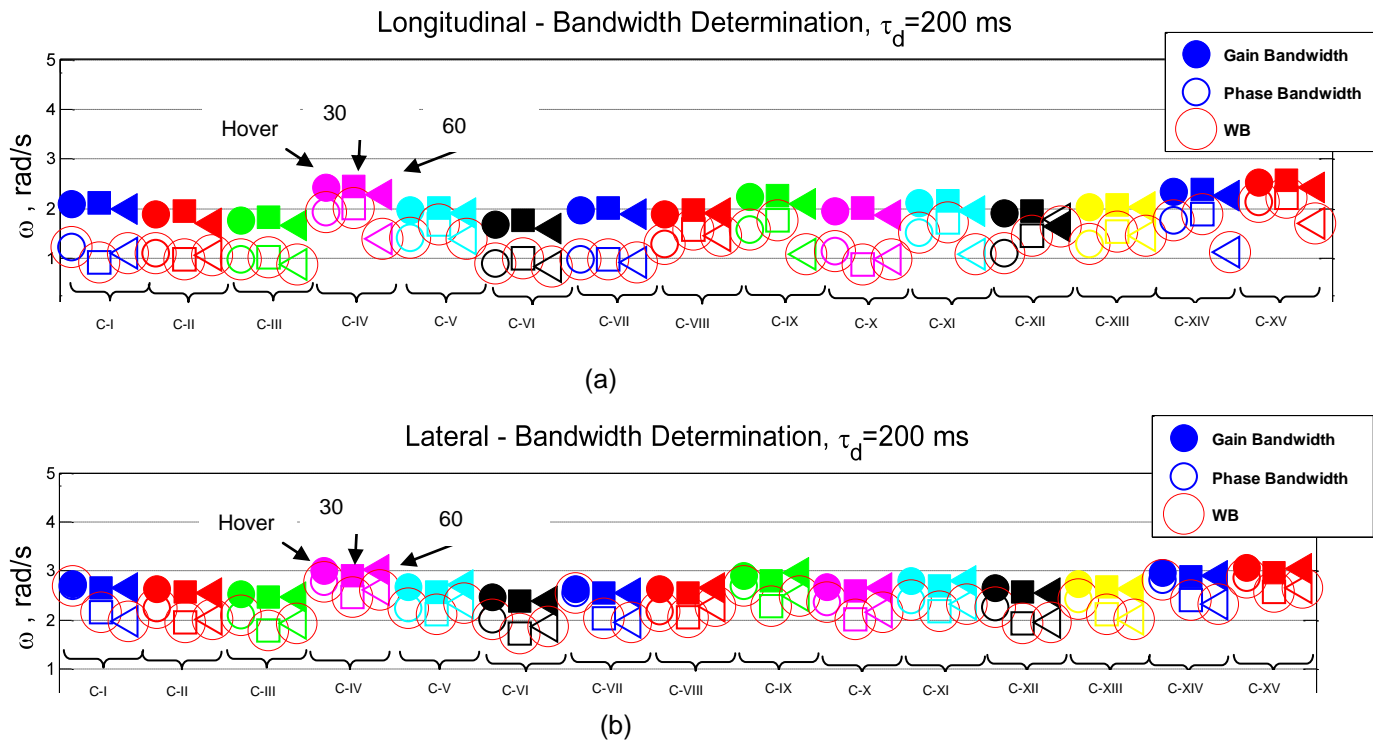
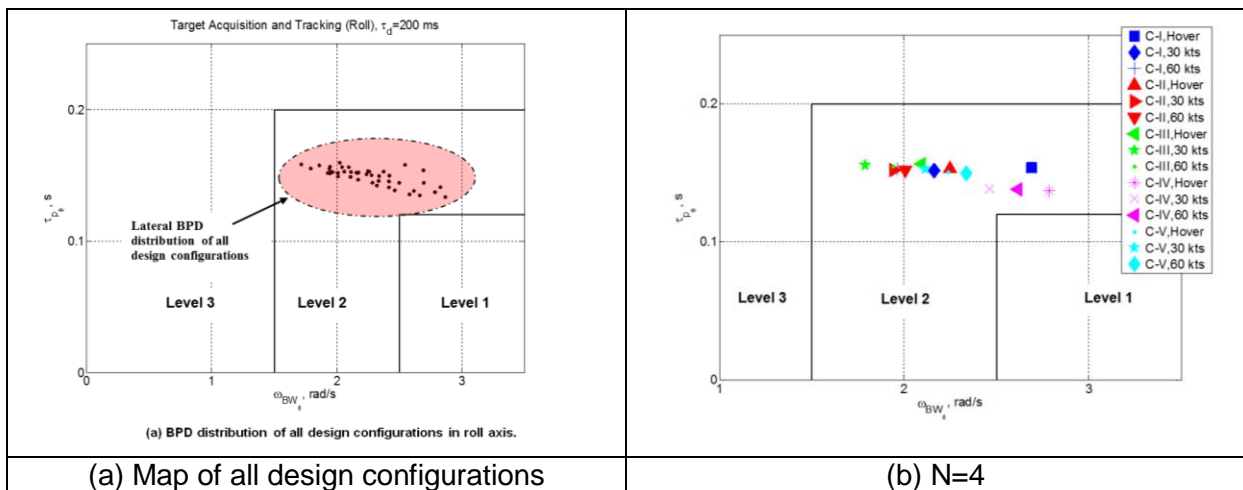
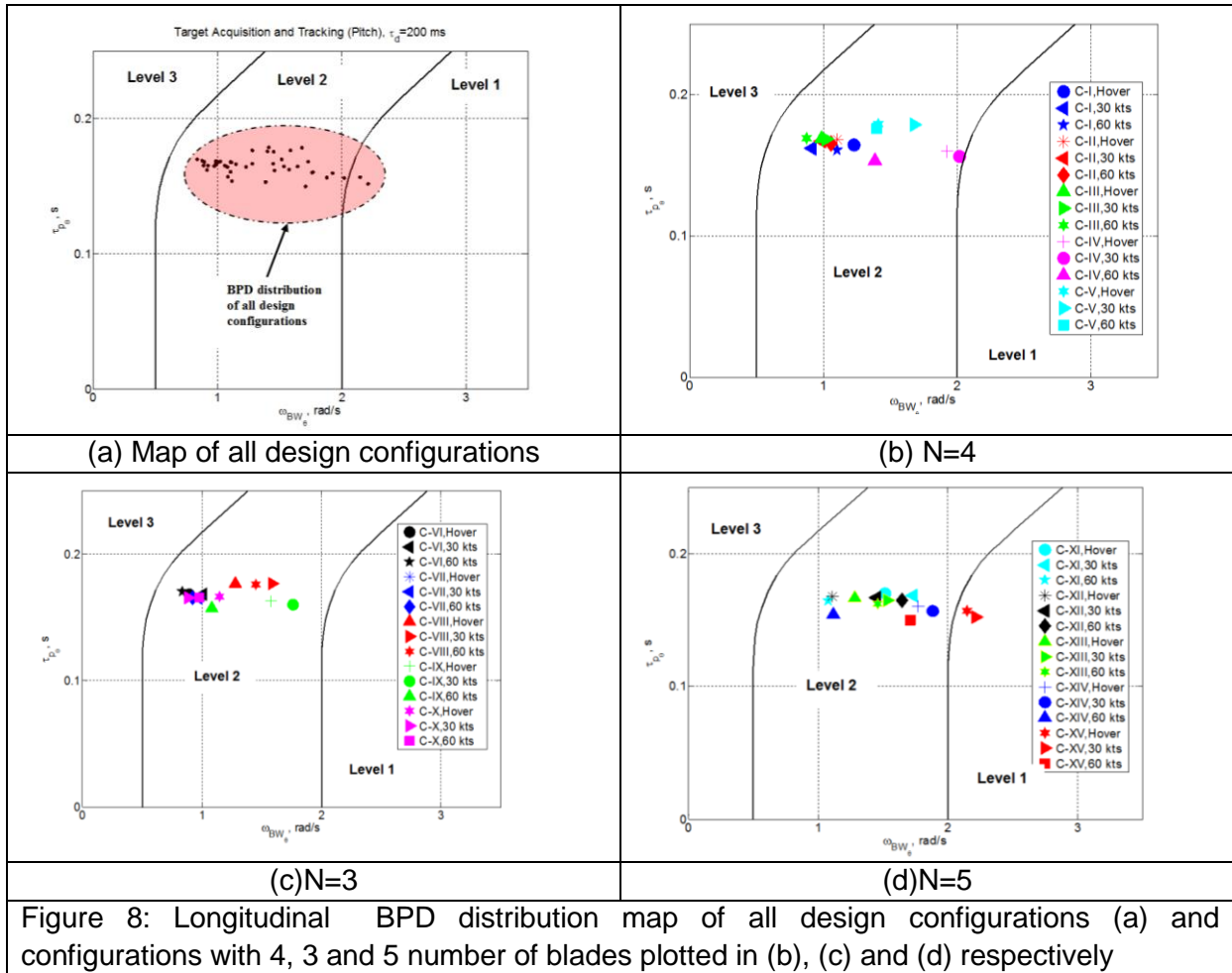


Figure 7: Longitudinal (a) and lateral (b) bandwidth determination of each design configuration. For each configuration circular, square and triangular markers present hover, 30 knots and 60 knots respectively.

It is clear from the Figure 7 that selected design configurations are phase limited such that lowest bandwidths are phase bandwidth values. Apart from the design configuration, one of the reasons for this could be the additional system time delay, which drops the phase at high frequencies for a first order rate command system.

Finally, longitudinal and lateral axes BPDs of design configurations are depicted in Figure 8 and Figure 9, longitudinal and lateral axis respectively. It can be seen from Figure 8 and Figure 9 that configuration C-XV has the best HQ and C-VI has the poorest HQ, according to BPD assessment of all configurations. It must be noted that majority of the configurations show Level-2 HQ. In this paper, 'better HQ' and 'poorer HQ' refer to being close to Level-1 and Level-3 boundaries respectively. In order to investigate the HQ and PIO sensitivity in more details, the configurations were chosen having the number of blades according to the best and poorer HQ. Configurations C-IV, C-IX and C-XV correspond to good HQ, while C-III, C-VI and C-XI have poor HQ.



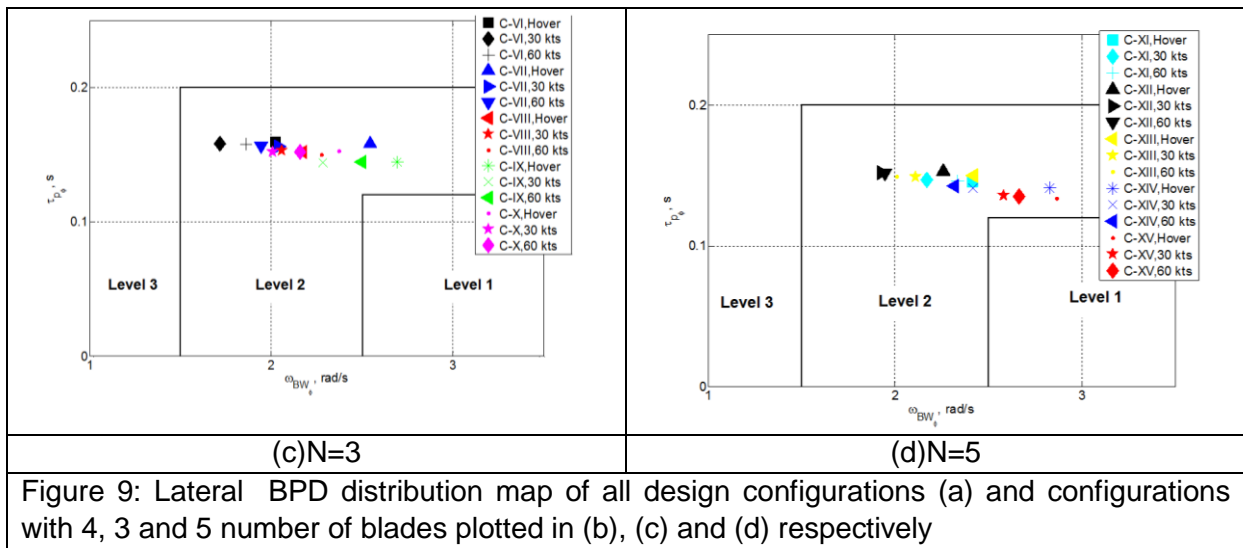
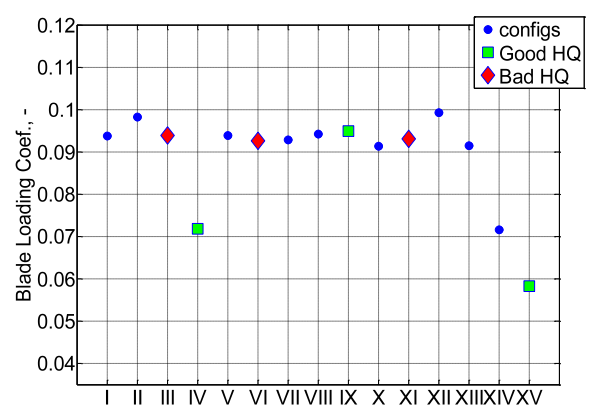
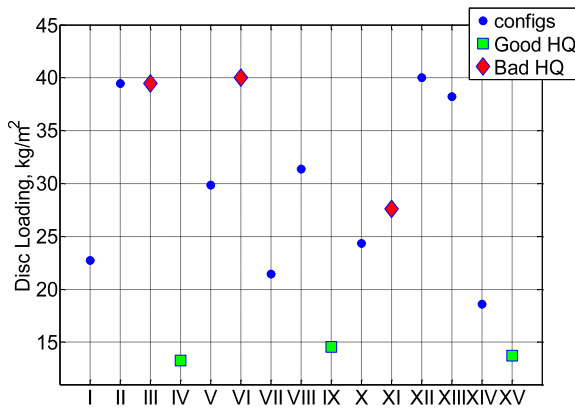
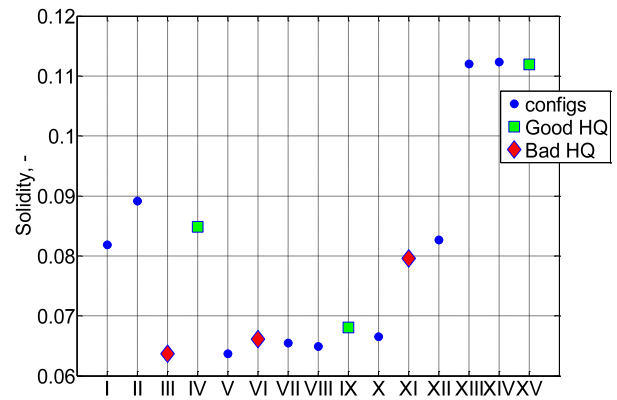
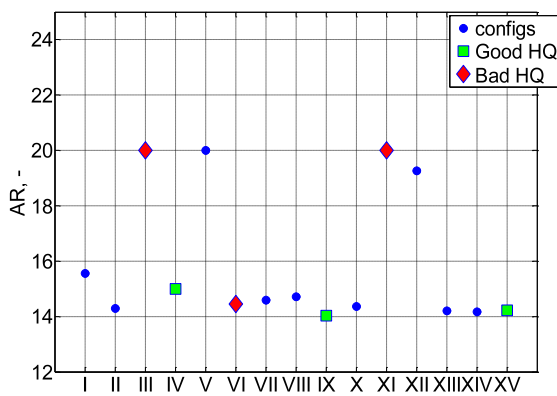
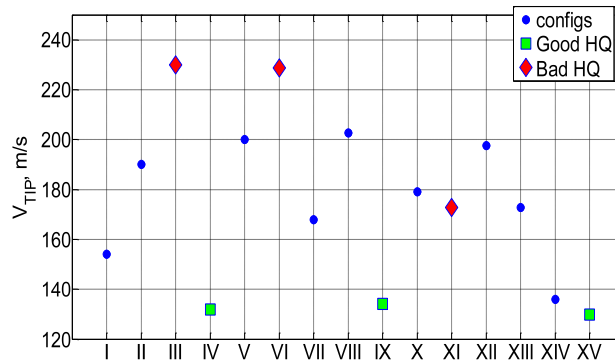


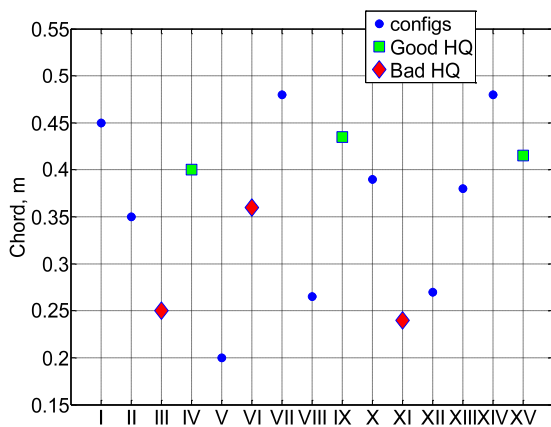
Figure 10 and Figure 11 depict design parameter distributions of all configurations with additional emphasize on these selected design configurations with different BPD results.



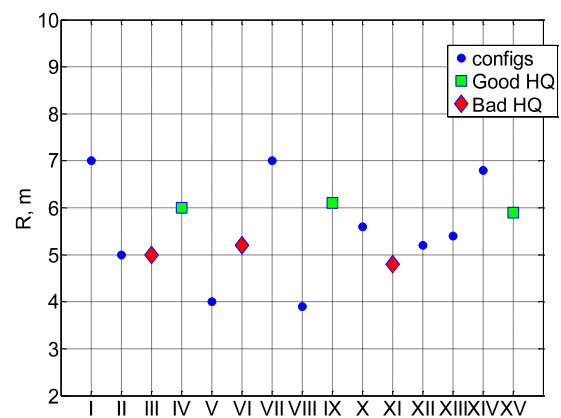


(e) Tip speed comparison

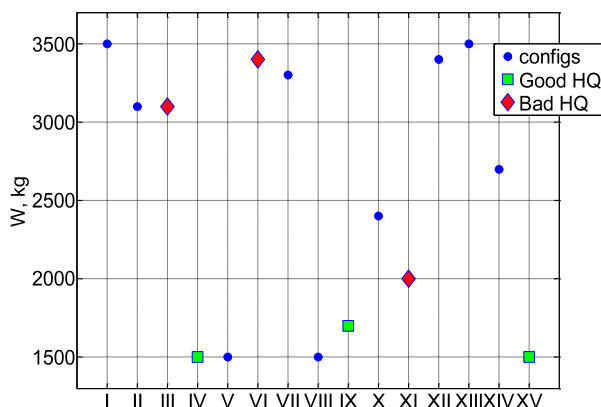
Figure 10: Preliminary design parameter comparisons among all configurations and the selected ones with good and poor HQs according to BPD analysis.



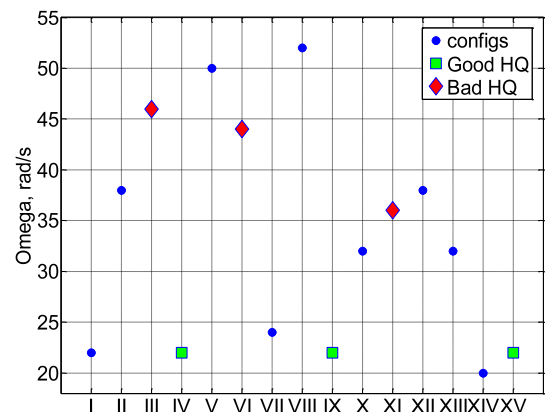
(a) Chord comparison



(b) Radius comparison



(c) Weight comparison



(d) Main rotor rotational speed comparison

Figure 11: Independent design parameter comparisons among all configurations and the selected ones with good and poor HQs according to BPD analysis.

## Results

Figure 10 and Figure 11

Aspect Ratio (AR) comparison (see Figure 10 (a)) shows that the majority of the configurations are around low boundary of design space. All configurations with good HQ are also close to the low AR boundary. However, C-VI with the poorest HQ configuration is also in the same AR region. Besides, two other poor HQ configurations have the highest AR values. These comparisons indicate that low AR values do not necessarily assure a good HQ, although all good HQ configurations belong to low AR regime.

Solidity comparison (see Figure 10 (b)) poses that there is higher scatter than AR values, such that a pattern for good or poor HQ could not be concluded. Besides, it must be considered that the selection of all design configuration points in design envelope maps was performed according to their location on solidity maps, which already inherently indicates a spread in configuration values. However, this does not change the fact that there is no conclusive trend among configurations with different HQs.

Disc loading comparison (see Figure 10 (c)) shows that configurations form up a scattered pattern of disc loading values. There is a noticeable pattern for good HQ configurations: the lowest disc loading values have the best HQs. A similar pattern is not observed for the bad HQ configurations, although for configurations with three and four number of blades, poor HQ configurations have the highest disc loading values.

Blade loading coefficient comparison (see Figure 10 (d)) shows a similar pattern as AR, such that majority of the values lie within a certain regime, which is the highest blade loading coefficient boundary of the envelope. However, some clear distinctive low values belong to good HQ configurations. On the other hand, bad HQ regimes are not with the highest peaks of values. The trend of the blade loading coefficient distribution does not provide a conclusive result, but low values show a high tendency to have better HQs.

Tip speed comparison (see Figure 10 (d)) indicates that good HQ configurations have the lowest tip speed values. Moreover, for three and four number of blades configurations, poor HQ configurations belong to highest tip speed values. Besides, for five number of blades configuration, poor HQ is not necessarily with the highest tip speed value.

Independent design parameters;

Blade chord and radius distributions (Figure 11 (a) and (b) respectively) show that configurations have scattered values. Design configurations with good and poor HQ values with respect to the BPD criterion also do not clearly belong to any regime of distributions. However, when compared to each other, good BPD HQ configurations have higher blade chord and radius values than the poor HQ configurations. However, Figure 11 (a) and (b) do not assure that high values are always with good HQ or vice versa.

Akin to other independent design parameter trends, weight and main rotor rotational speed parameters do not show a certain trend for good or poor BPD HQ points, see Figure 11 (c) and (d). However, when compared within the HQ group, good BPD HQ configurations have lower weight and rotor rotational speed values than the poor HQ configurations.

### Summary of BPD results in the design space

Before summarizing the results, it must be kept in mind that selected configurations belong to distinctive layers of solidity maps per preliminary design parameter. Due to computational expense, this study is limited to these selected configurations. However, summary of

remarks on good HQ can be listed in *Table 3*.

Table 3. Summary of BPD based HQ assessment of various design parameters.

	<b>Design Parameters</b>	<b>BPD HQ tendency</b>
<b>Preliminary</b>	Aspect Ratio	<i>Improved BPD HQ with low AR values</i>
	Solidity	<i>Not a conclusive trend</i>
	Tip Speed	<i>The lowest tip speed values have the best BPD HQs</i>
	Disc Loading	<i>The lowest disc loading values have the best BPD HQs</i>
	Blade Loading Coefficient	<i>Good HQ with low blade loading coefficient values</i>
<b>Independent</b>	Radius	<i>Good HQ with high radius values</i>
	Chord	<i>Good HQ with high chord values</i>
	Weight	<i>Good HQ with low weight values</i>
	Main rotor speed	<i>Good HQ with low main rotor speed values</i>

## Conclusions

A design envelope was first created while considering various parameter constraints and a subspace of design configuration was selected based on BO105 helicopter specifications to be used as baseline. Nonlinear simulation models were developed from the selected configurations and linearized models in state space representation were derived in order to be used in RPC analysis methods. BPD, OLOP and PRE-PAC were applied to predict PIO for the selected configurations.

HQ and Category I PIO assessment based on BPD reveals that the lowest tip speed values and the lowest disc loading values have the best BPD based HQs. Good HQs are also predicted for configurations with low aspect ratios and low blade loading coefficients.

## References

1. Yilmaz, D., Dang-Vu, B., Jones, M., "Rotorcraft Pilot Coupling Susceptibility Accompanying Handling Qualities Prospects in Preliminary Rotorcraft Design", In proceedings of 39th European Rotorcraft Forum, Moscow, Russia, Sep. 2013.
2. ARISTOTEL, "Rigid-body helicopter model implementation report", Deliverable D2.2, Oct. 2011.

3. Anon., "Handling Qualities Requirements for Military Rotorcraft," Aeronautical Design Standard 33 (ADS-33E-PRF), US Army Aviation and Missile Command, Mar. 2000.
4. ARISTOTEL, "Baseline air-vehicle model configuration data", Deliverable D2.1, Jan. 2011.

## Appendix B: Sensitivity analysis of RPC to design parameters

### (ONERA)

This appendix presents a theoretical parametric study to evaluate the effects of some preliminary rotorcraft design parameters on RPC, using the simulator-validated configurations developed in ARISTOTEL. The approach proceeds as follows. Starting from a nominal configuration of the BO105 and the IAR330 implemented on the simulators, a selection is made for the design parameters (from rotor, fuselage, flight control system) that may affect the dynamics of the closed-loop pilot-vehicle system. These dynamics are characterized by the parameters that are used in the rigid-body RPC prediction criteria or by the eigenvalues used in the aero-servo-elastic stability analysis. It is then estimated how the variation of a design parameter impacts on the position of the modified configuration over the criteria borderline or over the stability boundary.

Section 1 presents the sensitivity analysis of rigid-body Category II RPC to design parameters from a nominal configuration of the BO105, using the Open Loop Onset Point (OLOP) criterion.

Section 2 presents the sensitivity analysis of aeroelastic RPC to design parameters from a nominal configuration of the IAR330, using eigenvalues analysis.

#### 1. Rigid body RPC sensitivity analysis

A number of design points provided by TUD and applied to a BO105 baseline rigid-body simulation model are used to determine Cat II RPC susceptibility. Variations are applied on the following design parameters (see Section 2 of Appendix A): number of rotor blades, rotor radius, blade chord, rotor speed, helicopter weight.

Linearized models around trimmed flight (hover, 30kts, 60kts) were derived by TUD from the nonlinear simulation models (see Section 3 of Appendix A). For each above configuration, the actuator rate limit which drives the rotorcraft into PIO is now determined using the OLOP criterion, in both the pitch axis and the roll axis.

The OLOP was developed by DLR using describing function techniques and stability regions on the Nichols chart on a number of existing rate saturated aircraft systems [1]. The OLOP is defined as the frequency response value of the open-loop system at the closed-loop onset frequency. This frequency is the point at which actuator saturation first occurs. The closed-loop system describing function is characterised by a jump phenomenon after rate limiting onset, which can be recognized in a Nichols chart as a significant phase jump (Figure 1). OLOP can be identified as the point where the phase jump starts. If the OLOP is located at high amplitudes the additional phase delay causes an increase in the closed-loop amplitude as demonstrated in the Nichols chart. This increase in closed-loop amplitude provokes stronger rate saturation and, therefore, further increasing phase delay. This mechanism can lead to closed-loop instability. If the OLOP is located clearly below 0 dB, the onset of the rate limiter still causes additional phase delay but the change in closed-loop amplitude is less dramatic.

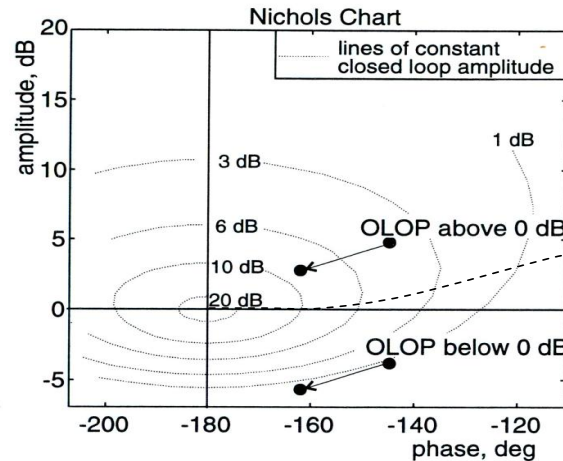


Figure 1: Physical significance of the OLOP parameter.

From off-line analysis of a number of flight experiments a stability boundary was proposed by DLR [1, 2]. As the criterion often over-predicted the susceptibility of certain configurations to PIOs, the modified boundary proposed in Ref. [3] derived from the original one by a 10dB gain shift will be used (OLOP2 boundary).

The application of OLOP is dependent on three major factors: pilot model, rate limit, and stick input amplitude. The pilot model affects the general shape and position of the curve on the Nichols chart. The rate limit and input amplitude affect the position of the OLOP along that curve. In the development of OLOP it was suggested that the pilot be modelled as a pure gain because previous research has shown that a pilot acts as a simple gain during a fully developed PIO (synchronous precognitive behaviour). This gain has to be adjusted based on the linear crossover phase angle of the open-loop pilot-plus-aircraft system. Initially, the authors of OLOP suggested a crossover angle spectrum of  $-110\text{deg}$  (low pilot gain) to  $-160\text{deg}$  (high pilot gain) to evaluate pilot gain sensitivity. They also recommended to use maximum pilot input amplitude when determining the onset frequencies. Clearly this is a worst case scenario although it is necessary to verify that this will not produce unreasonable results when compared to flight tests [4]. The results from applying OLOP to the set of configurations C-I to C-XV of the design envelope are presented below. The pilot crossover phase angle is chosen equal to  $-160\text{deg}$  and the pilot amplitude input is  $5\text{deg}$  of cyclic control actuator deflection.

### 1.1 Roll axis OLOP

The roll axis OLOP at hover flight is shown in Figure 2 for the configurations C-I to C-V. As mentioned above, the original OLOP boundary often over-predicted the susceptibility to PIOs, so a modified OLOP2 boundary proposed in Ref. [3] derived from the original one by a 10dB gain shift is used. As indicated in Table C.1, these configurations are with  $N=4$  number of blades. Configurations C-I to C-IV become PIO prone as the actuator rate limit is reduced to a value around  $6\text{deg/s}$ . Configuration C-V is borderline with a rate limit around  $5\text{deg/s}$ .

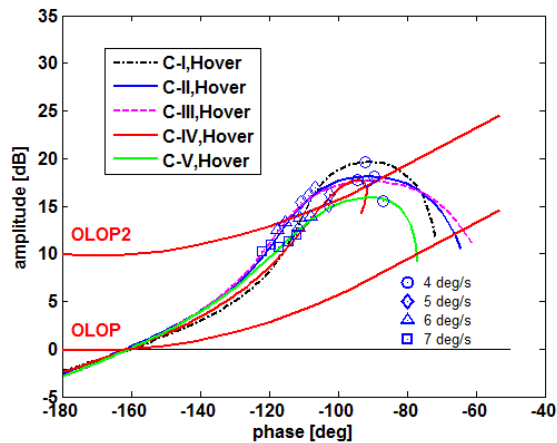


Figure 2: Roll axis OLOP at hover flight.

In Table 1, the roll axis OLOP for different velocities shows a noticeable higher rate limit for hover than for 30 knots and 60 knots forward velocities. This suggests that hover is the dimensioning flight condition for determining the minimum rate limit.

Table 1. Roll axis rate limits (deg/s)

	C-I	C-II	C-III	C-IV	C-V
Hover	5.85	5.86	5.67	5.60	4.51
30 kts	2.61	2.01	2.03	3.05	2.02
60 kts	2.58	2.09	2.03	2.15	2.03

The same trend is indeed observed for all the configurations C-I to C-XV. The configuration for which the difference in rate limits between hover and forward flight is the least is C-XV. This can be seen in Figure 3 where each configuration is characterized by a minimum rate limit and an onset frequency. For clarity purposes only the configurations C-XI to C-XV are represented (N=5 number of blades).

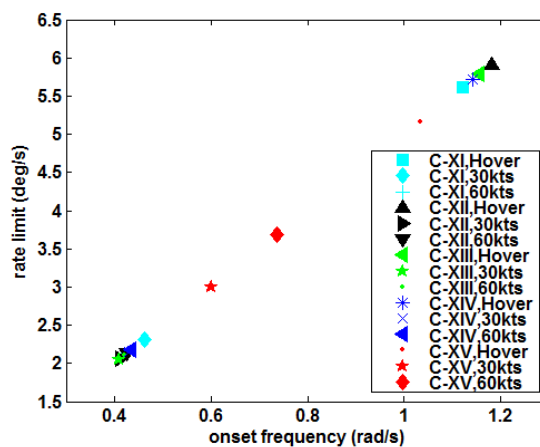


Figure 3: OLOP distribution of configurations with N=5 number of blades in roll axis.

Among all the configurations, C-IX has the highest rate limit while C-VI has the lowest (Figure 4), although the differences are relatively small. Thus, lowest minimum rate limits are obtained for configurations with high tip speed values and high disc loading values.

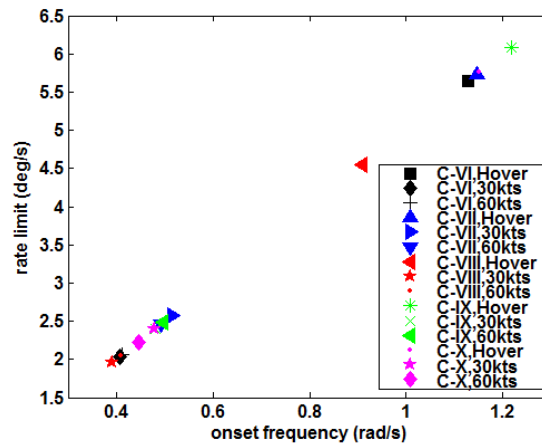


Figure 4: OLOP distribution of configurations with N=3 number of blades in roll axis.

For all the configurations it can be checked that the ratio of the rate limit to the onset frequency remains constant and equal to the actuator maximum deflection, i.e. 5deg.

### 1.2 Pitch axis OLOP

The pitch axis OLOP at 60kts forward flight is shown in Figure 5 for the configurations C-I to C-V. Configurations become PIO prone when the actuator rate limit is reduced to a value around 4.5deg/s. The configuration C-IV has the highest rate limit, but the difference between the configurations are relatively small as shown in Table 3.

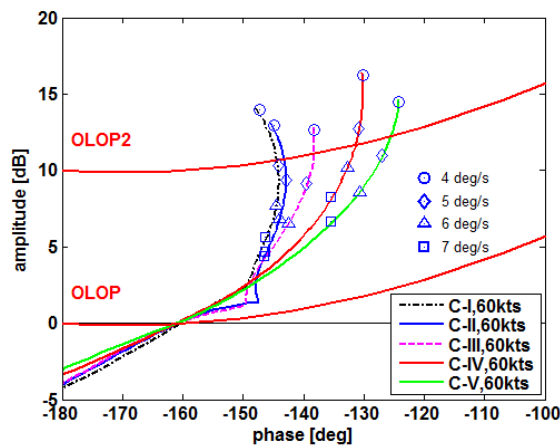


Figure 5: Pitch axis OLOP at 60kts forward flight.

The difference of rate limits between hover flight and forward flight is less important for the pitch axis than for the roll axis as shown in Table 2. The same trend is observed for all the configurations C-I to C-XV.

Table 2. Pitch axis rate limits (deg/s)

	C-I	C-II	C-III	C-IV	C-V
Hover	5.55	4.75	4.10	5.03	4.30
30 kts	4.37	4.20	4.04	4.75	4.39
60 kts	4.87	4.57	4.39	5.37	4.60

Among all the configurations, C-IX has the highest rate limit while C-VI has the lowest (Figure 6). Thus, lowest minimum rate limits are obtained for configurations with high tip speed values and high disc loading values.

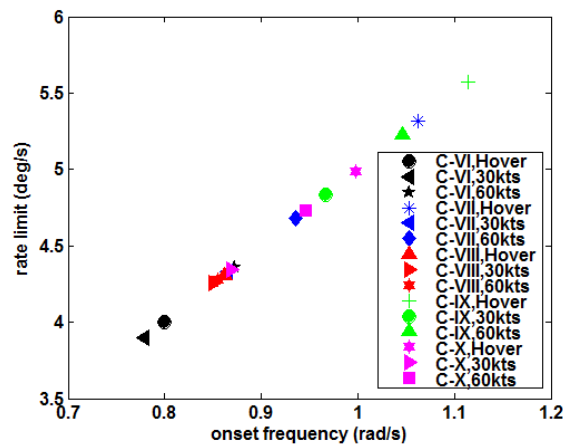


Figure 6: OLOP distribution of configurations with N=3 number of blades in pitch axis.

## 2. Aeroelastic RPC sensitivity analysis

The baseline rotorcraft configurations on which variations on the design parameters are applied is the IAR330. A number of design points are generated with the HOST code and are used to determine elastic RPC susceptibility. Variations are applied on the following design parameters (see Table 3): rotor speed, helicopter weight, blade chord, lead-lag damping coefficient, blade torsion stiffness, flap stiffness, lag stiffness. In Table 3, only the values of the stiffness distribution at the root and the tip locations of the blade are shown.

Table 3. Parameter values of design configurations

Configuration	I	II	III	IV	V	VI	VII	VIII	IX	X	XI	XII	XIII	XIV
Rotor speed (rad/s)	27.0	32.4	21.6	27.0	27.0	27.0	27.0	27.0	27.0	27.0	27.0	27.0	27.0	27.0
Weight (kg)	7345	7345	7345	4500	9150	7345	7345	7345	7345	7345	7345	7345	7345	7345
Disc Loading (kg/m <sup>2</sup> )	41.68	41.68	41.68	25.53	51.92	41.68	41.68	41.68	41.68	41.68	41.68	41.68	41.68	41.68
Chord (m)	0.60	0.60	0.60	0.60	0.60	0.50	0.70	0.60	0.60	0.60	0.60	0.60	0.60	0.60
Lead-lag damping (Nm/rad/s)	7000	7000	7000	7000	7000	7000	7000	2100	7000	7000	7000	7000	7000	7000
Torsion stiffness (10 <sup>4</sup> Nm <sup>2</sup> )	84.00 8.70	100.80 10.44	67.20 6.96	84.00 8.70	84.00 8.70	84.00 8.70	84.00 8.70							
Flap stiffness (10 <sup>4</sup> Nm <sup>2</sup> )	178.00 8.20	213.60 9.84	142.40 6.56	178.00 8.20	178.00 8.20									
Lag stiffness (10 <sup>4</sup> Nm <sup>2</sup> )	178.00 71.50	213.60 85.80	142.40 57.20											

For each above configuration, a linearized model around trimmed flight (hover, 80kts) has been derived from the HOST nonlinear simulation model. The passive couplings of the pilot biomechanics with the helicopter aeroelasticity are then analysed with an eigenvalues analysis method [5].

Figure 7 presents the coupling scheme of the pilot-vehicle system with the passive pilot closing the loop.

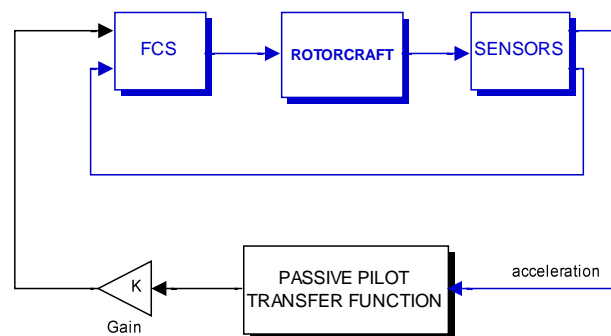


Figure 7: Coupled passive pilot-vehicle system.

The passive pilot model used in the eigenvalues analysis study is represented by transfer functions using pilot seat accelerations as input and control sticks (collective and cyclic) accelerations normal to the handle as output. The transfer functions have been identified by POLIMI from the experiments conducted in UoL's Heliflight simulator [6].

Figure 8a shows the Bode diagram of the relative collective control rotation transfer function for Pilot A. The transfer function is characterised by poles at  $-68.46 \pm 23.35j$ ,  $-6.86 \pm 38.28j$ ,

$-5.08 \pm 24.44i$ , and 2 poles at the origin. The low-frequency behaviour of the pilot transfer function is corrected by adding a washout high-pass filter.

Figure 8b shows the Bode diagram of the relative lateral cyclic control rotation transfer function for Pilot A. The transfer function is characterised by poles at  $-11.94 \pm 38.74i$ ,  $-4.44 \pm 16.18i$ ,  $-7.30 \pm 8.74i$ , and 2 poles at the origin. The low-frequency behaviour of the pilot transfer function is corrected by adding a washout high-pass filter.

Figures 9a and 9b show the corresponding transfer functions for Pilot B.

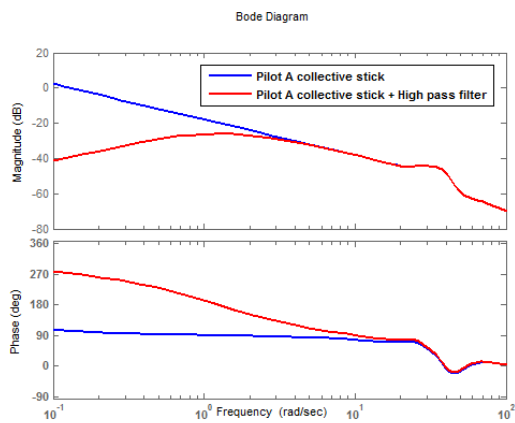


Figure 8a: Relative collective control rotation transfer function of Pilot A

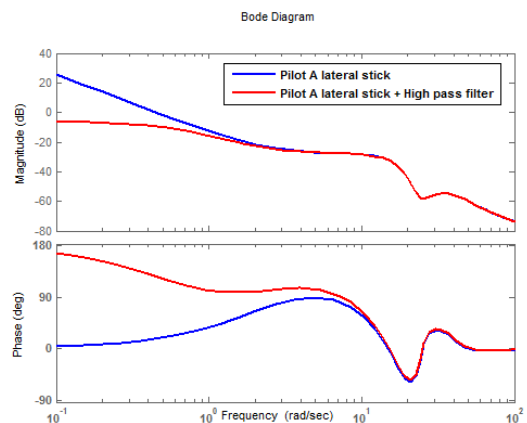


Figure 8b: Relative lateral cyclic control rotation transfer function of Pilot A

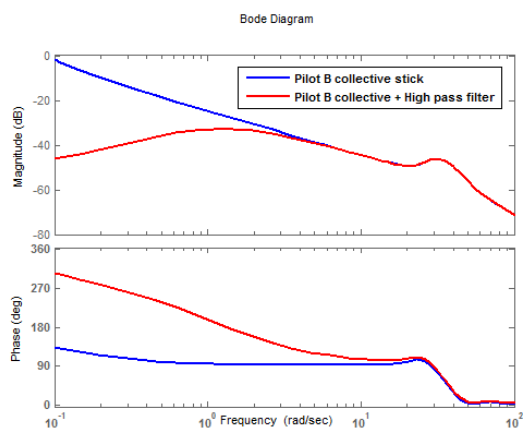


Figure 9a: Relative collective control rotation transfer function of Pilot B

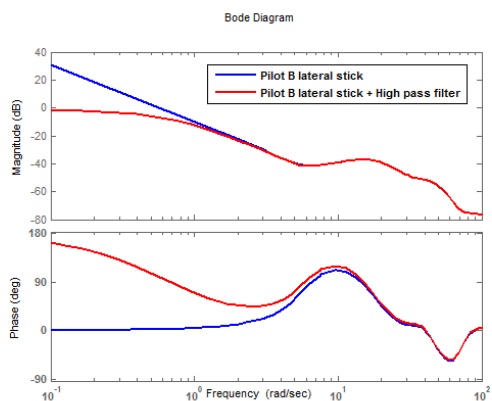


Figure 9b: Relative lateral cyclic control rotation transfer function of Pilot B

### 2.1. Stability analysis with collective control feedback

Figure 10 shows the dynamic characteristics of the nominal IAR330 helicopter (i.e. Configuration C-1) in hover flight, with the pilot A closing the loop through the collective control.

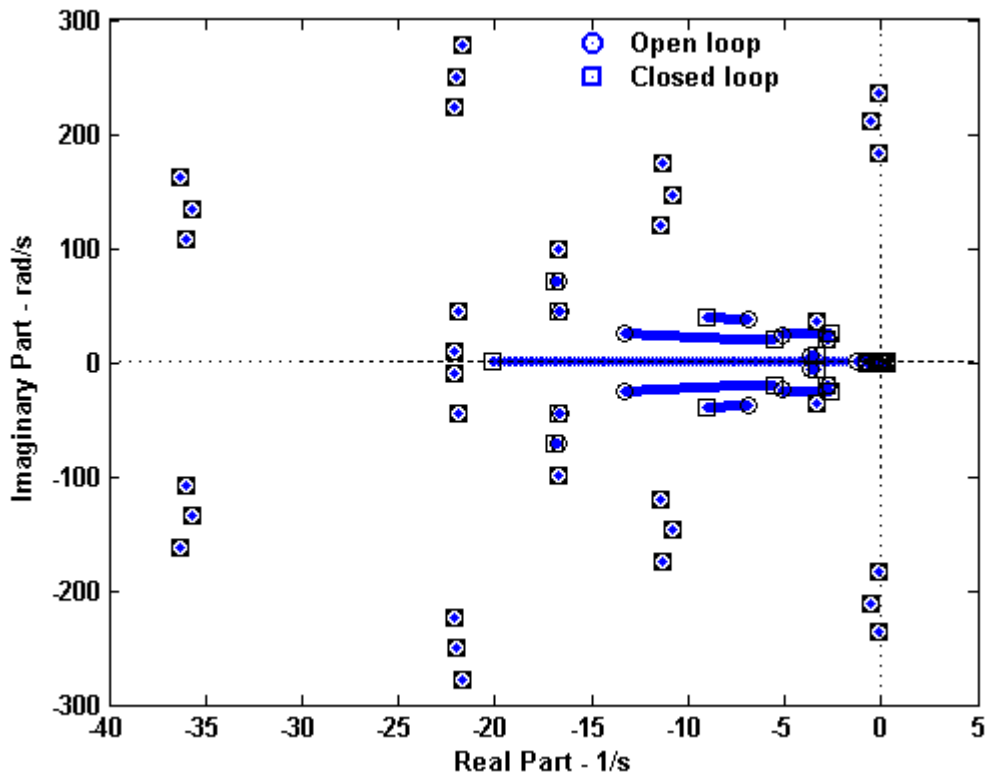


Figure 10: Root locus of Conf. C-I with collective control feedback in hover flight

For the open loop configuration, the rotor modes and progressive and regressive modes can be identified on the figure as follows:

4 <sup>th</sup> flap:	$-21.97 \pm 250.3i$	$-21.75 \pm 277.3i$	$-22.08 \pm 223.3i$
1 <sup>st</sup> torsion:	$-0.56 \pm 211.2i$	$-0.10 \pm 236.8i$	$-0.11 \pm 182.8i$
3 <sup>rd</sup> flap:	$-10.85 \pm 146.8i$	$-11.34 \pm 174.1i$	$-11.41 \pm 120.0i$
2 <sup>nd</sup> lag:	$-35.69 \pm 134.8i$	$-36.34 \pm 162.7i$	$-36.02 \pm 108.2i$
2 <sup>nd</sup> flap:	$-16.77 \pm 71.17i$	$-16.69 \pm 98.32i$	$-16.67 \pm 44.26i$
1 <sup>st</sup> flap:	$-13.39 \pm 25.31i$	$-21.95 \pm 45.04i$	$-22.15 \pm 9.60i$
1 <sup>st</sup> lag:	$-3.66 \pm 5.81i$	$-3.37 \pm 35.70i$	$-2.77 \pm 20.02i$

The most noticeable migration of the poles towards the stability boundary (imaginary axis) as the pilot closes the loop is observed for the pilot's poles which move from  $-5.08 \pm 24.44i$  to  $-2.60 \pm 25.99i$ , and for the 1<sup>st</sup> flap mode which moves from  $-13.34 \pm 25.31i$  to  $-5.56 \pm 20.60i$ .

Figure 11 shows the dynamic characteristics of the nominal IAR330 helicopter (i.e. Configuration C-I) at 80kts forward flight, with the pilot A closing the loop through the collective control.

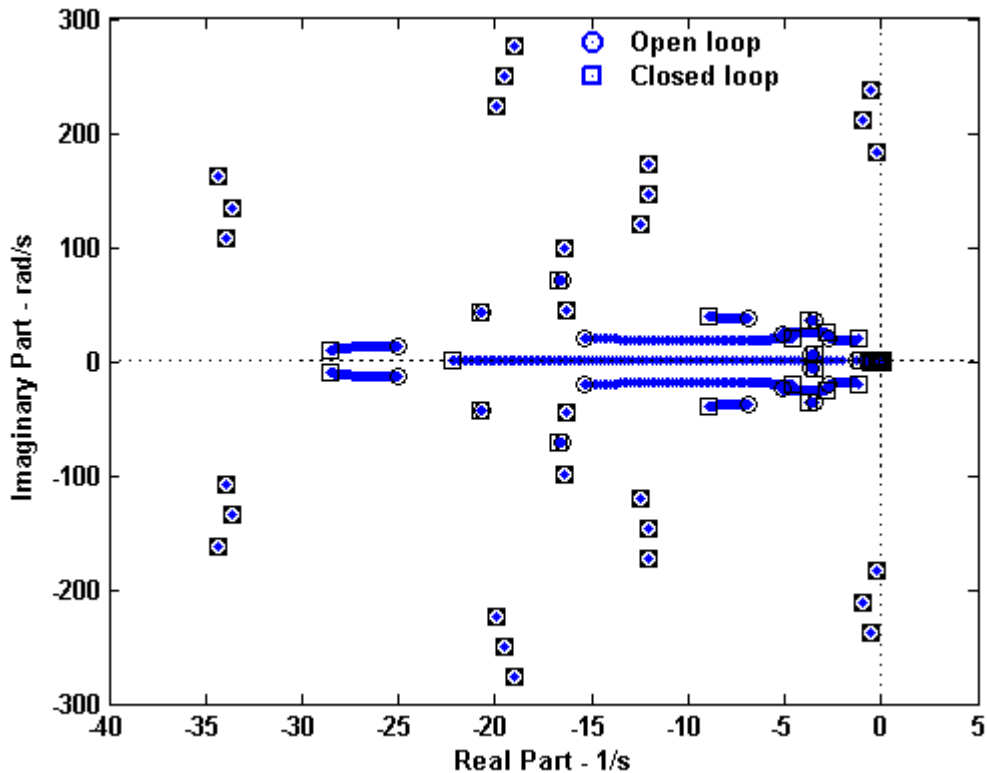


Figure 11: Root locus of Conf. C-I with collective control feedback in 80kts forward flight.

For the open loop configuration, the rotor modes and progressive and regressive modes can be identified on the figure as follows:

4 <sup>th</sup> flap:	$-19.54 \pm 250.0i$	$-19.05 \pm 277.0i$	$-19.91 \pm 223.1i$
1 <sup>st</sup> torsion:	$-0.98 \pm 211.3i$	$-0.54 \pm 236.9i$	$-0.28 \pm 183.2i$
3 <sup>rd</sup> flap:	$-12.04 \pm 146.4i$	$-12.11 \pm 173.2i$	$-12.49 \pm 119.9i$
2 <sup>nd</sup> lag:	$-33.66 \pm 135.0i$	$-34.31 \pm 162.9i$	$-33.91 \pm 108.4i$
2 <sup>nd</sup> flap:	$-16.56 \pm 71.59i$	$-16.37 \pm 98.40i$	$-16.34 \pm 44.82i$
1 <sup>st</sup> flap:	$-15.39 \pm 20.17i$	$-20.66 \pm 42.74$	$-25.01 \pm 13.56i$
1 <sup>st</sup> lag:	$-3.63 \pm 5.90i$	$-3.42 \pm 35.68i$	$-2.71 \pm 20.20i$

The most noticeable migration of the poles towards the stability boundary (imaginary axis) as the pilot closes the loop is observed for the pilot's poles which move from  $-5.08 \pm 24.44i$  to  $-2.87 \pm 25.25i$ , for the 1<sup>st</sup> flap mode which moves from  $-15.39 \pm 20.17i$  to  $-4.60 \pm 20.78i$ , and for the regressive lag mode which moves from  $-2.71 \pm 20.20i$  to  $-1.15 \pm 19.35i$ . The main differences with the hover flight are a less damped flap mode and a migration of the regressive lag mode towards the imaginary axis.

A summary of the effects of the design parameters on the pilot-vehicle modes is shown in Table 4. "Bad" means a destabilizing effect, "good" means a stabilizing effect, "no" means negligible effect.

Table 4. Summary of effects of design parameters on PVS modes

Configuration	I	II	III	IV	V	VI	VII	VIII	IX	X	XI	XII	XIII	XIV
Parameter characteristic	-	Higher rotor speed	Lower rotor speed	Lower weight	Higher weight	Lower blade chord	Higher blade chord	Lower lead-lag damping	Higher torsion stiffness	Lower torsion stiffness	Higher flap stiffness	Lower flap stiffness	Higher lag stiffness	Lower lag stiffness
Effect of parameter on closed loop pilot mode	-	bad	good	bad	good	no	no	no	no	no	no	no	no	no
Effect of parameter on open loop flap mode	-	good	bad	bad	no	bad	good	no	no	no	no	no	no	no
Effect of parameter on closed loop flap mode	-	no	no	bad	good	no	no	no	no	no	no	no	no	no
Effect of parameter on open loop regressive lag mode	-	no	no	no	no	no	no	bad	no	no	no	no	no	no
Effect of parameter on closed loop regressive lag mode	-	no	no	no	no	no	no	bad	no	no	no	no	no	no

The trends are similar for Pilot A and Pilot B. The destabilizing effects in hover flight are more or less worsened as the helicopter speed is increased.

For example, Figure 12 compares the root loci of Conf. C-I and Conf. C-II with collective control feedback in hover flight, while Figure 13 compares the root loci of the same configurations in 80 knots forward flight.

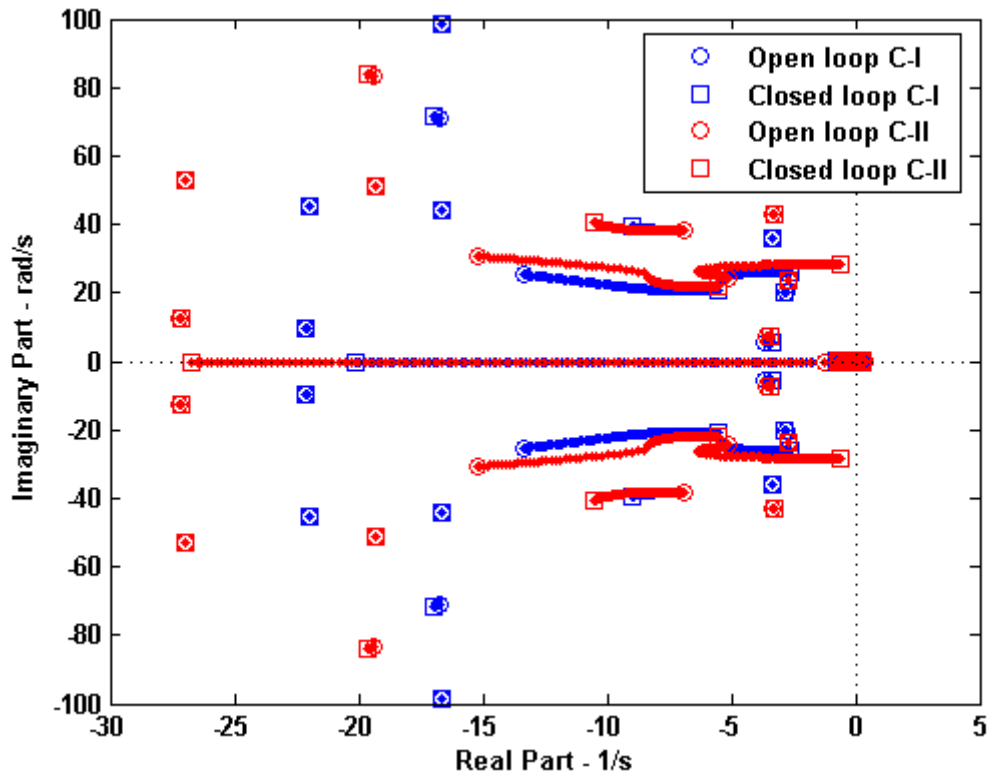


Figure 12: Root loci of Conf. C-I and Conf. C-II with collective control feedback in hover flight.

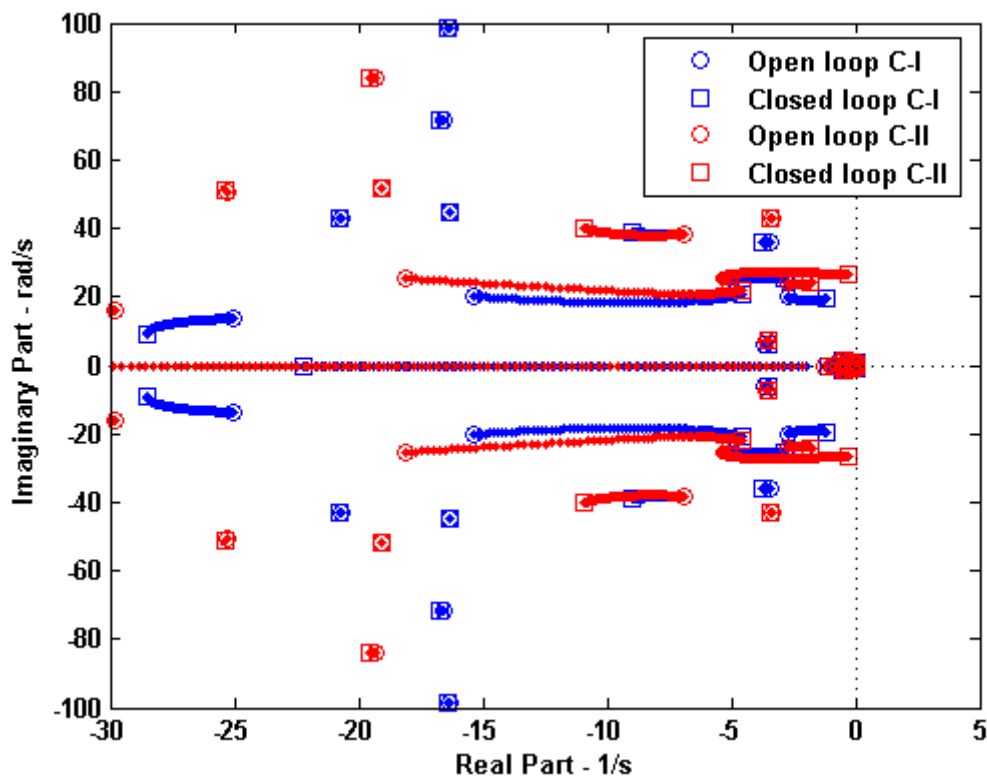


Figure 13: Root loci of Conf. C-I and Conf. C-II with collective control feedback in 80kts flight.

In Figure 12 (hover), it can be seen that the flap mode of Conf. C-I in open loop is less damped than Conf. C-II but the closed loop damping is roughly the same. For both configurations, the regressive lag mode is practically the same and remains unchanged when the pilot closes the loop. The destabilizing effect of the rotor speed on the closed loop pilot mode is more noticeable; for Conf. C-I the pilot's pole moves to  $-2.60 \pm 25.99i$ , while for Conf. C-II it moves to  $-0.28 \pm 28.13i$ .

In Figure 13 (80kts), it can be observed a little impact of the rotor speed on the regressive lag mode. Like the hover case, the closed loop pilot mode is much more affected. There is practically no effect of the helicopter forward speed on the closed loop pilot mode; for Conf. C-II, the pilot's pole migrates to  $-0.28 \pm 28.13i$  in hover flight and to  $-0.27 \pm 26.55i$  in 80kts forward flight.

As another example, Figure 14 compares the root loci of Conf. C-I and Conf. C-IV with collective control feedback in hover flight, while Figure 15 compares the root loci of the same configurations in 80 knots forward flight.

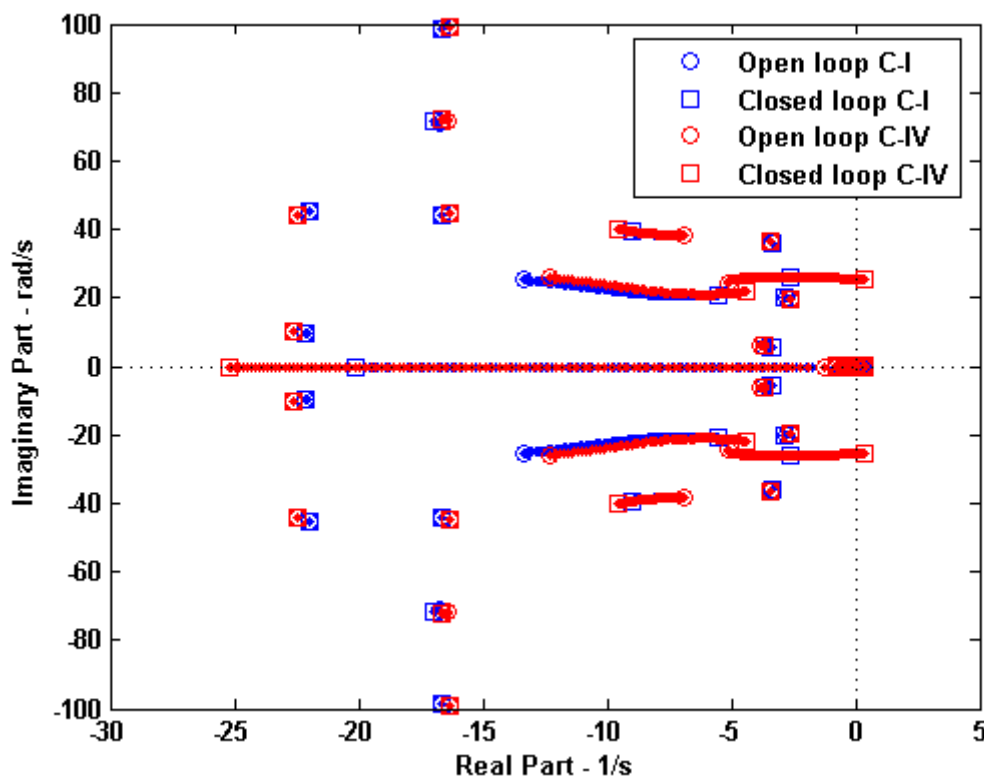


Figure 14: Root loci of Conf. C-I and Conf. C-IV with collective control feedback in hover flight.

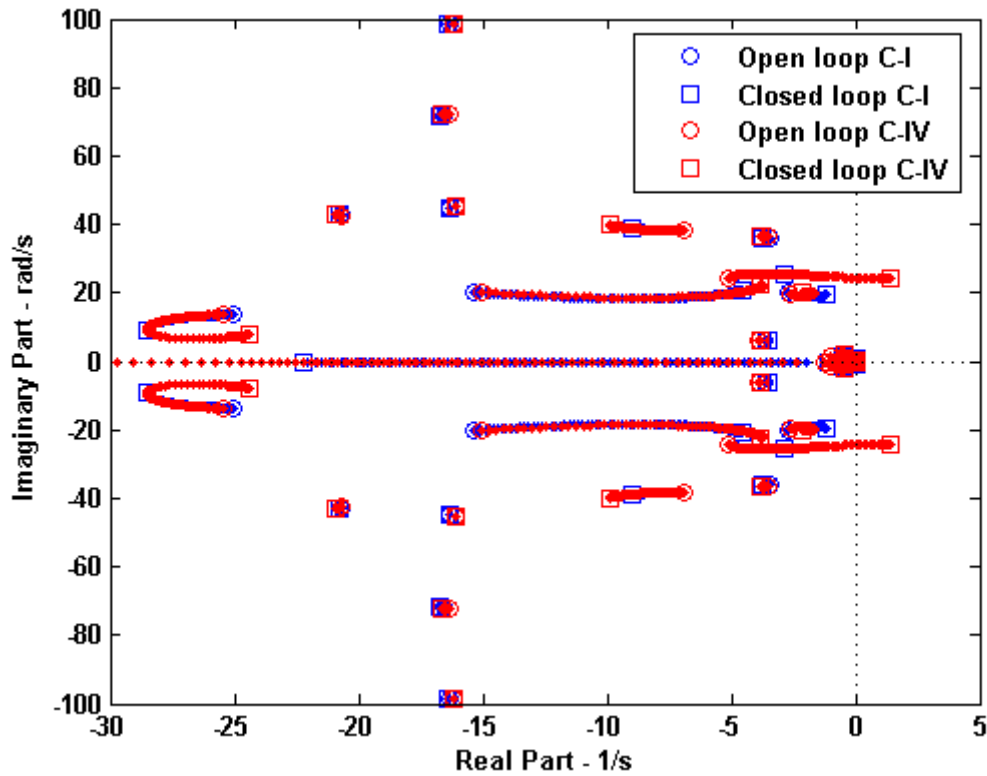


Figure 15: Root loci of Conf. C-I and Conf. C-IV with collective control feedback in 80kts forward flight.

The destabilizing effect of the helicopter weight on the closed loop pilot's mode is clearly shown in Figure 14 (hover) and Figure 15 (80kts) (poles at  $0.36 \pm 25.57i$  and  $1.44 \pm 24.39i$  respectively).

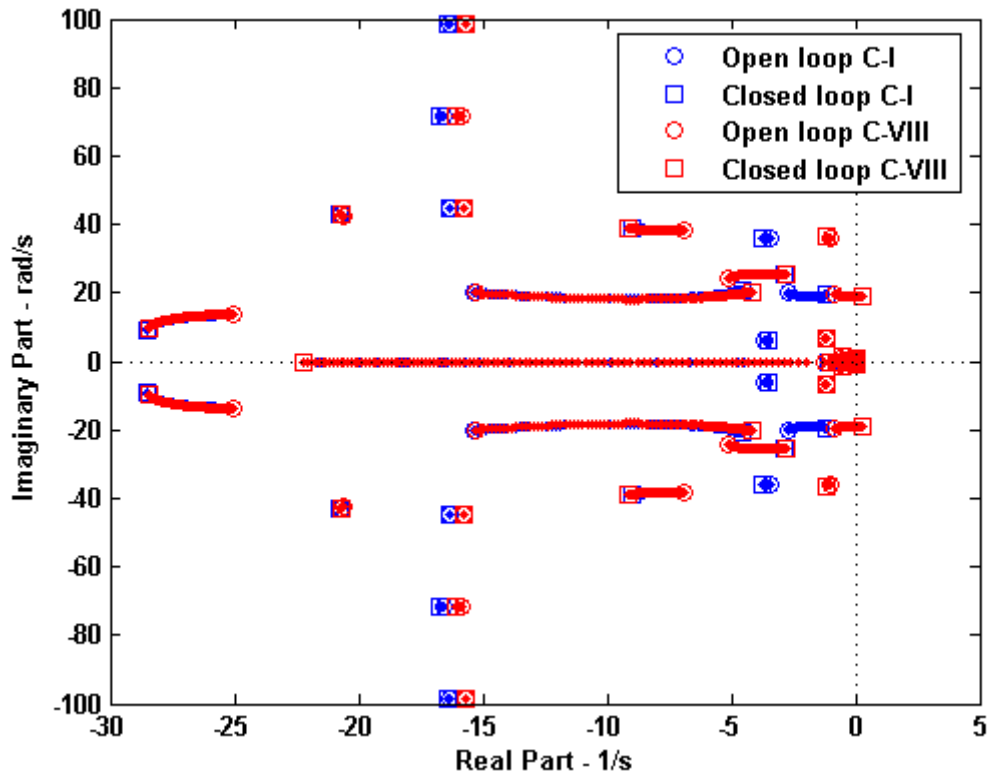


Figure 16: Root loci of Conf. C-I and Conf. C-VIII with collective control feedback in 80kts forward flight.

Figure 16 displays the effects of lead-lag damping. As expected, a lower lead-lag damping results in less damped regressive and progressive lag modes, in open loop configuration as well as in closed loop configuration. The regressive lag mode becomes even unstable moving to  $0.28 \pm 19.17i$  as the pilot closes the loop.

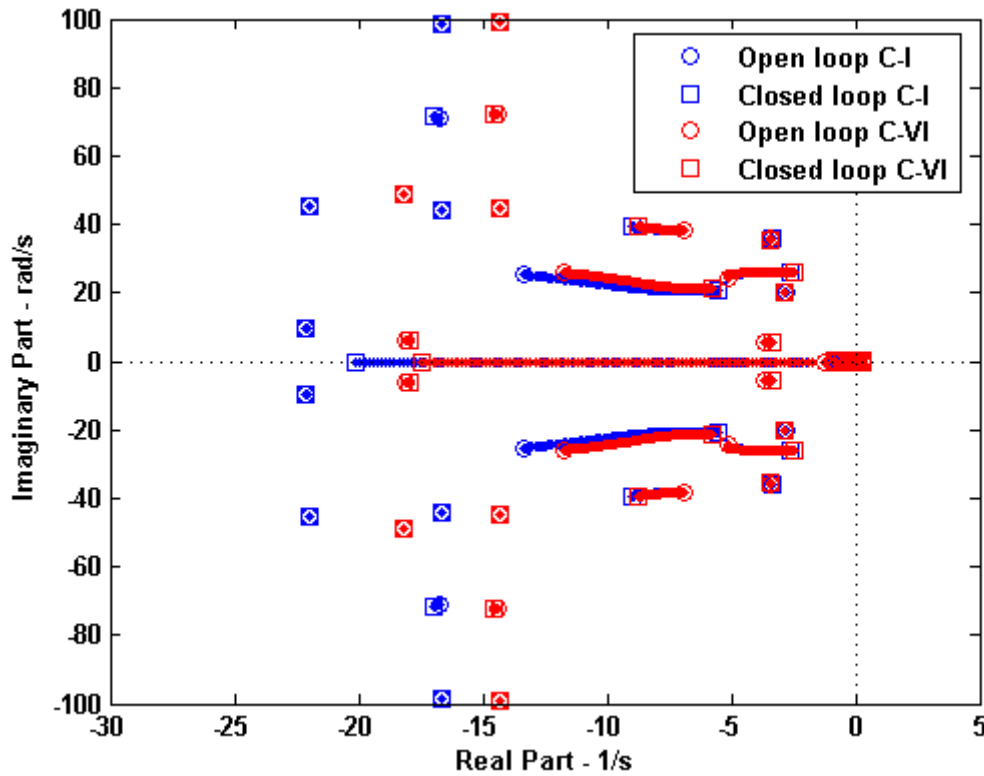


Figure 17: Root loci of Conf. C-I and Conf. C-VI with collective control feedback in hover flight.

Figure 17 displays the effects of blade chord. A lower blade chord results in lower Lock number and therefore lower flap damping. However the effect on the closed loop flap mode is negligible.

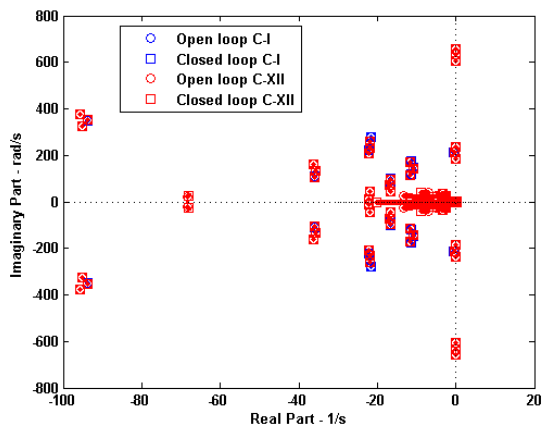


Figure 18: Root loci of Conf. C-I and Conf. C-XII with collective control feedback in hover.

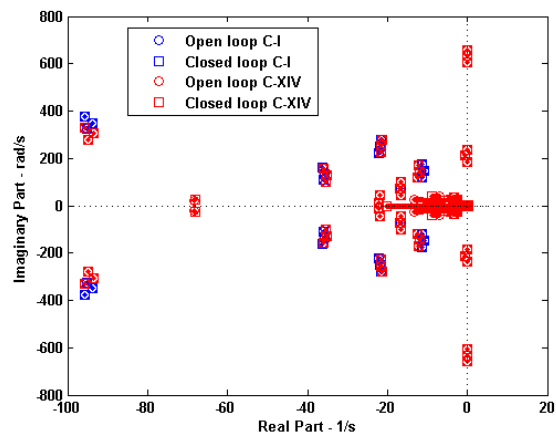


Figure 19: Root loci of Conf. C-I and Conf. C-XIV with collective control feedback in hover.

Figure 18 and Figure 19 show that there is practically no impact of the blade stiffness on the pilot's modes and the 1<sup>st</sup> flap mode.

Figure 20 displays the closed loop eigenvalues for all the configurations. It can be seen that the less stable configurations are Conf. C-IV, C-VIII and C-II.

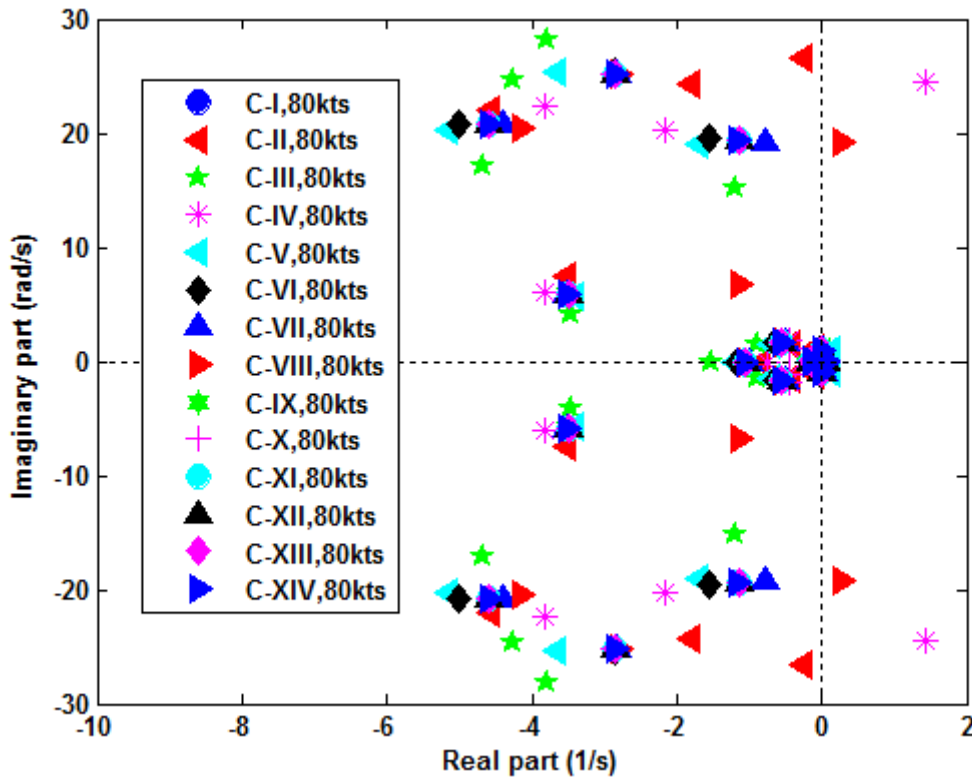


Figure 20: Closed loop eigenvalues of all configurations.

## 2.2. Stability analysis with lateral cyclic control feedback

Figure 21 and Figure 22 show the dynamic characteristics of the nominal IAR330 helicopter (i.e. Configuration C-I) in hover flight and 80kts forward flight, with the pilot A closing the loop through the lateral cyclic control.

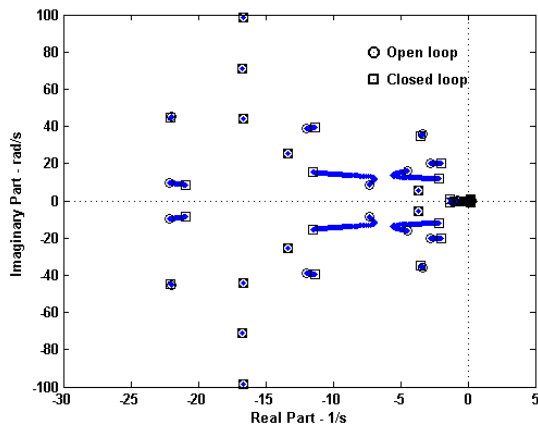


Figure 21: Root locus of Conf. C-I with lateral cyclic control feedback in hover flight

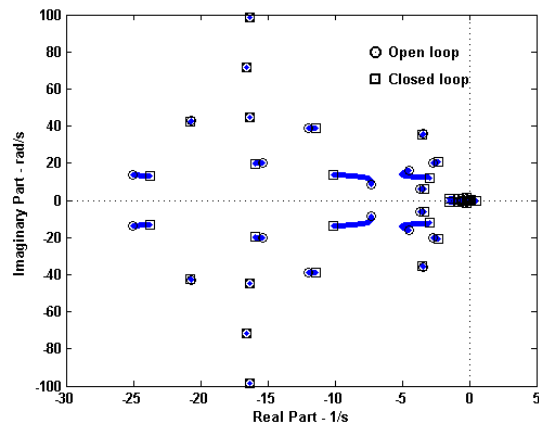


Figure 22: Root locus of Conf. C-I with lateral cyclic control feedback in 80kts forward flight

The pilot has a destabilizing effect on the pilot-vehicle system stability, mainly through the pilot's mode  $-4.44 \pm 16.18i$  which moves closer to the imaginary axis and the spiral mode which becomes unstable.

The effects of the design parameters on the above modes are very small. The most noticeable effects are concerned with Conf. C-III. Figures 23a, b and c compare the root loci of Conf. C-I and Conf. C-III with lateral cyclic control feedback in 80kts forward flight.

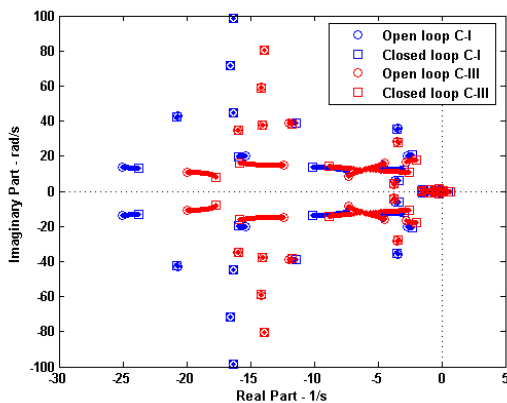


Figure 23a: Root loci of Conf. C-I and Conf. C-III with lateral cyclic control feedback in 80kts forward flight.

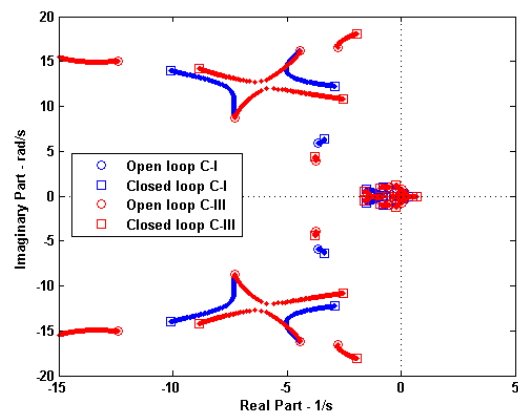


Figure 23b: Root loci of Conf. C-I and Conf. C-III with lateral cyclic control feedback in 80kts forward flight.

A zoom of Figure 22a around the pilot's modes (Figure 22b) shows that the destabilizing effects concern the pilot's pole  $-7.30 \pm 8.74i$  which moves closer to the imaginary axis, instead of the pole  $-4.44 \pm 16.18i$  which moves away from the imaginary axis. A zoom of Figure 23a around the flight mechanics modes (Figure 23c) shows that the closed loop spiral mode of Conf. C-III (+0.71) is more unstable than Conf. C-I (+0.49). The open loop Dutch roll of Conf. C-III is unstable.

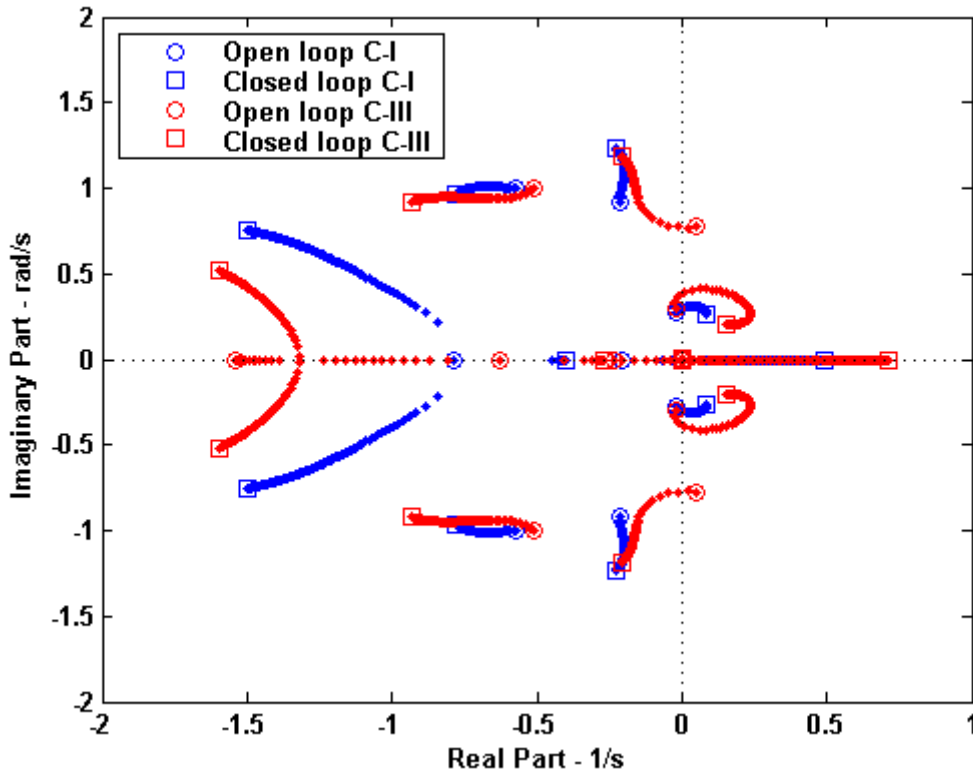


Figure 23c: Flight mechanics root loci of Conf. C-I and Conf. C-III with lateral cyclic control feedback in 80kts forward flight.

Figure 24 compares the root loci of Conf. C-I and Conf. C-VIII with lateral cyclic control feedback in 80kts forward flight, while Figure 25 compares the root loci of the same configurations in hover flight.

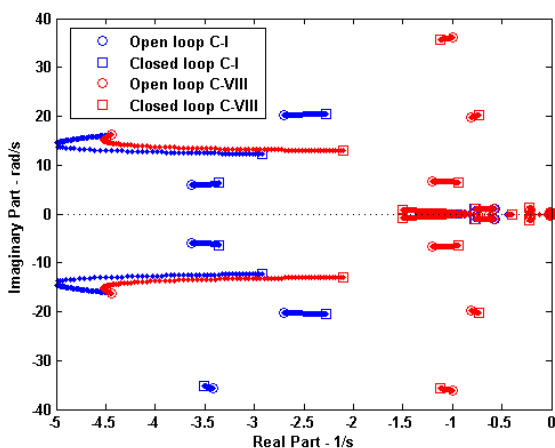


Figure 24: Root loci of Conf. C-I and Conf. C-VIII with lateral cyclic control feedback in 80kts forward flight.

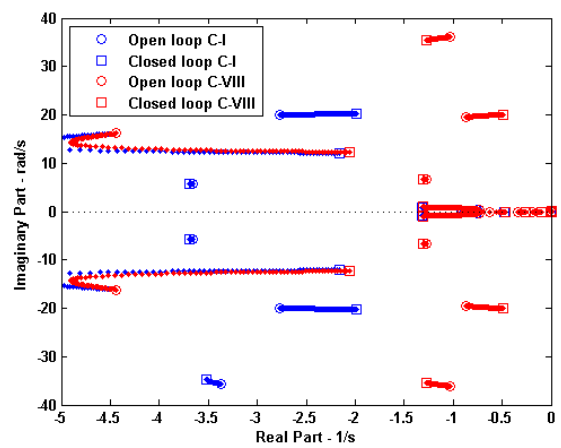


Figure 25: Root loci of Conf. C-I and Conf. C-VIII with lateral cyclic control feedback in hover flight.

Lower lead-lag damping results in less damped regressive lag mode (open loop as well as closed loop) and the destabilizing effect increases as the forward speed is decreased. In

Figure 24 (80kts), the regressive lag mode of Conf. C-VIII moves from  $-0.81 \pm 19.74i$  to  $-0.74 \pm 20.18i$ , while in Figure 25 (hover), it moves from  $-0.87 \pm 19.53i$  to  $-0.49 \pm 20.08i$ .

### 3. Conclusion

In summary of sensitivity analysis of rigid body Category II RPC in the design space, Category II RPC assessment based on OLOP shows that in the roll axis, hover is the dimensioning flight condition for determining the minimum rate limit. In the pitch axis, the difference of rate limits between hover and forward flight is less important. Lowest minimum rate limits are obtained for configurations with high tip speed values and high disc loading values. After the conclusion of Appendix A, these configurations produce the worst Bandwidth Phase Delay (BPD) handling qualities due to low bandwidth. Low bandwidth configurations yield low crossover frequencies (for the same pilot gain), and low OLOP onset frequencies. As the minimum rate limit is proportional to the onset frequency, the conclusion on the configurations via the OLOP analysis is coherent with the BPD analysis. In the design process a compromise has to be found between good BPD handling qualities and low rate limits.

In summary of sensitivity analysis of aeroelastic RPC in the design space, the dynamic characteristics of the coupled pilot-IAR330 helicopter as the pilot closes the loop through the collective control are characterized mainly by a migration of the pilot's poles and the 1<sup>st</sup> flap mode towards the stability boundary. This decrease in stability is worsened and instability may even occur with high forward speed, low helicopter weight, high rotor speed, and low lead-lag damping. There is little sensitivity of the stability decrease to the blade chord and practically no sensitivity to the blade stiffness. The dynamic characteristics of the coupled pilot-IAR330 helicopter as the pilot closes the loop through the lateral cyclic control are characterized mainly by a migration of the pilot's poles towards the stability boundary and the destabilization of the spiral mode. The rotor elastic modes are little affected. The decrease in stability is worsened with low forward speed, low rotor speed, and low lead-lag damping. There is little sensitivity of the stability decrease to the helicopter weight and the blade chord and practically no sensitivity to the blade stiffness.

### References

1. Duda, H., "Effects of Rate Limiting Elements in Flight Control Systems – A New PIO Criterion", AIAA-Paper-95-3304, Aug. 1995.
2. Duda, H., Hovmark, G. and Forssell, L., "Prediction of Category II Aircraft-Pilot Couplings – New Experimental Results", AIAA-Paper-97-3499, Aug. 1997.
3. Wilmes, T., Duda, H., "Investigation of Electronic Filters to Prevent Aircraft-Pilot-Coupling", Technical Report IB 111-98/29, Institut für Flugmechanik, Braunschweig, Nov. 1998.
4. Gilbreath, G.P., "Prediction of Pilot-Induced Oscillations Due to Actuator Rate Limiting Using the Open-Loop Onset Point Criterion", AFIT/GAE/ENY/01M-02, Air Force Institute of Technology, 2002
5. ARISTOTEL, Prediction of aero-servo-elastic instabilities with and without pilot in the loop, Deliverable D3.9, March 2013.
6. ARISTOTEL, Complete Bio-Dynamical Test Data Analysis and Critical Review, Deliverable D4.4, January 2013.

## **Appendix C: Robust Stability Analysis of RPC sensitivity to pilot biodynamic feedthrough and design parameters (POLIMI)**

This section presents the application of the robust stability approach developed by POLIMI [46,47] as a simple and effective method to assess the sensitivity of pilot-vehicle interaction to pilot biodynamic feedthrough (BDFT) and vehicle design parameters. The work illustrated in the following has been developed in cooperation with TUD, and presented in [42,43]. Other applications of the method to pilot-vehicle interaction have been developed within the project [22], also in cooperation with UROMA3 [44,45].

### **1. Introduction**

This work addresses the problem of RPCs from the point of view of robust stability analysis by treating the pilot's BDFT as an uncertainty in the dynamics of a closed-loop system. This makes the definition of robust stability margins possible in an easy and straightforward manner provided that

- 1) the aeromechanics of the rotorcraft are known (e.g. in the form of a transfer function), and
- 2) the range of BDFT variability is known as a function of frequency.

The latter can be expressed as the maximum and minimum feedthrough possible for a particular pilot task, as a function of the frequency. A tool for assessing the impact of BDFT on RPCs is obtained by evaluating its effects on the robust stability boundaries of the rotorcraft. As long as the effect of the BDFT dynamics remains within the stability boundary for every frequency, no instability can occur; if the boundary is exceeded, the rotorcraft must be considered RPC prone and the pilot's BDFT response may drive the coupled system unstable. Thus, the proposed tool may aid in the design of rotorcraft providing insight in how vehicle and FCS dynamics couple with the pilot's BDFT.

To illustrate the procedure a realistic aeroservoelastic model of a complete helicopter, originally presented and validated in Ref. [18], is used. The range of possible BDFT was determined using a database of experimental results where BDFT was measured for pilots performing various tasks using a generic rotorcraft control layout [19]. The tasks were designed to demand different control behaviour of the pilots, resulting in different BDFT dynamics for each task.

The combination of the experimental BDFT data with the robust stability margins unveils whether, and which, piloting behaviour may lead to RPC proneness for any rotorcraft model and regardless of its complexity in terms of number and type of states. Conversely, given the BDFT, one can investigate which model parameters impact the stability and in which frequency range RPCs are likely to occur. This may help design rotorcraft that are less susceptible to RPCs.

The work is organized as follows. Section 2 briefly discusses robust stability analysis based on the Generalized Nyquist Criterion (GNC). Section 3 presents Biodynamic Feedthrough, and describes how vehicle accelerations lead to involuntary control inputs. It discusses how

BDFT is measured for different limb dynamics. Section 4 shows how stability margin curves can be extracted from a ‘certain’ (in a robust stability sense) aeroelastic model of a rotorcraft and compared to experimental BDFT curves to evaluate the likelihood of RPCs to occur for that rotorcraft.

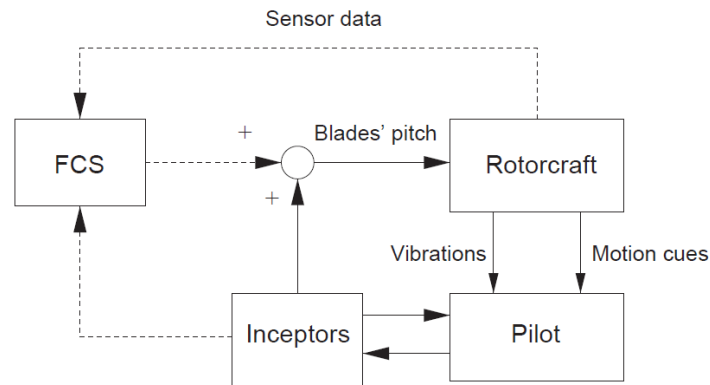


Fig. 1. Generic RPC block scheme. The rotorcraft transmits vibrations in addition to visual and sensorial cues to the pilot. The pilot acts on the inceptors, but is also ‘disturbed’ by the forces exerted by the inceptors. The presence of the FCS loop depends on the architecture of the aircraft.

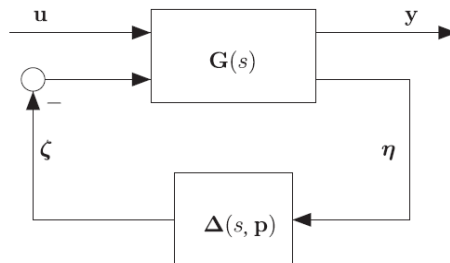


Fig. 2. Feedback loop between nominal plant and uncertainty operator.

## 2. Robust Stability Analysis

Consider a Linear Time Invariant (LTI) system characterized by a set of uncertain parameters  $\mathbf{P}$ . By using the Linear Fractional Transform (LFT, Ref. [20]), all the uncertainties can be collected into a norm bounded operator  $\Delta(\mathbf{p}, s)$  connected in feedback with the ‘certain’ model of the system characterized by the transfer function  $\mathbf{G}(s)$ , as shown in Figure 2. The plant  $\mathbf{G}(s)$  can be partitioned as

$$\begin{Bmatrix} \mathbf{y} \\ \eta \end{Bmatrix} = \begin{bmatrix} \mathbf{G}_{11} & \mathbf{G}_{12} \\ \mathbf{G}_{21} & \mathbf{G}_{22} \end{bmatrix} \begin{Bmatrix} \mathbf{u} \\ \zeta \end{Bmatrix} \quad (1)$$

with a negative feedback loop that can be established on the transfer matrix  $\Delta$  of the uncertain part,  $\zeta = -\Delta\eta$ . The transfer function between  $\mathbf{u}$  and  $\mathbf{y}$  is

$$\mathbf{y}(s) = \left( \mathbf{G}_{11} - \mathbf{G}_{12}\mathbf{\Delta}(\mathbf{I} + \mathbf{G}_{22}\mathbf{\Delta})^{-1} \mathbf{G}_{21} \right) \mathbf{u} = \overline{\mathbf{G}}\mathbf{u}(s) \quad (2)$$

Under the assumption that the baseline system,  $\overline{\mathbf{G}}$  with  $\mathbf{\Delta} \equiv \mathbf{\Delta}_0$ , is stable, and that  $\mathbf{\Delta}$  itself is stable for all acceptable values of the parameters  $\mathbf{P}$ , the stability of the uncertain system of Eq. (C.2) can be studied by considering that of the transfer function

$$\mathbf{H}(j\omega) = \mathbf{G}_{22}(j\omega)\mathbf{\Delta}(j\omega) \quad (3)$$

which plays the role of the loop transfer function in classical feedback control theory [21]. The stability of the transfer function of Eq. (3), in turn, can be studied using the Generalized Nyquist Criterion by considering the distance of the eigenvalues of the loop transfer function  $\mathbf{H}(j\omega)$  from the point  $(-1 + j0)$  as a function of the uncertain parameters. Conversely, the limit values of the parameters are found by requiring such distance to vanish, namely  $\det(\mathbf{I} + \mathbf{H}(j\omega)) = 0$  (for more details see the Refs. [22,21]).

The perturbation of the  $i$ -th eigenvalue  $\lambda_i(\mathbf{H}_0(j\omega))$  of the reference system  $\mathbf{H}_0 = \mathbf{G}_{22}\mathbf{\Delta}_0$  can be expressed as

$$\chi_i(\omega) = \lambda_i(\mathbf{H}_0(j\omega)) + \rho(\omega)e^{j\theta(\omega)}, \quad (4)$$

where the complex number  $\rho e^{j\theta}$  represents an arbitrary perturbation of the  $i$ -th eigenvalue of modulus  $\rho$  and argument  $\theta$ , as shown in Figure 3.

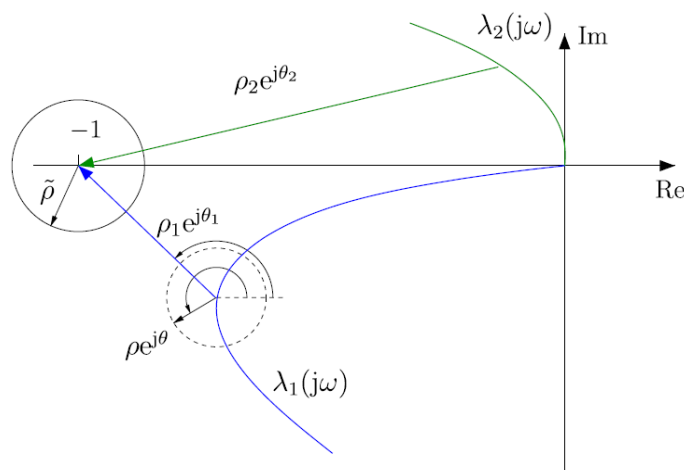


Fig. 3. Nyquist eigenloci: distance of transfer matrix eigenvalues from point  $(-1 + j0)$  in the complex plane.

When  $\lambda_i = -1$  the stability limit is reached for the eigenvalue  $\lambda_i$ , since the loop transfer function corresponding to that eigenvalue for any further perturbation would circle about point  $(-1 + j0)$ . As a consequence, the stability margin, as a function of the frequency  $\omega$ , is

$$\rho_i(\omega)e^{j\theta_i(\omega)} = -(\lambda_i(\mathbf{H}_0(j\omega)) + 1). \quad (5)$$

For each frequency  $\omega$ , the critical direction  $\theta_i(\omega)$  represents the direction from  $\lambda_i(\mathbf{H}_0(j\omega))$  to  $(-1 + j0)$ , while  $\rho_i(\omega)$  represents the magnitude of the eigenvalue perturbation that leads to instability when it occurs along the critical direction (Fig. 3).

The stability of the system is ensured whenever for

$$\theta \equiv \theta_i(\omega) = \arg(-1 - \lambda_i(\mathbf{H}_0(j\omega))) = \tan^{-1} \left( \frac{\text{Im}(\lambda_i(\mathbf{H}_0(j\omega)))}{\text{Re}(\lambda_i(\mathbf{H}_0(j\omega))) + 1} \right) \quad (6)$$

the condition

$$\rho(\omega) < \rho_i(\omega) = \|\lambda_i(\mathbf{H}_0(j\omega)) + 1\| \quad (7)$$

is met for all frequencies  $\omega$ .

These margins can be translated into bounds of the physical quantities that are included in the unstructured uncertainty operator  $\Delta^{(s)}$ . For scalar Single-Input Single-Output (SISO) systems the process is straightforward. In this case the eigenvalue  $\lambda$  corresponds exactly to the scalar transfer function  $H_0$ . So, considering an additive uncertainty  $\Delta = \Delta_0 + \delta\Delta$  yields the condition

$$\arg(\delta\Delta(j\omega)) = \arg \left( -\frac{1 + H_0(j\omega)}{G_{22}(j\omega)} \right) \quad (8a)$$

$$\|\delta\Delta(j\omega)\| < \left\| \frac{H_0(j\omega) + 1}{G_{22}(j\omega)} \right\| \quad (8b)$$

to guarantee the stability of the system.

Eqs. (8) result in two requirements on the parameters  $\mathbf{P}$  that must be met to have stability at frequency  $\omega$ . At each frequency, Eqs. (8) define a region of acceptable values in the parameter space. The knowledge of this region can be very helpful for the designer, especially when dealing with elements that present a wide range of characteristics dependent on several factors like environmental or operating conditions, wear and so on.

This type of analysis is quite attractive because it is performed in the traditional, often familiar frequency domain. In fact only frequency response data are required, opening the door to complementing numerical models with experimental data. A similar process can be employed also for Multiple-Input Multiple-Output (MIMO) systems using the E-contour techniques to compute the eigenvalues uncertainty regions at each frequency [28,29]. This aspect will not be pursued further in the present work since the main interest is on SISO applications only.

Further margins can be considered by requiring the uncertain bounds to allow some residual distance from point  $(-1 + j0)$ . This can be obtained by first computing the critical direction  $\theta$  that leads from point  $\lambda$  to point  $(-1 + j0)$ , namely

$$d = -\frac{1 + \lambda}{\|1 + \lambda\|} = e^{j\theta} \quad (9)$$

Then, a new uncertainty amplitude  $\hat{\rho}$ , that leaves a prescribed margin  $\tilde{\rho}$  along the critical direction, is considered,

$$\hat{\rho} = \rho - \tilde{\rho} \quad (10)$$

with  $\hat{\rho} \geq 0$ . As shown in Fig. 3, this corresponds to considering the distance  $\rho$  of the eigenvalue from the point  $(-1 + j0)$ , along the critical direction  $\theta$ , and restricting the limit value in such a way that, when at the boundary, a distance  $\tilde{\rho}$  remains.

### 3. Biodynamic Feedthrough

It is known that the BDFT dynamics depend on many different factors, such as vehicle dynamics, amplitude and frequency content of the input acceleration, seating characteristics and control device dynamics [1,17]. However, the most complex source of influence is the human operator or, more precisely, the varying limb dynamics of the human operator [21,12]. A very preliminary characterization of rotorcraft pilot's BDFT can be found in Ref. [30].

Limb dynamics not only do vary from pilot to pilot, but can also vary over time, depending for example on the control task the pilot is performing. It is known that these limb dynamics influence the BDFT. In other words, BDFT depends on the way the human is interacting with the vehicle. For example, when a pilot stiffens his muscles and increases grip on the control devices, this alters the way accelerations are fed through his body and thus modify the BDFT. More detailed information can be found in Ref. [23] where an experimental activity developed at Delft University of Technology and applied to helicopters is discussed. To understand the influence of the control task, biodynamic feedthrough was measured for different limb neuromuscular conditions, using an experimental method described in Ref. [12].

### 3.1. Delft experiments on helicopter pilots

The experiment is elaborately described in Ref. [23] and briefly summarized in the following for convenience. The experiment was performed on the SIMONA Research Simulator of Delft University of Technology, a six degree-of-freedom flight simulator. The control devices were electrically actuated collective and cyclic controls with adjustable dynamics settings. The settings used for each control axis were based on Ref. [31] and are listed in Table 1. The seat in which the subjects were seated had a 5-point safety belt that was adjusted tightly. Performance information could be displayed on a 15 in. LCD screen in front of the subject, shown in Fig. 4.

Table 1. Control device dynamical settings

Axis	Inertia (N s <sup>2</sup> /deg)	Damping (N s/deg)	Stiffness (N/deg)
Cyclic pitch	0.0369	0.0514	1.8340
Cyclic roll	0.0162	0.0516	1.8100
Collective	0.0152	0.0447	1.7950

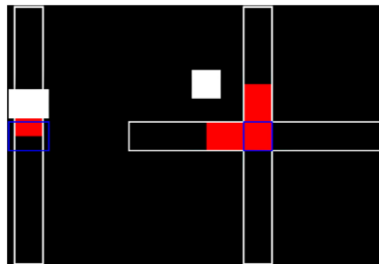


Fig. 4. Display presented to the subject. On the left the collective, on the right the cyclic (roll in horizontal and pitch in vertical direction). The figure shows the collective slightly above target value of 50%. The cyclic is slightly deflected to the left and forward.

During the experiment, two disturbance signals were used simultaneously: an acceleration disturbance  $M_{\text{dist}}(t)$ , applied to the simulator, and a force disturbance  $F_{\text{dist}}(t)$ , applied to the control devices. Using the acceleration disturbance  $M_{\text{dist}}(t)$ , the BDFT dynamics were determined; the force disturbance  $F_{\text{dist}}(t)$  was used to obtain neuromuscular admittance.

The measurements were performed for three disturbance directions (DIR): lateral (LAT), longitudinal (LNG) and vertical (VRT). In the lateral condition,  $F_{\text{dist}}(t)$  was applied to the cyclic in the roll direction (left-right) and  $M_{\text{dist}}(t)$  consisted in a lateral acceleration disturbance signal. In the longitudinal condition,  $F_{\text{dist}}(t)$  was applied to the cyclic in the pitch direction (forward-backward) and  $M_{\text{dist}}(t)$  consisted in a longitudinal acceleration disturbance signal. In the vertical condition  $F_{\text{dist}}(t)$  was applied to the collective in the vertical direction (up-down) and  $M_{\text{dist}}(t)$  consisted in a vertical acceleration disturbance signal.

The subjects were instructed to perform three disturbance rejection tasks (TSK) [32]:

1. the position task (PT), in which the instruction is to keep the position of the side-stick in the centred position, that is, to “resist the force perturbations as much as possible”;
2. the force task (FT), in which the instruction is to minimize the force applied to the side-stick, that is, to “yield to the force perturbations as much as possible”;
3. the relax task (RT), in which the instruction is to relax the arms while holding the control devices, that is, to “passively undergo the perturbations”.

For the PT the best performance was achieved by being very stiff (low admittance). The FT required the operator to be very compliant (high admittance). The RT yielded an admittance reflecting the passive dynamics of the neuromuscular system. Subjects were trained for each task before the experiment started. In earlier studies, it was shown that neuromuscular admittance and BDFT strongly depend on these control tasks [21,12]. The three tasks combined with the three directions result in a  $3 \times 3$  repeated measures design; each condition was repeated 6 times. During the experiment the angular deflection of the side-stick  $\theta_{CD}$  and the force applied to the side-stick  $F_C$  were measured.

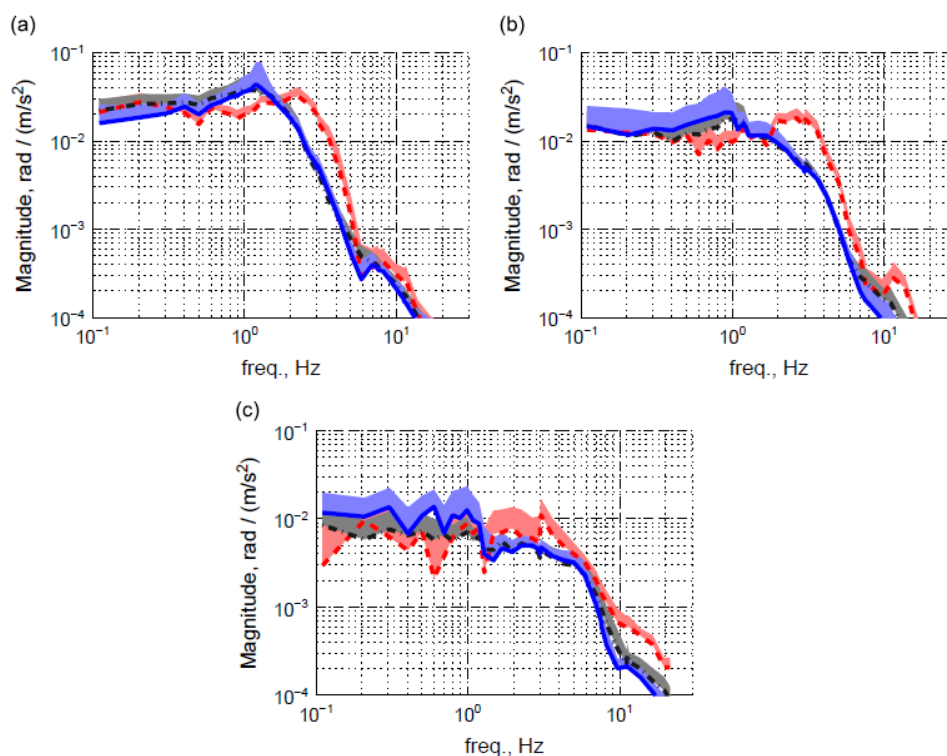


Fig. 5. Biodynamic feedthrough amplitude. (a) lateral; (b) longitudinal; (c) vertical. Dashed line: position task; dot dashed line: relax task; solid line: force task. The lines indicate the means over all subjects; the coloured (shaded) bands indicate the standard deviation. (For interpretation of the references to colour in this figure caption, the reader is referred to the web version of this article.)

The results of these measurements are an estimate of the BDFT dynamics, applicable to helicopters, in three different directions (lateral, longitudinal, vertical), for three different settings of the limbs ('stiff', 'compliant', 'passive'). The magnitude of the BDFT estimates thus

obtained is shown in Fig. 5 (see also Ref. [23]). It can be easily seen that the BDFT varies per control task and per direction. The BDFT dynamics plotted in Fig. 5 can be interpreted as the amount of involuntary control device deflection caused by vehicle acceleration in one direction. In the vertical direction, one could write

$$\psi_{\text{BDFT}}(s) = H_{\psi\ddot{z}}(s)\ddot{z}(s) \quad (11)$$

where  $\psi_{\text{BDFT}}$  is the involuntary contribution to the deflection of the collective control inceptor, measured in radian, and  $\ddot{z}$  is the vertical acceleration of the helicopter in  $\text{m/s}^2$ . The function  $H_{\psi\ddot{z}}$  is a transfer function describing the BDFT in the vertical direction, as plotted in the bottom subfigure of Fig. 5. Note again that  $H_{\psi\ddot{z}}$  depends on the control task that is being performed.

Evidently, a similar relationship can be written for the lateral and longitudinal direction. Therefore, the BDFT data shown in Fig. 5 can be interpreted as transfer functions with vehicle acceleration as input and the involuntary control device deflection as output. Note that a vehicle model has exactly the inverse input/output relationship: it describes the relationship between control device deflection  $\psi$  as input and vehicle motion (e.g. displacement, or acceleration) as output. By combining the BDFT data with the vehicle model the stability of the closed-loop system can be evaluated. In the present work the robust stability analysis is applied to the experimental BDFT data by plotting the stability limits of the vehicle together with the data shown in Fig. 5. This way, it is possible to assess the impact of BDFT dynamics on the closed-loop stability of the helicopter in three directions and for a range of limb dynamics.

### 3.2. Mayo's analytical biodynamic feedthrough model

To illustrate the power of robust stability analysis the vertical BDFT model for helicopters proposed by Mayo in Ref. [30] can be used. In this way the insights that can be gained from the robust stability approach are easily illustrated using a very simple model. Improved models that also take into account the different settings of the neuromuscular system can be found in Ref. [33].

Data	Ectomorphic	Mesomorphic
$\omega_p$ (rad/s)	21.267	23.567
$\xi_p$	0.322	0.282
$\tau_p$ (s)	0.118	0.108

Table 2. Data for function  $H_{\psi\ddot{z}}$  from Mayo's models.

The transfer functions proposed by Mayo describe the absolute vertical acceleration of the pilot's left hand as a function of the absolute vertical acceleration applied to the pilot's seat,

$\ddot{z}_h(s) = H_{\ddot{z}_h \ddot{z}_p}(s) \ddot{z}_p$ . Mayo identified two functions from two relatively homogeneous sets of persons, called 'ectomorphic' (small size) and 'mesomorphic' (large size),

$$H_{\ddot{z}_h \ddot{z}_p \text{ ecto}}(s) = \frac{5.19s + 452.3}{s^2 + 13.70s + 452.3} \quad (12a)$$

$$H_{\ddot{z}_h \ddot{z}_p \text{ meso}}(s) = \frac{4.02s + 555.4}{s^2 + 13.31s + 555.4} \quad (12b)$$

We are interested in the rotation of the collective control inceptor; as described for example in Refs. [34,11], this requires to subtract the absolute acceleration of the seat from the absolute acceleration of the hand, to obtain the relative acceleration of the hand. Furthermore, the division by the length of the collective control inceptor,  $L_\psi$ , yields an estimate of the angular acceleration, which, after double integration, results in the rotation of the collective,  $\psi$ , namely

$$H_{\psi \ddot{z}_p}(s) = \frac{H_{\ddot{z}_h \ddot{z}_p}(s) - 1}{s^2 L_\psi} \quad (13)$$

In the case of Mayo's functions,  $H_{\psi \ddot{z}_p}$  becomes

$$H_{\psi \ddot{z}_p}(s) = -\frac{1}{s L_\psi} \frac{s + 1/\tau_p}{s^2 + 2\xi_p \omega_p s + \omega_p^2} \quad (14)$$

with data from Table 2.

### 3.3. Biodynamic feedthrough from multibody simulation

Experimentally evaluated biodynamic feedthrough, and transfer functions obtained therein by system identification of time or frequency response, is a fundamental tool for the characterization of pilots and pilot-vehicle interface (both in terms of cockpit and control device layout). As discussed in subsequent sections, a simple graphical method is proposed to provide the analyst and the designer fundamental indications about vehicle proneness to RPC and sensitivity to various design parameters.

A significant drawback of the experimental approach is the actual need to perform experiments, which is expensive, time consuming, and requires the design and the manufacturing of the actual cockpit and control device layout that needs to be tested.

As an alternative, a reliable numerical model of the pilot's biodynamical behaviour would make it possible to evaluate in advance, and with minimal effort, the BDFT of a new configuration, or to understand the effects of cockpit and control device design modifications on the proneness to RPC for a given vehicle.

For this purpose, in WP3 a detailed multibody model of the pilot's arm has been developed and used to determine the biodynamic feedthrough and neuromuscular admittance that support the study of aeroservoelastic RPCs. Such analysis is not repeated in this deliverable; the reader should refer to Chapter 4 of D3.6 and to [48,49,50,51,52] for further details. The biodynamic feedthrough frequency response functions presented in that document can be used in the following in alternative to the experimental ones. Moreover, transfer functions can be estimated from them, cast in the same structure of Mayo's or in a more appropriate one, and used for the determination of the stability margins with respect to specific parameters.

#### 4. Application to rotorcraft–pilot coupling

The application of robust stability to the analysis of RPC is illustrated by considering a simple SISO problem. Consider a linearized rotorcraft model that describes the vertical displacement of the vehicle,  $z$ , as a function of the collective pitch of the rotor blades,  $\theta_0$ , namely

$$z(s) = H_{z\theta}(s)\theta_0(s) \quad (15)$$

The simplest possible model is (see [35, Chapter 3])

$$z(s) = \frac{Z_{/\theta}}{s^2m - sZ_{/\dot{z}}}\theta_0(s) \quad (16)$$

where  $m$  is the overall rotorcraft mass and  $Z$  is the rotor thrust;  $Z_{/\theta}$  and  $Z_{/\dot{z}}$  are its derivatives with respect to the blade collective pitch,  $\theta_0$ , and the vertical velocity,  $\dot{z}$  (note that  $Z_{/\theta} > 0$ , while  $Z_{/\dot{z}} < 0$ ). A similar model, that only differs in the output, yields the vertical motion of the pilot's seat,  $z_p$ , namely

$$z_p(s) = H_{z_p\theta}(s)\theta_0(s) \quad (17)$$

When the simple rigid model of Eq. (16) is considered,  $H_{z_p\theta}(s) \equiv H_{z\theta}(s)$ . Three instances of the function  $H_{z_p\theta}$  of Eq. (17) are used in this section, all based on data representative of the Sud Aviation SA330 Puma helicopter (data taken from Ref. [35, p. 270]). The oversimplified model of Eq. (16), called 'rigid' in the following, along with another model, called 'coning', which differs from the 'rigid' one because of the presence of the main rotor coning mode, is used to show some features of the proposed approach. For this second model the dynamics equations are

$$(s^2m - sZ_{/\dot{z}})z(s) + (s^2S_{\beta z} + sZ_{/\dot{\beta}})\beta(s) = Z_{/\theta}\theta_0(s) \quad (18a)$$

$$(s^2 I_\beta + s B_{/\dot{\beta}} + B_{/\beta})\beta(s) + (s^2 S_{\beta z} + s B_{/\dot{z}})z(s) = B_{/\theta}\theta_0(s) \quad (18b)$$

where  $\beta$  is the rotor coning angle and  $B$  is the rotor blade flap bending moment. Details on the values of the different coefficients can be found in Ref. [35, pp. 265–266].

Numerical results obtained using a rather complex aeroservoelastic model are also presented to illustrate how the complexity of the model, although fully reflected in the numerical results, has no impact on the complexity of the analysis. The model, called ‘puma’, was obtained using the MASST linearized rotorcraft analysis code [36,37].

At this stage it is worth stressing that the main reason for considering the SA330 in the present analysis is related to the public availability of the data required to prepare a realistic aeroelastic model, as the SA330 is not specifically known to suffer from collective bounce problems. Aeroelastic data for the main rotor have been obtained from Ref. [38].

The collective pitch  $\theta_0$  input into the control system can be partitioned in two contributions,

$$\theta_0(s) = \theta_{0ap}(s) + \theta_{0pp}(s), \quad (19)$$

one resulting from the voluntary control of the pilot,  $\theta_{0ap}$ , and one resulting from the involuntary control of the pilot,  $\theta_{0pp}$ . The latter represents input resulting from BDFT, the main focus of this work.

The model of Eqs. (C.15) and (C.17) can be recast in LFT form by simply setting  $\mathbf{y} = z$ ,  $\mathbf{u} = \theta_{0ap}$ ,  $\eta = z_p$ ,  $\zeta = \theta_{0pp}$ , and  $\mathbf{G}_{11} = \mathbf{G}_{12} = H_{z\theta}$ ,  $\mathbf{G}_{21} = \mathbf{G}_{22} = H_{z_p\theta}$ . The model that describes the involuntary control of the pilot is considered the uncertain part of the model; it provides the rotation of the collective,  $\psi$ , as a function of the vertical acceleration of the seat,  $\ddot{z}_p$ , namely

$$\psi(s) = H_{\psi\ddot{z}_p}(s)\ddot{z}_p \quad (20)$$

The transfer function between the vertical acceleration of the pilot and the main rotor collective pitch is obtained by multiplying the output of the function  $H_{\psi\ddot{z}_p}$  by a gearing ratio  $G_c$  that converts the rotation of the collective control inceptor into the corresponding pitch rotation of the blades. The nominal value for  $G_c$  is 0.35. The closure of the LFT loop is obtained by setting  $\Delta(s) = -G_c H_{\psi\ddot{z}_p}(s)s^2$ , under the assumption that  $H_{\psi\ddot{z}_p}$  is stable for any allowable choice of the uncertain parameters, which corresponds to setting

$$\theta_{0pp}(s) = \underbrace{G_c H_{\psi\ddot{z}_p}(s)s^2}_{-\Delta(s)} z_p(s) \quad (21)$$

where  $s$  differentiates twice the position of the pilot's seat,  $z_p$ , to yield its acceleration.

The degree of uncertainty of the properties of the vehicle, namely  $H_{z\theta}$ ,  $H_{z_p\theta}$ ,  $G_c$  and so on, is usually much less than that of the involuntary pilot's behaviour,  $H_{\psi\ddot{z}_p}$ . The transfer function  $H_{\psi\ddot{z}_p}$  can be obtained from the literature, e.g. by manipulating the functions identified by Mayo [30] as discussed in Ref. [11], or using those proposed in Ref. [11]; in this work the experimental BDFT data measured in Ref. [23] are used.

A minimal involuntary pilot control transfer function is...0! In fact, when a 'rigid' pilot holds the collective inceptor infinitely firmly, no relative rotation of the inceptor caused by the acceleration occurs. Alternatively, when the pilot releases the inceptor, thus decoupling the acceleration of the vehicle from the control inceptor through the pilot's body, and the centre of mass of the inceptor is located on its hinge's axis, the rotation of the inceptor does not depend on the vertical acceleration of the pilot. As a consequence,  $\Delta_0 = 0$ .

Since this simple problem involves a SISO system, the transfer matrix  $\mathbf{H}$  degenerates into the scalar

$$\chi(\omega) = H_{z_p\theta}(j\omega)G_cH_{\psi\ddot{z}_p}(j\omega)\omega^2 \quad (22)$$

According to Eq. (C.4), since the reference value  $\chi_0(\omega) = \lambda(\omega)$  is exactly 0, then  $\chi(\omega) = \rho(\omega)e^{j\theta(\omega)}$ . The resulting limiting condition  $\chi_{\text{limit}} = -1$ , i.e.  $\rho_1 = 1$  and  $\theta_1 = -\pi$ , corresponds to the usual Bode stability criterion, a special case of Nyquist's. As a consequence, the limit function

$$H_{\psi\ddot{z}_p\text{limit}}(j\omega) = -\frac{1}{\omega^2 G_c H_{z_p\theta}(j\omega)} \quad (23)$$

is obtained.

No instability is possible if the magnitude of the passive pilot model never exceeds that of the limit function of Eq. (23), shown in Fig. 6 for the simple models discussed earlier. Otherwise, the interaction with the passive pilot may result in instability when the phase of the passive pilot model matches that of the limit function of Eq. (23) and the magnitude of the passive pilot model exceeds that of the limit function. When the passive pilot model transfer function approaches any of the above limits, the likelihood of instability increases, or the stability margins reduce. For this reason, the combination of  $\rho$  and  $\theta$  can be interpreted as generalized stability margins.

#### 4.1. Mayo's model

As shown in Fig. 7, when the 'rigid' model of Eq. (16) is considered along with Mayo's pilot BDFT models, no instability appears to be possible, since the phase of the BDFT of the two

pilots is  $90^\circ$  for  $\omega \rightarrow 0$  and drops to  $0^\circ$  for  $\omega \rightarrow \infty$  because of the zero at  $-1/\tau_p$  and the two subsequent poles at  $(-\xi_p \pm j(1 - \xi_p^2)^{1/2})\omega_p$ , while the phase of the limit function

$$H_{\psi\ddot{z}_p,limit}(j\omega) = \frac{j\omega m - Z/\dot{z}}{j\omega G_c Z/\theta} \tag{24}$$

is  $-90^\circ$  for  $\omega \rightarrow 0$  because of the  $1/j\omega$  term, and raises to  $0^\circ$  for  $\omega \rightarrow \infty$  because of the zero at  $Z/\dot{z}/m$ ; as a consequence, the two functions only merge for  $\omega \rightarrow \infty$ , where the amplitude of the pilot models drop to zero and thus is well below the limits. Without an intersection between the phase curves of the limit function  $H_{\psi\ddot{z}_p,limit}$  and of the uncertainty operator  $H_{\psi\ddot{z}_p}$ , an unstable condition cannot occur whatever the ratio of the amplitudes.

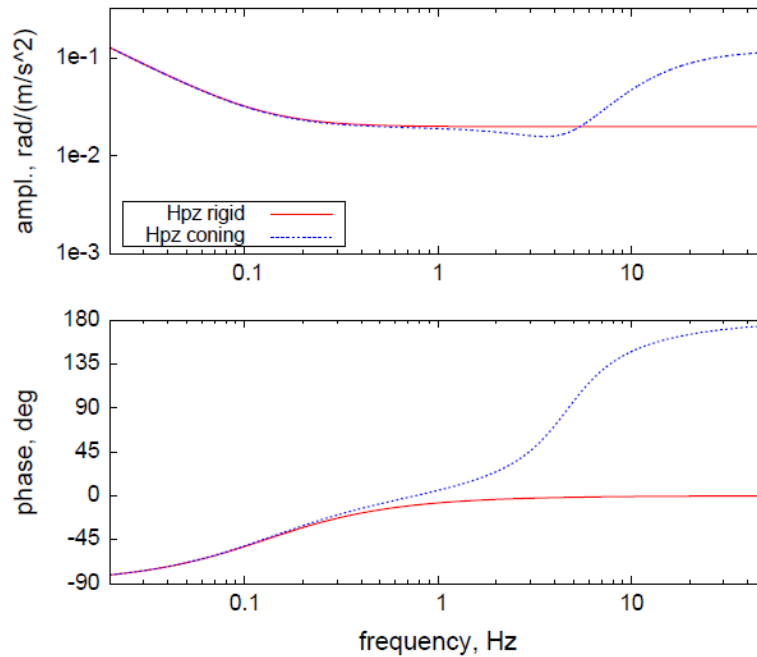


Fig. 6. Stability limits for the 'rigid' (Eq. (16)) and 'coning' (Eqs. (18)) models of the SA330 Puma.

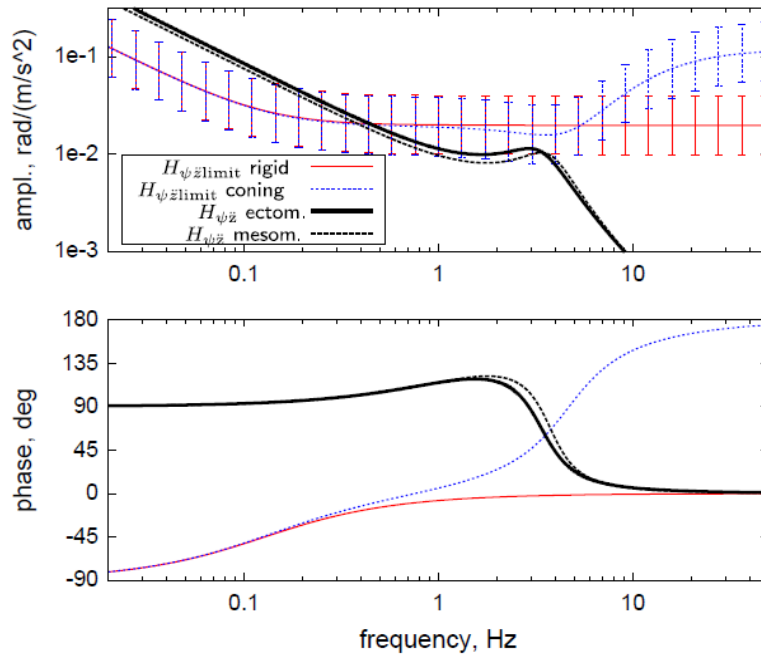


Fig. 7. Stability limits for the ‘rigid’ and ‘coning’ models of the SA330 Puma (Fig. 6) related to Mayo's ectomorphic pilot BDFT function; error bars indicate an uncertainty on the gearing ratio  $G_c$  ranging from 50% to 200% of the nominal value.

When the slightly more sophisticated ‘coning’ model is used, an unstable condition can occur in the vicinity of the intersection of the phase curves, provided the amplitude of the pilot's function is large enough. Fig. 7 shows Mayo's ectomorphic pilot model with an uncertainty on the gearing ratio  $G_c$ . This parameter is actually associated to the vehicle rather than to the pilot. However, it is considered the uncertain parameter in this analysis because the choice of the gearing ratio is typically based on considerations independent from BDFT and rather related to the rotorcraft handling qualities (see Ref. [35, Chapter 2]), although a lower limit may also be dictated by ergonomic considerations on the maximum excursion of the collective inceptor. Within reasonable bounds there is no specific need to define an upper limit, and for systems with a fly-by-wire FCS it is even possible to conceive a system with variable  $G_c$  depending on the mission task element the aircraft must accomplish.

An indirect experimental verification of this fact is presented in Ref. [39], which discusses the test campaign of an ‘aeroelastic’ two degree of freedom model performed in the flight simulator at University of Liverpool in July 2011. The heave motion of the helicopter was augmented by a second mode aimed at representing an internal elastic degrees of freedom, such as the ‘coning’ mode. Without the elastic mode, thus with a model essentially equivalent to that of Eq. (16), no PAO instability could be observed, while by carefully tuning the frequency and the damping of the elastic mode several PAO events could be observed by increasing the gearing ratio  $G_c$  as needed. By increasing  $G_c$  the modulus of the limit function of Eq. (23) reduces without affecting its phase.

Consider now in more detail the structure of the uncertainty. In fact, the structure of Eq. (14) for the passive pilot function depends on parameters like the frequency  $\omega_p$ , the damping factor  $\xi_p$ , and the time constant of the zero,  $\tau_p$ . The limit of Eq. (23) can be further

elaborated by replacing  $H_{\psi\ddot{z}_p}$  with its expression from Eq. (14) and then exposing, for example, the limit value of the damping factor,

$$\xi_{plimit} = \frac{\omega^2 - \omega_p^2 - j\omega \left( j\omega + \frac{1}{\tau_p} \right) \frac{G_c}{L_{\psi}} H_{z\theta}(j\omega)}{2\omega_p j\omega} \quad (25)$$

This function describes the value of  $\xi_p$  that brings the loop transfer function on top of the point  $(-1 + j0)$ . It is complex valued; as such, it can be plotted in the Argand plane, as shown in Fig. 8. However, only a real, positive damping factor makes sense for the transfer function of a passive pilot model. As a consequence, only values of  $\xi_p$  larger than the one that function  $\xi_{plimit}$  assumes when its value is purely real, corresponding to the critical direction, lead to a stable loop transfer function. In Fig. 8 it is shown that instability is actually possible using the simplified model of Eq. (16), although it requires a damping factor  $\xi_p < 0.045$ . When the rotor coning mode is considered, the limit damping factor is about 0.2.

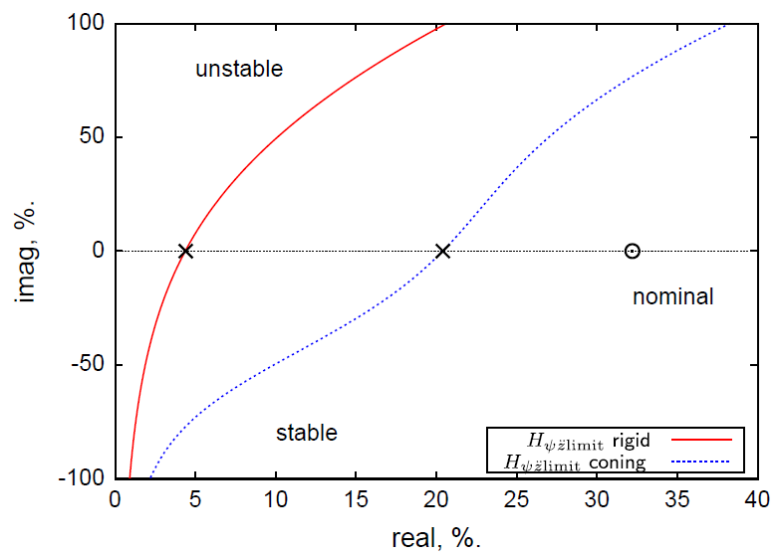


Fig. 8. Limit damping factor  $\xi_{plimit}$  for Mayo's ectomorphic pilot model.

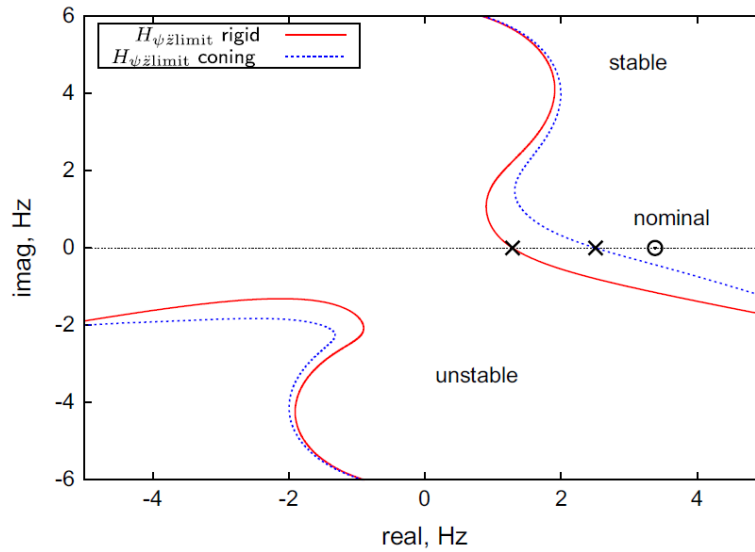


Fig. 9. Limit frequency  $\omega_{plimit}$  for Mayo's ectomorphic pilot model.

Similarly, the passive pilot frequency limit can be computed as

$$\omega_{plimit} = -j\omega\xi_p \pm \sqrt{\omega^2(1 - \xi_p^2) - j\omega \left( j\omega + \frac{1}{\tau_p} \right) \frac{G_c}{L_\psi} H_{z_p\theta}(j\omega)} \quad (26)$$

and plotted accordingly in the Argand plane as shown in Fig. 9. This figure suggests that a reduction in the pilot's frequency, obtained for example by increasing the inertia of the collective control inceptor using bobweights, would reduce the stability margin, unless accompanied by an increase in the damping. Unfortunately this conjecture cannot be confirmed because Mayo's functions do not allow to separate the admittance of the pilot from that of the control device. Ref. [20] presents an approach to investigate the effect of control device dynamics on BDFT dynamics. The limit frequency for the simplest model is 8.08 rad/s (about 1.3 Hz), while for the model that includes the rotor coning mode it is 15.75 rad/s (about 2.5 Hz).

Finally, the limit value of the passive pilot zero time constant is

$$\tau_{plimit} = \frac{j\omega \frac{G_c}{L_\psi} H_{z_p\theta}(j\omega)}{\left( 1 + \frac{G_c}{L_\psi} H_{z_p\theta}(j\omega) \right) \omega^2 - 2\xi_p \omega_p j\omega - \omega_p^2} \quad (27)$$

Its plot on the Argand plane is shown in Fig. 10. The limit values are approximately 17 ms for the simple model and 42 ms for the model that includes the rotor coning mode.

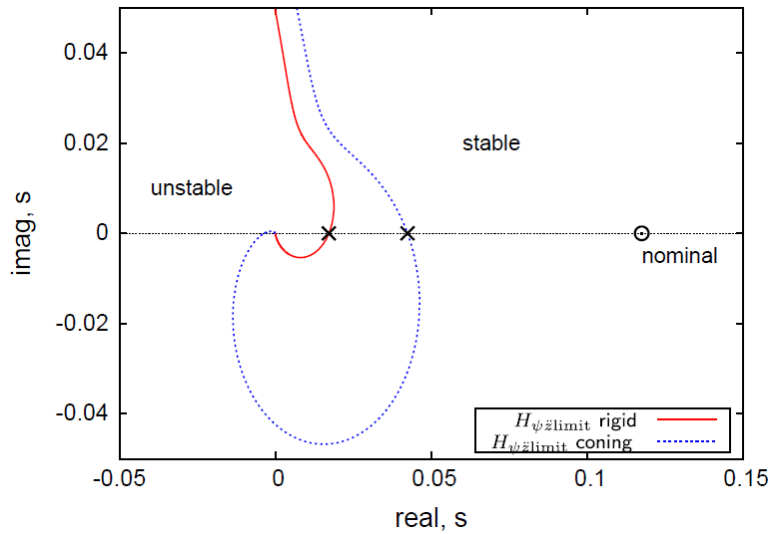


Fig. 10. Limit zero time constant  $\tau_{plimit}$  for Mayo's ectomorphic pilot model.

Fig. 11 shows the limit curves and the reference value in the space of the passive pilot's frequency  $\omega_p$  and damping factor  $\xi_p$ , for nominal zero time constant  $\tau_p$ . This plot is useful to understand whether the biomechanical properties of a specific pilot coupled to a specific collective inceptor layout, identified from a procedure like Mayo's, tend towards more or less stability. Since both parameters can be affected, at least in part, by acting on the dynamic properties of the collective control, this plot can be used for example to influence the design of passive devices. It clearly shows that a reduction of frequency not accompanied by an increase of damping can be detrimental.

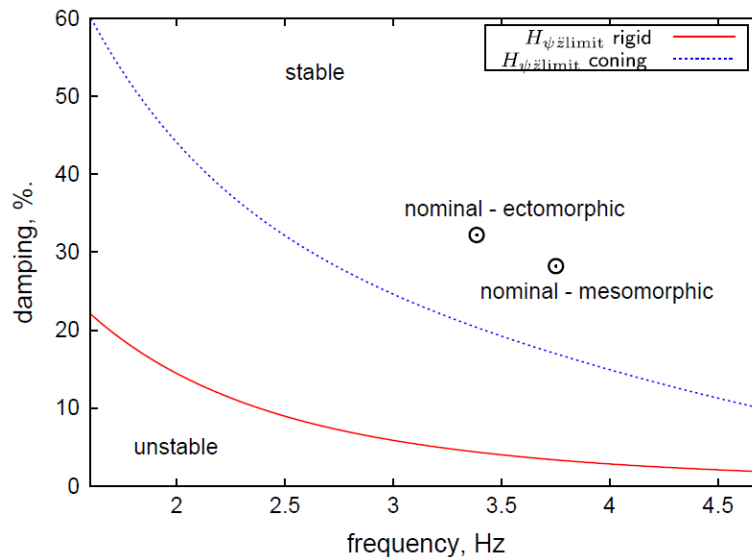


Fig. 11. Limit curves in the space of passive pilot's frequency  $\omega_p$  and damping factor  $\xi_p$  for Mayo's ectomorphic and mesomorphic pilot models.

It is interesting to note that the results presented by Mayo in Ref. [30] for the two types of persons, the ectomorphic and the mesomorphic, lie on a line loosely parallel to the limit curves. This justifies the fact that during prior tests (e.g. in Ref. [6]) the two datasets provided

very similar stability results, since they lie at about the same distance from either of the limit curves.

#### 4.2. Experimental biodynamic feedthrough

More sophisticated aeroservoelastic models of the vehicle can be used in a straightforward manner, as shown later in this section. The ‘puma’ model has been obtained in the form of the transfer function  $H_{z_p\theta}$  of Eq. (17) using the modelling environment MASST [36,37], which produces linearized aeroservoelastic rotorcraft models.

The aeroservoelastic model of the SA330 used in this work, consisting of the elastic airframe described by 6 normal modes, a linearized aeroelastic model of the main rotor with 3 bending and 2 torsion modes per blade, connected to the airframe using Craig-Bampton’s substructuring approach [40], and linear servoactuator dynamics for the swashplate actuators, has been presented and validated in Refs. [22,41]. The transfer function  $H_{z\theta}$  between the collective pitch control and the vertical acceleration of the helicopter model called ‘puma’ has been computed in three flight conditions: hover and forward flight at 50 kts and 100 kts, the corresponding Bode plots are shown in Fig. 12. A very broad spectrum is presented to highlight the complexity of the model and the differences at various operating conditions. However, it is worth noticing that the functions are very similar in the 1-10 Hz band, which is of interest for BDFT. As a consequence, very small differences can be expected in the stability limit curves.

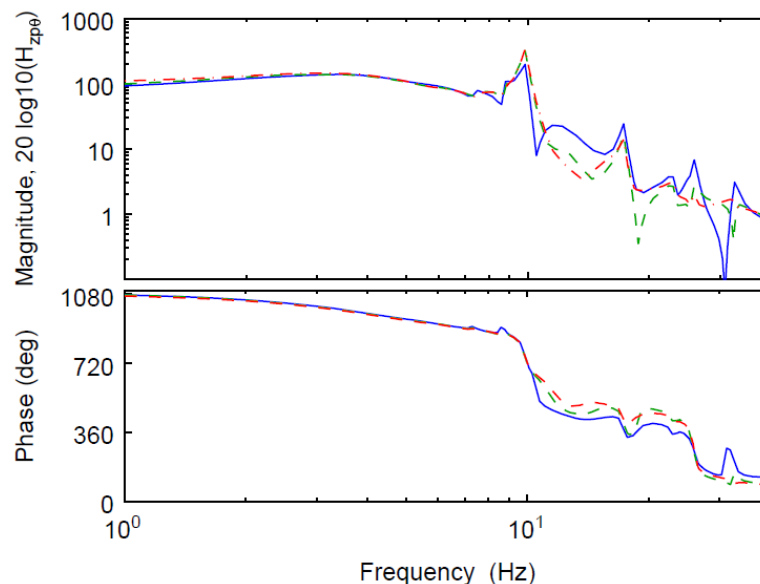


Fig. 12. Transfer function  $H_{z\theta}$  between collective pitch and vertical acceleration of the ‘puma’ model. The blue (solid) line is computed in hover, while the green (dashed) and red (dot dashed) lines are computed in forward flight, respectively, at 50 kts and 100 kts.

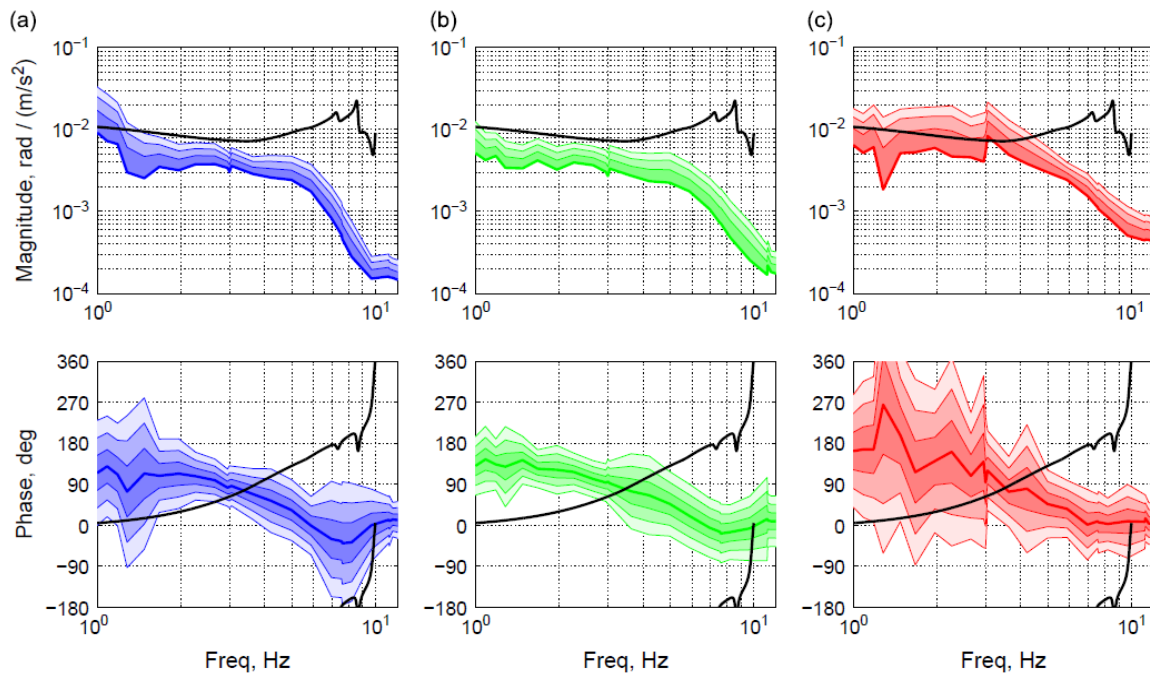


Fig. 13. Stability limits of the 'puma' model in hover related to pilot BDFT according to force (a), relax (b) and position (c) tasks.

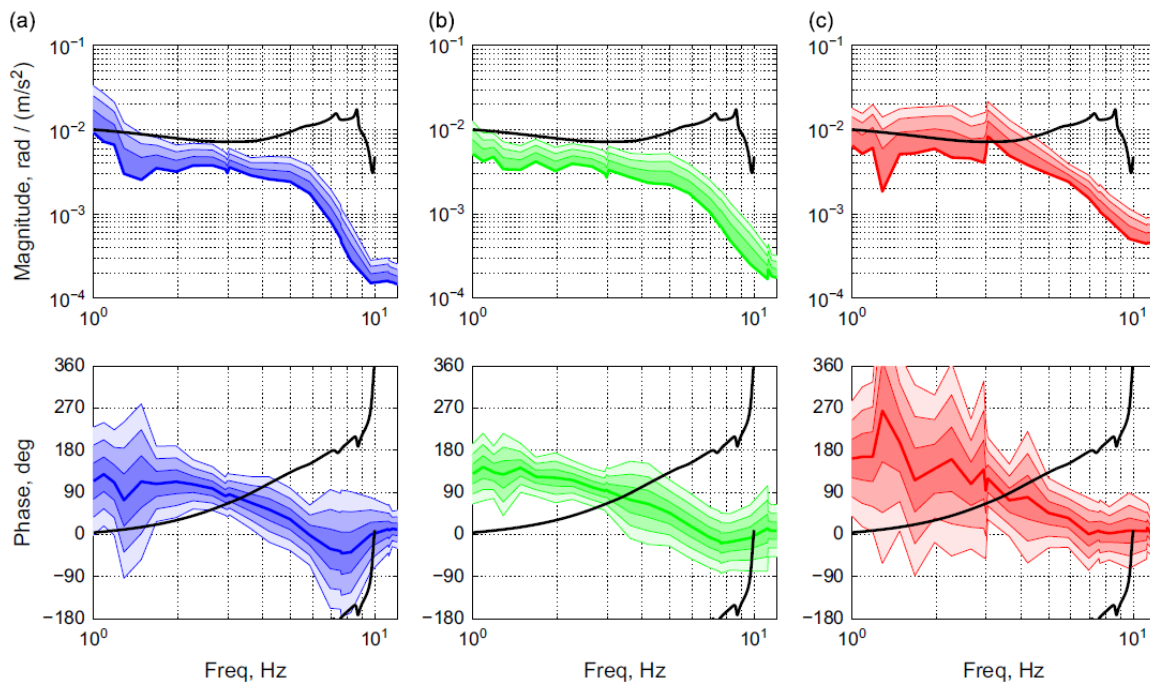


Fig. 14. Stability limits of the 'puma' model in forward flight ( $V_{\infty} 50 = \text{kts}$ ,  $\mu = 0.12$ ) related to pilot BDFT according to force (a), relax (b) and position (c) tasks.

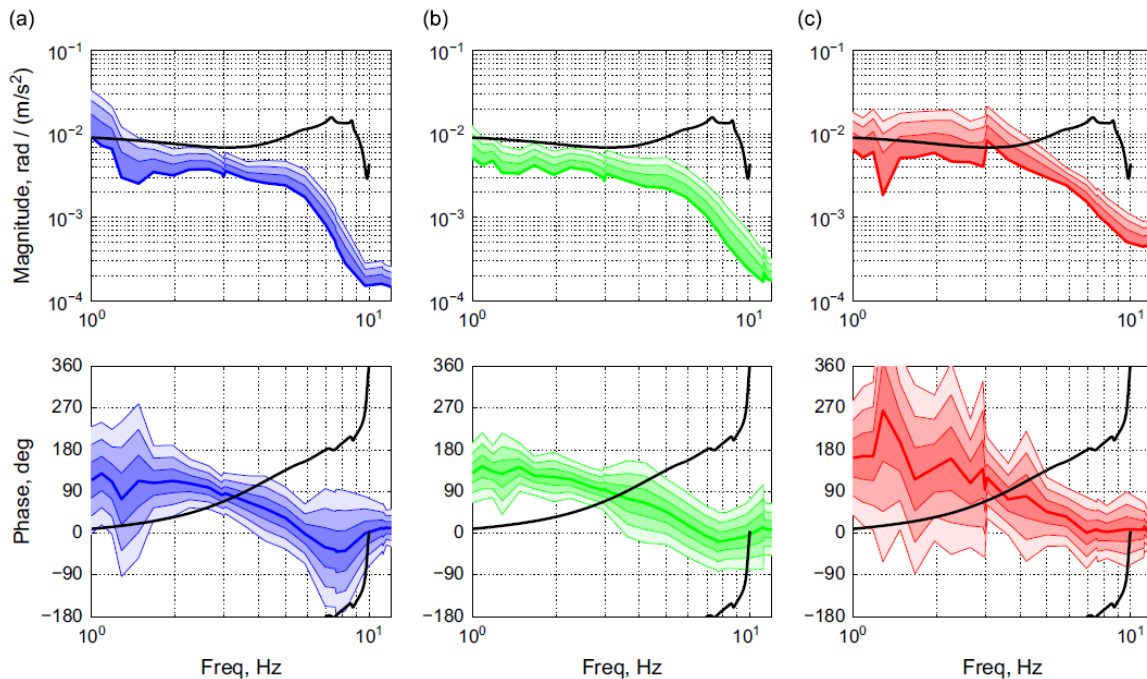


Fig. 15. Stability limits of the 'puma' model in forward flight ( $V_{\infty} 100 = \text{kts}$ ,  $\mu = 0.24$ ) related to pilot BDFT according to force (a), relax (b) and position (c) tasks.

Figs. 13–15 show how the stability limit of the complete rotorcraft model, the solid line, relates to the measured BDFT of the pilot while performing the three tasks considered in [23], namely the force, the relax and the position tasks in vertical direction. These data correspond to those shown in Fig. 5 (bottom). The pilot's BDFT amplitude curves consist of the mean resulting from the test (the lower limit of the shaded area) and the mean plus 1, 2, and 3 times the standard deviation (the upper limit), while the phase curves consist of the mean plus and minus 1, 2, and 3 times the standard deviation. Since the crossing between the phase curve of the pilot's BDFT and of the helicopter's stability limit is of the utmost importance, it has been decided to plot the BDFT curve and superimpose multiple instances of the stability limit curve shifted by multiples of  $2\pi$  ( $360^\circ$ ), to highlight the presence of such crossings.

Fig. 13 refers to the helicopter in hover, while Figs. 14 and 15 refer to forward flight, respectively at 50 kts and 100 kts. The possible interaction seems to be relatively independent from the flight condition, as qualitatively noted in [6].

BDFT measurements related to motion along the vertical axis are unreliable below 1 Hz because of low signal to noise ratio caused by too little travel in the vertical direction, or velocity saturation in the actuators when requested to achieve a certain level of acceleration at very low frequency. Moreover, below 0.5 Hz cognitive control actions may appear as noise in the BDFT estimate and therefore should be kept to a minimum. In any case, the intentional control of the pilot in this range of frequencies would eventually compensate a mild instability of the interaction with the vehicle. As a consequence, the potential instabilities below 1 Hz most likely do not directly represent a practical problem with respect to BDFT, although they might contribute to triggering other types of adverse RPCs (PIO).

In order to guarantee the stability of the interaction, either the BDFT amplitude curve has to remain always below the helicopter stability limit curve or there must be no phase crossing when the BDFT amplitude is above the stability limit curve.

Within 1 Hz and 10 Hz, the BDFT amplitude curves resulting from the force and the relax tasks are almost always below the stability limit curve of the helicopter. Slight chances of instability occur in the vicinity of 1 Hz for the force task, for pilot models with amplitude at the mean plus 2 times the variance. Instead, in the case of the position task the BDFT amplitude curve is occasionally above the stability limit curve of the helicopter. The mean value seldom is, with the notable exception of a peak at about 3 Hz, which is consistent with the peak amplitude of the curve from Mayo [30]. However, the mean plus standard deviation is often above the limit. When this happens, the band resulting from the mean plus/minus the standard deviation of the phase occasionally crosses the phase curve of the stability limit, resulting in a non-negligible probability of unstable interaction of the rotorcraft with the pilot in the 2–5 Hz band.

Further crossing of the phase curves occurs at about 10 Hz; however, in that case the amplitude stability margin is well above the BDFT amplitude, and thus the probability of unstable interactions is negligible.

In conclusion, the plots indicate that the same rotorcraft may show different levels of proneness to collective bounce depending on the neuromuscular dynamics of the pilot's body. The latter may be associated with the task the pilot is performing, or in a broader sense to the piloting attitude and the workload of the pilot. Furthermore, sudden changes of neuromuscular dynamics that may occur for example in reaction to unexpected events or emergencies may increase the proneness to collective bounce and act as triggers for other types of RPCs.

## 5. Conclusions

This work discussed the use of robust stability analysis to evaluate helicopter proneness to Rotorcraft–Pilot Couplings (RPC) considering analytical pilot biodynamic feedthrough (BDFT) models and experimental measurements.

The vehicle model is regarded as 'certain', in a robust analysis sense; in this sense, the method is applied to the verification of the proneness of a given design. The pilot behavior is regarded as the 'uncertain' portion of the system, again in a robust analysis sense. Similarly, portions of the pilot-vehicle interface (the cockpit and the control device layout) can be seen as certain or uncertain, and thus associated respectively with the vehicle or with the pilot.

The proposed approach is applied to increasingly complex models of helicopter collective bounce. This supports the following considerations:

1. the proposed approach highlights the dependence and sensitivity of rotorcraft models to pilot BDFT;
2. when an analytical BDFT model is used, sensitivity to specific parameters of the model can be evaluated;

3. when numerical or experimental frequency response data are available, proneness to RPC can be assessed using a very simple and practical graphical approach.

## References

- [1] R.W. McLeod, M.J. Griffin, Review of the effects of translational whole-body vibration on continuous manual control performance, *Journal of Sound and Vibration* 133 (1) (1989) 55–115, [http://dx.doi.org/10.1016/0022-460X\(89\)90985-1](http://dx.doi.org/10.1016/0022-460X(89)90985-1).
- [2] M. Abzug, E. Larrabee, *Airplane Stability and Control: a History of the Technologies that Made Aviation Possible*, 2nd ed. Cambridge University Press, 2002.
- [3] D.T. McRuer, *Aviation Safety and Pilot Control: Understanding and Preventing Unfavourable Pilot-Vehicle Interactions*, National Research Council, National Academy Press, Washington, DC, 1997.
- [4] D.G. Mitchell, D.H. Klyde, Recommended practices for exposing pilot-induced oscillations or tendencies in the development process, USAF Developmental Test and Evaluation Summit, Woodland Hills, CA, 2004, pp. 1–20, AIAA 2004-6810.
- [5] M.D. Pavel, J. Malecki, B. DangVu, P. Masarati, G. Quaranta, M. Gennaretti, M. Jump, H. Smaili, A. Ionita, L. Zaicek, *Aircraft and rotorcraft pilot coupling: a survey of recent research activities within the European project ARISTOTEL*, 3rd CEAS Air & Space Conference, Venice, Italy, 2011.
- [6] J. Serafini, M. Gennaretti, P. Masarati, G. Quaranta, O. Dieterich, *Aeroelastic and biodynamic modeling for stability analysis of rotorcraft–pilot coupling phenomena*, 34th European Rotorcraft Forum, Liverpool, UK, 2008.
- [7] R.A. Hess, *Modeling biodynamic interference in helicopter piloting tasks*, American Helicopter Society Aeromechanics Specialists' Conference, San Francisco, CA, 2010.
- [8] I.L. Ashkenas, H.R. Jex, D.T. McRuer, *Pilot-induced Oscillations: Their Cause and Analysis*, NCR 64-143, Norair Report, June 20, 1964.
- [9] C.H. Lewis, M.J. Griffin, Mechanisms of the effects of vibration frequency, level and duration on continuous manual control performance, *Ergonomics* 22(7) (1979) 855–889.
- [10] S. Sövényi, R. Gillespie, Cancellation of biodynamic feedthrough in vehicle control tasks, *IEEE Transactions on Control Systems Technology* 15 (6) (2007) 1018–1029.
- [11] P. Masarati, G. Quaranta, M. Jump, Experimental and numerical helicopter pilot characterization for aeroelastic rotorcraft–pilot couplings analysis, *Proceedings of IMechE, Part G: Journal of Aerospace Engineering* 227 (1) (2013) 124–140, <http://dx.doi.org/10.1177/0954410011427662>.
- [12] J. Venrooij, D.A. Abbink, M. Mulder, M.M. van Paassen, M. Mulder, A method to measure the relationship between biodynamic feedthrough and neuromuscular admittance, *IEEE Transactions on Systems, Man, and Cybernetics, Part B: Cybernetics* 41 (4) (2011) 1158–1169, <http://dx.doi.org/10.1109/TSMCB.2011.2112347>.
- [13] T. Parham Jr., D. Popelka, V-22 pilot-in-the-loop aeroelastic stability analysis, American Helicopter Society 47th Annual Forum, Phoenix, AZ, USA, 1991.
- [14] R.B. Walden, A retrospective survey of pilot-structural coupling instabilities in naval rotorcraft, American Helicopter Society 63rd Annual Forum, Virginia Beach, VA, 2007, pp. 1783–1800.
- [15] R.W. Prouty, A.R. Yackle, The Lockheed AH-56 Cheyenne—lessons learned, AIAA Aircraft Design Systems Meeting, Hilton Head, SC, USA, 1992, AIAA-1992-4278.
- [16] R.L. Bielawa, *Rotary Wing Structural Dynamics and Aeroelasticity*, AIAA, Washington, DC, 1992.

- [17] M.J. Griffin, *Handbook of Human Vibration*, Academic Press, London, 1990.
- [18] M.G. Toward, M.J. Griffin, Apparent mass of the human body in the vertical direction: inter-subject variability, *Journal of Sound and Vibration* 330 (4) (2011) 827–841.
- [19] M.G. Toward, M.J. Griffin, The transmission of vertical vibration through seats: influence of the characteristics of the human body, *Journal of Sound and Vibration* 330 (26) (2011) 6526–6543.
- [20] J. Venrooij, M. Mulder, D.A. Abbink, M.M. van Paassen, M. Mulder, F.C.T. van der Helm, H.H. Bühlhoff, A new view on biodynamic feedthrough analysis: unifying the effects on i forces and positions, *IEEE Transactions on Systems, Man, and Cybernetics, Part B: Cybernetics* 43 (1) (2013) 129–142.
- [21] J. Venrooij, D.A. Abbink, M. Mulder, M.M. van Paassen, M. Mulder, Biodynamic feedthrough is task dependent, 2010 IEEE International Conference on Systems Man and Cybernetics (SMC), Istanbul, Turkey, 2010, pp. 2571–2578, <http://dx.doi.org/10.1109/ICSMC.2010.5641915>.
- [22] V. Muscarello, P. Masarati, G. Quaranta, Robust aeroservoelastic analysis for the investigation of rotorcraft pilot couplings, 3rd CEAS Air & Space Conference, Venice, Italy, 2011.
- [23] J. Venrooij, D. Yilmaz, M.D. Pavel, G. Quaranta, M. Jump, M. Mulder, Measuring biodynamic feedthrough in helicopters, 37th European Rotorcraft Forum, Gallarate, Italy, 2011, pp. 199.1–12.
- [24] J.C. Cockburn, B.G. Morton, Linear fractional representations of uncertain systems, *Automatica* 33 (7) (1997) 1263–1271, [http://dx.doi.org/10.1016/S0005-1098\(97\)00049-6](http://dx.doi.org/10.1016/S0005-1098(97)00049-6).
- [25] S. Skogestad, I. Postlethwaite, *Multivariable Feedback Control*, John Wiley & Sons, Chichester, 2005.
- [26] C. Desoer, Y. Wang, On the generalized Nyquist stability criterion, *IEEE Transactions on Automatic Control* 25 (2) (1980) 187–196.
- [27] O.N. Gasparyan, *Linear and Nonlinear Multivariable Feedback Control*, John Wiley & Sons, Ltd, 2008.
- [28] R. Daniel, B. Kouvaritakis, A new robust stability criterion for linear and non-linear multivariable feedback systems, *International Journal of Control* 41 (6) (1985) 1349–1379.
- [29] B. Kouvaritakis, H. Latchman, Singular-value and eigenvalue techniques in the analysis of systems with structured perturbations, *International Journal of Control* 41 (6) (1985) 1381–1412.
- [30] J.R. Mayo, The involuntary participation of a human pilot in a helicopter collective control loop, 15th European Rotorcraft Forum, Amsterdam, The Netherlands, 1989, pp. 81.1–12.
- [31] D. Mitchell, R. Hoh, A.J. Adolph, D. Key, Ground based Simulation Evaluation of the Effects of Time Delays and Motion on Rotorcraft Handling Qualities, Technical Report USAAVSCOM TR 91-A-010, AD-A256 921, January 1992.
- [32] D.A. Abbink, *Neuromuscular Analysis of Haptic Gas Pedal Feedback During Car Following*, PhD Thesis, Delft University of Technology, 2006.
- [33] J. Venrooij, M. D. Pavel, M. Mulder, F. C. T. van der Helm, H. H. Bühlhoff, A practical biodynamic feedthrough model for helicopters, 38th European Rotorcraft Forum, Amsterdam, The Netherlands, 2012, paper no. 096.
- [34] P. Masarati, G. Quaranta, M. Gennaretti, J. Serafini, An investigation of aeroelastic rotorcraft–pilot interaction, 37th European Rotorcraft Forum, Gallarate, Italy, 2011, paper no. 112.

- [35] G.D. Padfield, *Helicopter Flight Dynamics: The Theory and Application of Flying Qualities and Simulation Modelling*, Blackwell Publishing, 2007.
- [36] P. Masarati, V. Muscarello, G. Quaranta, Linearized aeroservoelastic analysis of rotary-wing aircraft, 36th European Rotorcraft Forum, Paris, France, 2010, pp. 099.1–10.
- [37] P. Masarati, V. Muscarello, G. Quaranta, A. Locatelli, D. Mangone, L. Riviello, L. Viganò, An integrated environment for helicopter aeroservoelastic analysis: the ground resonance case, 37th European Rotorcraft Forum, Gallarate, Italy, 2011, pp. 177.1–12.
- [38] W.G. Bousman, C. Young, F. Toulmay, N.E. Gilbert, R.C. Strawn, J.V. Miller, T.H. Maier, M. Costes, P. Beaumier, A Comparison of Lifting-line and CFD Methods with Flight Test Data from a Research Puma Helicopter, TM 110421, NASA, October 1996.
- [39] P. Masarati, G. Quaranta, L. Lu, M. Jump, Theoretical and experimental investigation of aeroelastic rotorcraft–pilot coupling, American Helicopter Society 68th Annual Forum, Fort Worth, TX, 2012.
- [40] R.R. Craig Jr., M.C.C. Bampton, Coupling of substructures for dynamic analysis, *AIAA Journal* 6 (7) (1968) 1313–1319.
- [41] V. Muscarello, P. Masarati, G. Quaranta, Multibody analysis of rotorcraft–pilot coupling, in: P. Eberhard, P. Ziegler (Eds.), *2nd Joint International Conference on Multibody System Dynamics*, Stuttgart, Germany, 2012.
- [42] G. Quaranta, P. Masarati, J. Venrooij, Robust Stability Analysis: a Tool to Assess the Impact of Biodynamic Feedthrough on Rotorcraft, 68th AHS Forum, Fort Worth, Texas, May 1-3, 2012.
- [43] P. Masarati, G. Quaranta, J. Venrooij, Impact of Pilot's Biodynamic Feedthrough on Rotorcraft by Robust Stability, *Journal of Sound and Vibration*, 332(20):4948-4962, September 2013, doi:10.1016/j.jsv.2013.04.020.
- [44] G. Quaranta, A. Tamer, V. Muscarello, P. Masarati, M. Gennaretti, J. Serafini, M. Molica Colella, Evaluation of Rotary Wing Aeroelastic Stability Using Robust Analysis, 38th ERF, Amsterdam, NL, September 4-7, 2012.
- [45] G. Quaranta, A. Tamer, V. Muscarello, P. Masarati, M. Gennaretti, J. Serafini, M. Molica Colella, Rotorcraft Aeroelastic Stability Using Robust Analysis, *CEAS Aeronautical Journal*, in press, doi:10.1007/s13272-013-0082-z.
- [46] P. Masarati, V. Muscarello, G. Quaranta, Robust Aeroservoelastic Stability of Helicopters: Application to Air/Ground Resonance, AHS 67th Annual Forum, Virginia Beach, VA, USA, May 3-5, 2011.
- [47] G. Quaranta, V. Muscarello, P. Masarati, Lead-Lag Damper Robustness Analysis for Helicopter Ground Resonance, *AIAA Journal of Guidance, Control, and Dynamics*, 36(4):1150-1161, July 2013, doi:10.2514/1.57188.
- [48] A. Zanoni, P. Masarati, G. Quaranta, Estimation of the Dependence of Upper Limb's Biomechanical Impedance on Muscular Activation, presented at IMSD 2012, Stuttgart, Germany, May 29-June 1, 2012.
- [49] A. Zanoni, P. Masarati, G. Quaranta, Rotorcraft Pilot Impedance from Biomechanical Model Based on Inverse Dynamics, ASME IMECE 2012, Houston, Texas, November 9-15, 2012.
- [50] P. Masarati, G. Quaranta, Coupled Bioaeroservoelastic Rotorcraft-Pilot Simulation, DETC2013-12035, ASME 9th MSNDC, Portland, OR, USA, August 4-7, 2013
- [51] P. Masarati, G. Quaranta, A. Zanoni, Dependence of Helicopter Pilots' Biodynamic Feedthrough on Upper Limbs' Muscular Activation Patterns, *Proc. IMechE Part K: J. Multi-body Dynamics*, doi:10.1177/1464419313490680, in press.
- [52] P. Masarati, G. Quaranta, Bioaeroservoelastic Analysis of Involuntary Rotorcraft-Pilot Interaction, *ASME J. Comput. Nonlinear Dyn.*, in press.

## Appendix D: Pilot-Vehicle System modelling requirements and RPC/PAO sensitivity to structural parameters (UROMA3)

### 1. Summary of Work Performed

The contribution of UROMA3 to the definition of guidelines that might be of help to designers to assess the susceptibility of new rotorcraft to adverse aeroservoelastic RPCs (and then prevent their occurrence) is twofold: (i) identification of modelling requirements for accurate and reliable RPC/PAO simulations, and (ii) analysis of parameters that are critical in terms of unfavourable rotorcraft-pilot coupling and aero-servo-elastic instabilities. It is based on the activities performed in WP3 and WP4, and extensively documented in deliverables D3.4, D3.9 and D4.11 (see Refs. [1-3]).

Specifically, concerning modelling requirements identification, the following main issues have been investigated:

- **rotor aerodynamics modelling** (with emphasis on unsteady, interaction, and three-dimensional effects);
- **rotor aeroelastic modelling** (with emphasis on identification of main rotor transfer functions and analysis of nonlinear terms effects);
- **passive pilot modelling** (workload dependent models).

Indeed, aerodynamics has a great impact on helicopter dynamics and stability, and it is well known that three-dimensional, unsteady and interactional effects (such as interaction between wakes and aerodynamic surfaces) may play a great role in flight mechanics. Focusing on RPC, aerodynamics may also trigger instability and limit cycle events. Two-dimensional, quasi-steady aerodynamics, although well known and widely used, do not take into account part of these effects and must be corrected with empirical formulas. However, these might not be very reliable and accurate, in that based on knowledge of data that could not be available during preliminary design. Approaches based on unsteady, three-dimensional aerodynamics may take into account most of these complex effects, thus yielding more accurate numerical simulations. Further, since the performance of solvers applied is a critical issue for the design process, part of the activity has been devoted to the identification of feasible mathematical modelling allowing the numerically efficient inclusion of complex aerodynamic solutions within the aeroelastic simulation of rotorcraft.

On the other hand, the sensitivity of RPC/PAO phenomena to variations of some critical system parameters has been examined for a light-weight helicopter and a medium-weight helicopter (the MBB BO105 and the IAR330 Puma, namely).

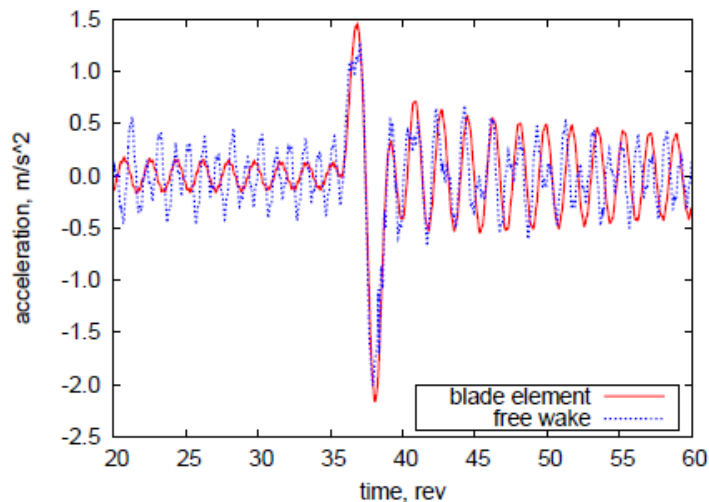
### 2. Results and Conclusions

The following sections presents the results of UROMA3 analysis aimed at defining design guidelines concerning, respectively, modelling requirements for accurate RPC/PAO simulations and impact of critical system parameters to RPC/PAO events.

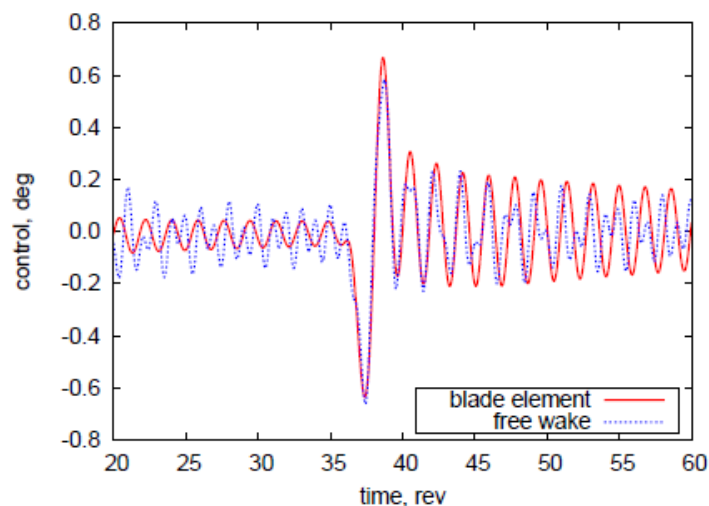
## 2.1 Analysis of modelling requirements

### Rotor Aerodynamic Modelling

Concerning main rotor aerodynamic modelling, RPC/PAO simulations obtained by using a widely applied blade element theory (BET) formulation have been compared with those given by application of a boundary element method (BEM) aerodynamic approach for the solution of three-dimensional, unsteady potential flows around lifting bodies. The former is based on quasi-steady sectional aerodynamics with wake dynamic inflow correction, while the latter is able to take into account free-wake and body-interaction effects (including strong wake-body impacts), and has been extensively validated in the past for the analysis of aeroelastic and aeroacoustics problems [4, 5].



(a) Vertical acceleration.



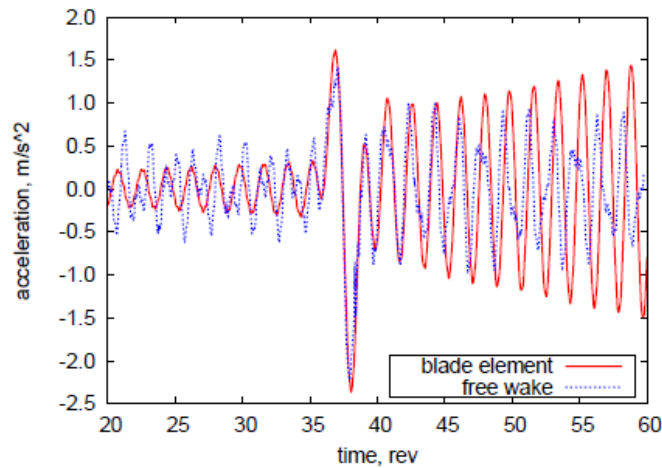
(b) Pilot control,  $\Delta\theta_0$  involuntary pilot.

Figure 1: Pilot-in-the-loop helicopter response,  $G=1.1$ , forward flight.

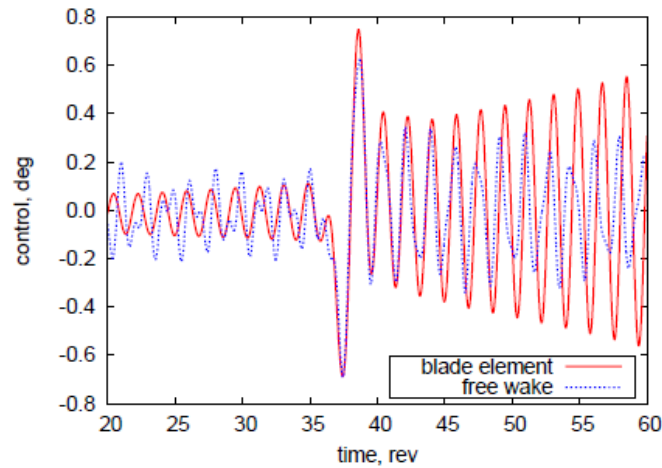
The first application of BEM aerodynamics in RPC analysis has been performed in collaboration with POLIMI by coupling it with the rotor structural dynamics solver MBDyn [6]. Considering the piloted BO105 model in forward flight, the passive pilot model introduced by Mayo [7] and pilot gain (or gearing ratio)  $G = 1.1$ , Fig. 1 shows the response to a collective input 'doublet', consisting of two  $(1-\cos)$  functions of amplitude 0.5 deg of opposite sign, the second one phased half period after the first one. It is given in terms of helicopter CG vertical

acceleration and involuntary collective control imposed by pilot, as evaluated by BET and BEM (free-wake) aerodynamics. For this value of gain, both formulations (BET and free-wake BEM) have a similar behaviour, remaining both stable.

When the same case is analysed with a slightly higher value of gain ( $G=1.2$ ), BET aerodynamics predicts a clearly diverging solution, whereas the free wake one shows a somewhat erratic but stable behaviour (Fig. 2).



(a) Vertical acceleration.



(b) Pilot control,  $\Delta\theta_0$  involuntary pilot.

Figure 2: Pilot-in-the-loop helicopter response,  $G=1.2$ , forward flight.

A clearer view of the stability behaviour may be obtained through the piloted helicopter eigenvalue analysis. For the hovering BO105, Fig. 3 shows the modification of the critical pole (identified by time marching response) as the pilot gain increases: a slightly lower value of critical gain is predicted by free-wake BEM analysis.

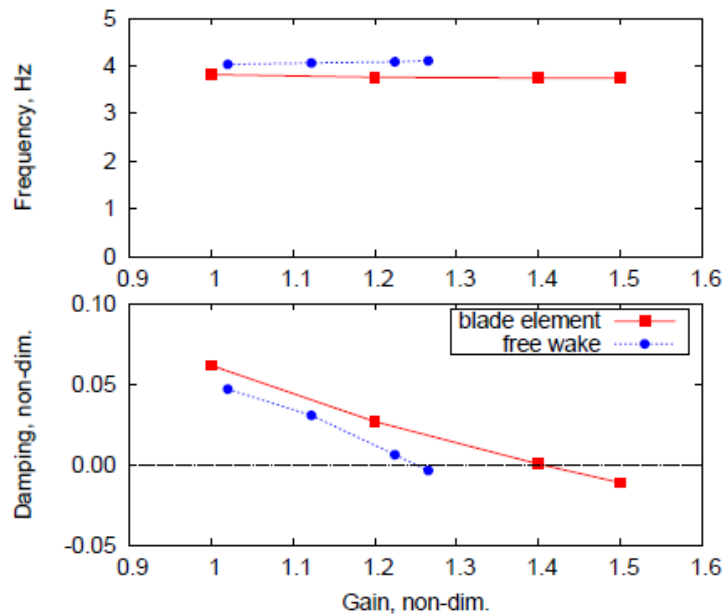


Figure 3: Pilot-in-the-loop helicopter critical eigenvalue, hovering.

However, while time-marching solutions are convenient for taking into account nonlinear effects and having a clearer insight on physical behaviour, they are not so convenient to assess system stability (for instance, in the case of slightly damped coupled dynamics very long investigation time could be required and the interpretation of the responses could be difficult). From this point of view, eigenanalysis is a faster and more reliable approach, although requiring a linear, state-space form description of the system to be examined. In rotorcraft dynamics problems, this can be easily obtained if the aeroservoelastic modelling (particularly the one concerning the rotor) is based on analytical, sectional aerodynamics, while the application of more complex aerodynamic tools (like BEM and CFD solvers, for example) makes the identification of system state-space representation a more difficult task. To overcome this problem, UROMA3 developed a novel methodology for the finite-state modelling of rotor aeroelasticity (see deliverable D3.9). This is based on the identification of the rotor transfer function matrix between hub displacements and hub loads through evaluation of a sequence of time-marching harmonic responses, followed by its rational-matrix approximation. This yields a state-space rotor aeroelastic model given in terms of fuselage degrees of freedom, with the presence of additional states representing the dynamics of rotor blade elasticity and wake vorticity.

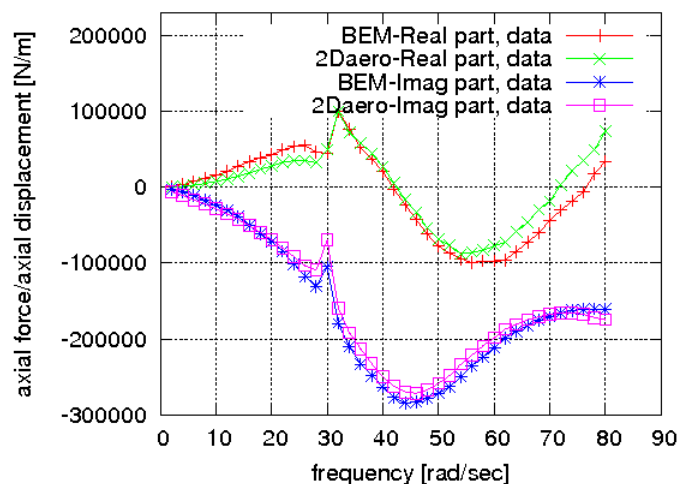


Figure 4: Transfer function between axial force and axial displacement at the hub.

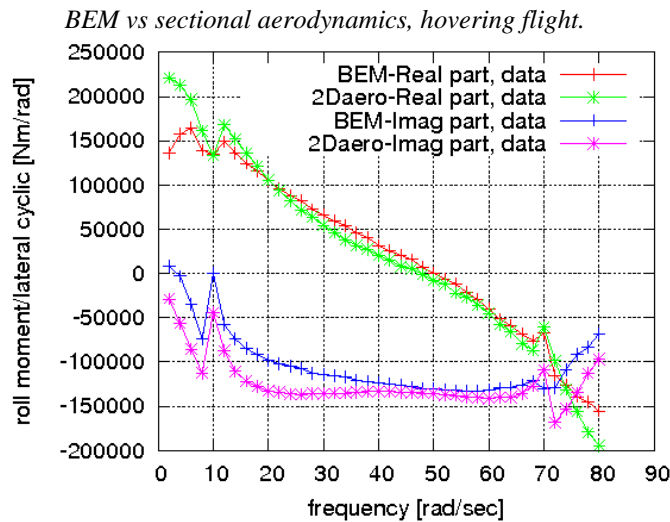


Figure.5: Transfer function between hub roll moment and lateral cyclic pitch.  
BEM vs sectional aerodynamics, hovering flight.

Figures 4 and 5 show the comparison between rotor aeroelastic transfer functions based on quasi-steady sectional aerodynamics and on three-dimensional, unsteady BEM solutions, both derived from a beam-like blade structural model with three sectional degrees of freedom (lag, flap and torsion). Significant discrepancies are present over the whole frequency range, especially for the imaginary part. As already mentioned, in order to have a convenient expression of hub loads in terms of hub motion (which is well suited for helicopter comprehensive modelling and hence RPC investigations) a rational-matrix approximation (RMA) of these transfer functions is performed. Indeed, this yields a state-space representation of rotor aeroelasticity that may be easily coupled with elastic and rigid fuselage dynamics, as well as with blade control actuation from pilot or SCAS. The high level of accuracy achievable with the RMA is shown in Fig. 6, where the rational approximation of the rotor transfer function between hub yaw moment and longitudinal cyclic pitch almost perfectly matches sampled values based on BEM aerodynamics.

Note that, following this approach rotor blade degrees of freedom do not appear explicitly in the model, but rather are represented by RMA poles (the peaks observed in the transfer functions in Figs. 4 and 5 are induced by rotor blade dynamics). This is demonstrated in Fig. 7 where, considering the simple case of rotor aeroelasticity based on quasi-steady, sectional aerodynamics, the rotor eigenvalues directly evaluated from the isolated rotor model described in terms of blade degrees of freedom are compared with the poles identified through the RMA of hub-loads/hub-displacement transfer matrix.

State-space aeroelastic rotor model may be efficiently coupled with fuselage and pilot dynamics models to obtain a comprehensive pilot-in-the-loop helicopter model suitable for RPC/PAO analyses. Considering quasi-steady, sectional rotor aerodynamics, for which the identification of a state-space model may be obtained also by small perturbations of the system degrees of freedom, Fig. 8 compares BO105 eigenvalues as determined from the state-space system identified by perturbations and by the present approach based on transfer function RMA. It demonstrates that most relevant dynamics, including critical poles, is well captured by the proposed general technique applicable to any kind of aeroelastic rotor modelling, both in terms of damping and frequency.

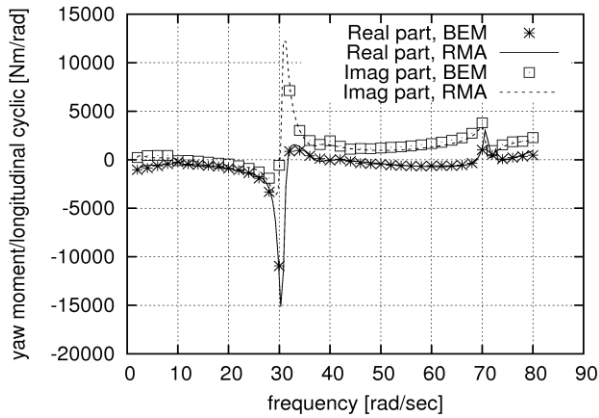


Figure 6: Transfer function between hub yaw moment and longitudinal cyclic pitch. BEM vs RMA, hovering flight.

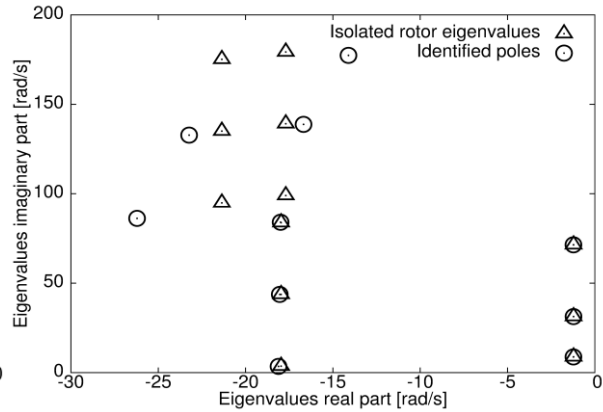


Figure 7: Isolated rotor eigenvalues vs identified poles. Hovering case, quasi-steady aerodynamics.

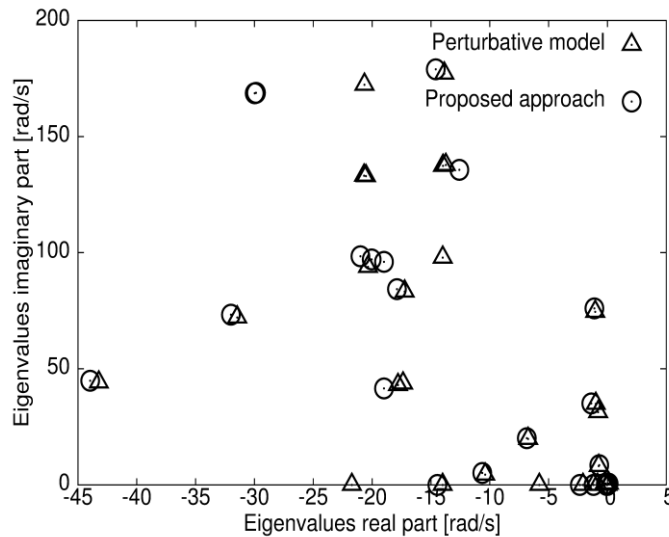


Figure 8: Hovering Bo105 model eigenvalues. Perturbative approach vs RMA approach.

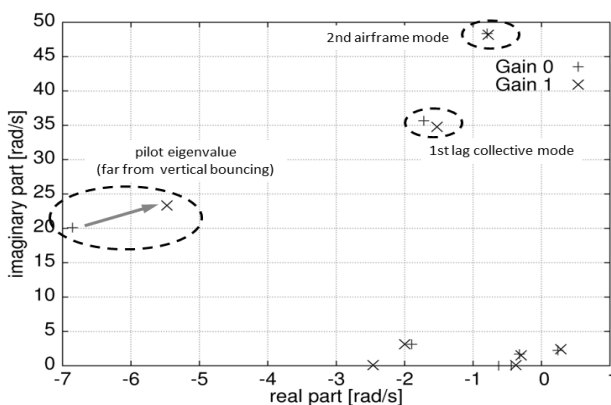


Figure 9: Effect of pilot in the loop on helicopter dynamics, RMA with BEM aerodynamics.

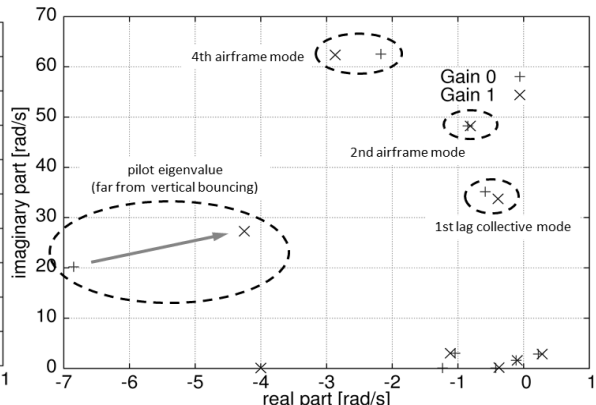


Figure 10: Effect of pilot in the loop on helicopter dynamics, RMA with sectional, quasi-steady aerodynamics.

Finally, Figs. 9 and 10 show the impact of pilot-in-the-loop inclusion ( $G=1$ ) when rotor aeroelasticity is based on BEM aerodynamics and on sectional, quasi-steady aerodynamics,

respectively. Most of the eigenvalues predicted by BEM and sectional, quasi-steady aerodynamics are quite similar, but appreciable differences appear between the poles dominated by pilot biodynamics (and most involved in the vertical bouncing phenomenon) and the eigenvalues related to the first lag collective elastic mode. In particular, the first lag collective elastic mode predicted by application of the sectional aerodynamics formulation is significantly less damped than that obtained from BEM aerodynamics. This occurs regardless the presence of the pilot in the loop which, anyway, tends to decrease the stability margin of this mode. The very low frequency modes appearing in Figs. 9 and 10 are related to the rigid body motion (namely, phugoid, roll, spiral, heave subsidence, pitch subsidence); it is worth noting that, the phugoid motion is slightly unsteady because, for the sake of simplicity, no flight control system for helicopter stabilization has been considered in the analysis.

After this short review, one can conclude that, although simple, quasi-steady sectional rotor aerodynamic modelling yields helicopter dynamics and RPC/PAO simulations that are generally close to those obtained from the application of three-dimensional, unsteady BEM solvers, some significant differences may appear in predicting critical behaviours and, thus, for next generation helicopters design focused on RPC prevention the application of accurate rotor aerodynamic modelling is encouraged. In view of this, a methodology for the efficient numerical stability analysis of piloted helicopter configurations simulated by an arbitrarily complex aerodynamic model has been proposed and validated.

### Linear vs. Non-linear Modelling

Next, the attention of UROMA3 has been focussed on the assessment of the effects of nonlinearities in aeroservoelastic modelling for RPC/PAO analysis.

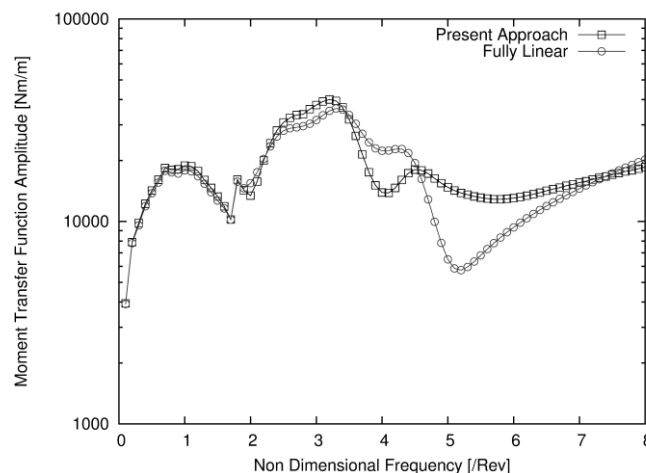


*Figure 11: Effect of nonlinearities on pitching moment vs longitudinal displacement transfer function.*

Two different issues concerning modelling nonlinearities have been taken into account: effect of reference trim state on linearized rotor model and effect of nonlinear terms on response to initial perturbations (for stability analysis).

Figure 11 presents the comparison between the transfer function relating hub pitching moment to hub longitudinal displacement evaluated about a null (blade-undeformed) trim state (“Fully Linear”) and that evaluated about the correct blade-deformed trim state (“Present Approach”). Although reference trim state is sometimes neglected in simple rotor modelling, this figure shows that it may play a very significant role on rotor aeroelastic response: significant discrepancies are present on most of the frequency range examined and the similar results have been obtained for the rest of the transfer functions relating hub

loads to hub motion and blade controls. This result suggests that the accurate identification of linearized rotor modelling (for instance, for aeroservoelastic purposes) requires the accurate identification of the reference rotor trim state.

Advantages and disadvantages of the time-marching solution of aeroelastic systems have already been mentioned. However, it is important to point out that this is the simplest way to introduce a wide class of complex contributions like, strong periodic-coefficient terms, saturation of controls, malfunctioning, strong aerodynamic interactions, non-small perturbations, that can heavily affect RPCs. Focussing the attention to the problem of stability analysis, Figs. 12-15 show the influence of nonlinear terms in the pilot-in-the-loop response to a perturbation to the collective stick rotation (in these pictures, NLTM indicates nonlinear time-marching simulation, whereas LTM indicates linear time-marching solution).

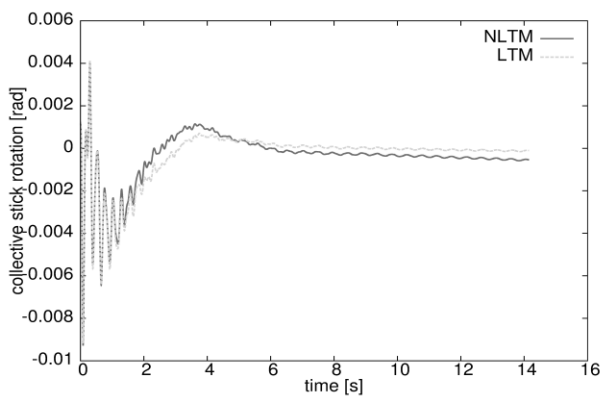


Figure 12: Pilot-in-the-loop response to a small initial perturbation,  $G=0.6$ .

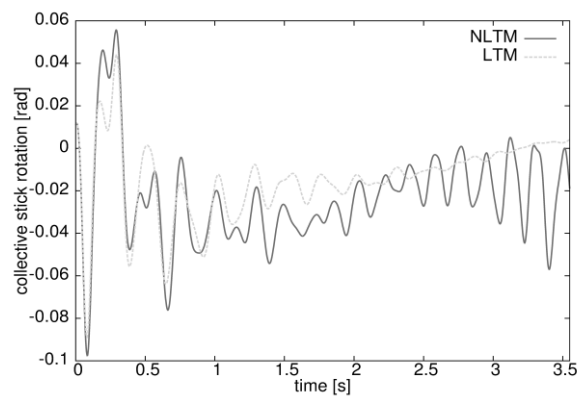


Figure 13: Pilot-in-the-loop response to an initial perturbation,  $G=0.6$ .

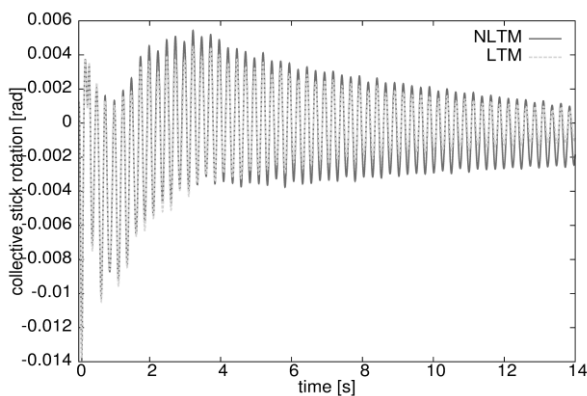


Figure 14: Pilot-in-the-loop response to a small initial perturbation,  $G=0.9$ .

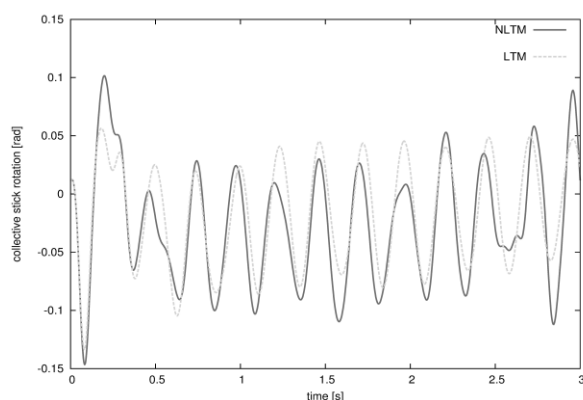


Figure 15: Pilot-in-the-loop response to an initial perturbation,  $G=0.9$ .

The responses presented in Figs. 12 and 13 have been evaluated for  $G=0.6$  (corresponding to a stable linearized configuration), for two different values of initial perturbation. For the smaller value of the initial perturbation (Fig. 12) linear and nonlinear models predict similar (stable) behaviour while, increasing by a factor ten the initial perturbation, nonlinear model becomes unstable, evidently due to the growth of nonlinear terms effects. Figures 14 and 15 present the result of a similar analysis concerning the case with a higher value of gain,  $G=0.9$  (corresponding to a linearized configuration close to the margin of stability). Also in this case, for small initial perturbations linear and nonlinear responses are quite similar, with the

second one slightly less damped. For larger initial perturbations, nonlinear model becomes rapidly unstable, despite this instability doesn't seem to involve heavily pilot dynamics. These results suggest that, although the eigenvalue analysis remains the more practical way to assess the overall stability behaviour (especially for design purposes, where synthetic description of system behaviour is required), nonlinear time-marching analysis should be performed for verification and detailed analyses aimed at RPC/PAO prevention.

### Pilot Modelling

Further investigations on modelling requirements have concerned the influence of passive pilot modelling on aeroservoelastic RPC/PAO predictions. Pilot model is obviously a critical component of PAO analyses. Both data available from literature and the results from the experimental campaign carried out in ARISTOTEL present a large number of identified models. Indeed, in addition to commands setting and cabin architecture the pilot operates in, they depend on several parameters like, for instance, pilot body characteristics, workload, direction of perturbations soliciting the pilot biodynamical feedthrough. Thus, it is interesting to assess the impact on the numerical simulations of PAO predictions of the different passive pilot models that could be introduced.

Figure 16 shows the comparison between piloted BO105 eigenvalues evaluated by pilot models proposed in Refs. [7] and [8], all related to a similar pilot weight. The pilot transfer functions models identified in Ref. [8] take into consideration the influence of pilot task on pilot passive response to a motion perturbation (specifically, the classes of tasks examined are force, precision and relaxed tasks). It is possible to observe that, while force task pilot response tends to yield a more stable system, the overall behaviour is quite similar during the transition from pre-critical to post-critical configurations (i.e., from pilot gain  $G=0.9$  to pilot gain  $G=1.35$ ).

This behaviour is confirmed by the results presented in Figs. 17 and 18, which concern the stability analysis of BO105 and IAR330 Puma, respectively, as given by a detailed gain sweep for the different-task pilot models proposed in Ref. [8]. Although different coupling with airframe modes may be observed, the vertical bouncing insurgency is very similar for all pilot models, and arises when pilot gain/gearing ratio is increased slightly above 1.

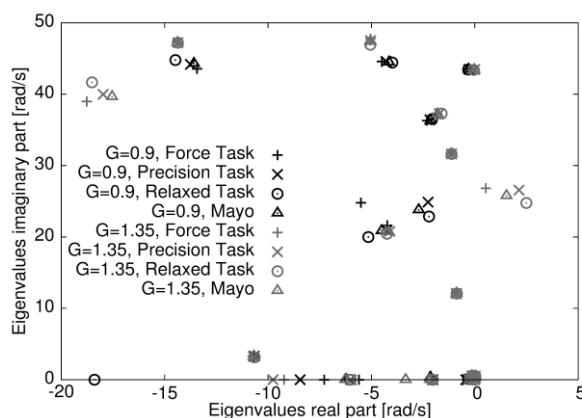


Figure 16: Effect of task-dependent pilot models on BO105 stability.

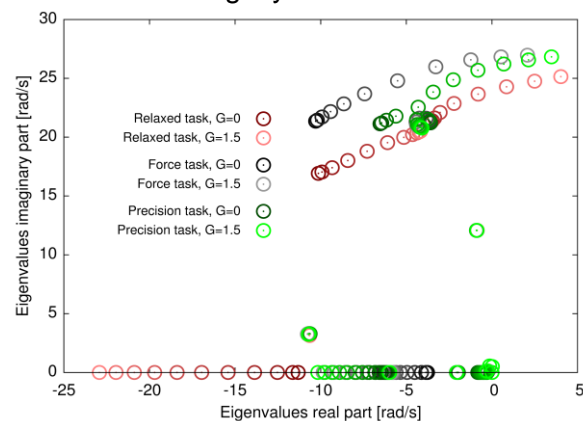


Figure 17: Effect of pilot gain/gearing ratio on BO105 stability.

Then, Fig. 19 presents BO105 eigenvalues as predicted by considering biodynamical pilot feedthrough from transfer functions identified during the ARISTOTEL experimental campaign of WP4. It is important to note that these pilot models, unlike those from the literature, are not averaged and therefore a single results may not be univocally representative of one

individual pilot behaviour. However, vertical bouncing insurgency appears in substantially similar conditions. Increasing pilot gain above  $G=1$  yields instability (except for one pilot, who induces an unstable response for a relatively lower value of gain). Critical eigenvalue frequency is higher than that in the previous analyses (between 30 and 35 rad/s), but still within the range of lower airframe modes.

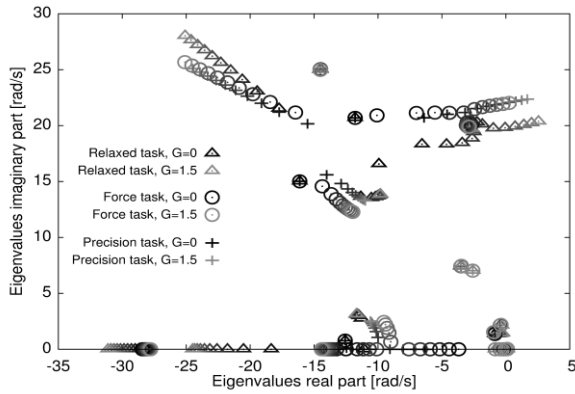


Figure 18: Effect of pilot gain/gearing ratio on IAR330 Puma stability.

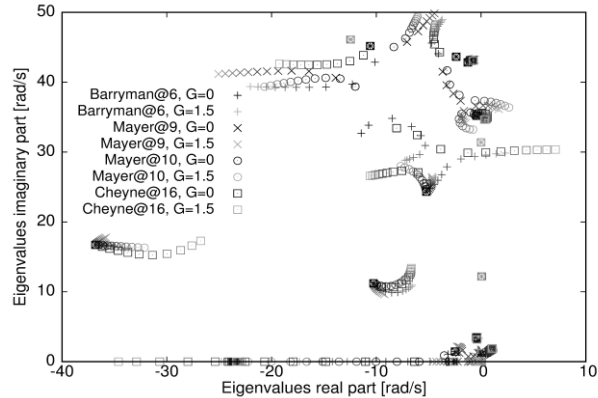


Figure 19: BO105 stability analysis with pilot models identified in WP4.

It is interesting to remark that different pilots (or even, different transfer functions identified for the same individual) may present significantly different poles, revealing that a statistical investigation is required for a more robust stability analysis.

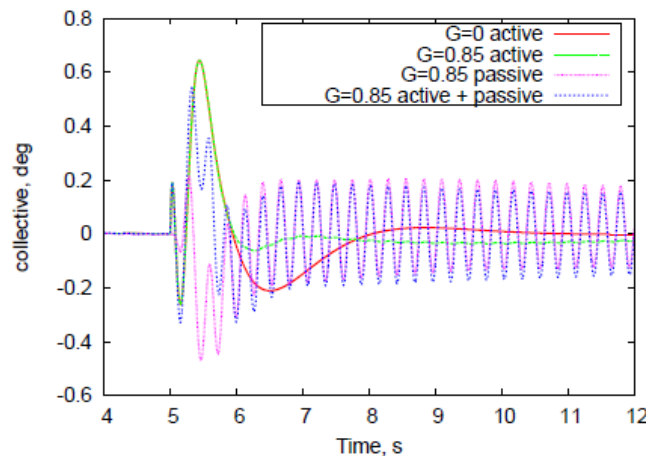


Figure 20: Effect of active pilot on PAO.

Finally, the effect of the inclusion of an active pilot model on RPC/PAO prediction has been assessed in cooperation with POLIMI. Figure 20 presents the response to a collective pitch perturbation, as resulting from considering pilot-in-the-loop effects from an active model, a passive model, and a combination of the two. This investigation confirms that simple active pilot modelling doesn't modify the mid-frequency (2-10 Hz) behaviour and therefore doesn't affect PAOs. The influence of active pilot modelling is limited to low frequency input response, while non-forced response remains almost unaffected in terms of damping and frequency. This conviction is strengthened by the position of passive pilot poles which in all cases investigated in WP4 has been found to be placed at a frequency close to 4 Hz. It is important to note that particular flight control systems may alter this situation and then, if an intensive actuation of AFCS occurs, the introduction of active pilot even for PAO identification purposes is suggested.

## 2.2. Analysis of RPC/PAO sensitivity to structural parameters

The second part of UROMA3 activity concerning the identification of design guidelines for RPC analysis and prevention has been focussed on the analysis of RPC/PAO sensitivity to some of the structural parameters that may be critical in terms of instability occurrence. This activity has been partly carried out in cooperation with POLIMI.

Although, in general, the helicopter designer has a narrow level of freedom in changing structural parameters, the preliminary design phase is that most suited for this kind of action. Indeed, at a later stage the designer may make minor adjustments only, usually limited to retrofit modifications. The interest in the following investigation is twofold: it may give useful guidance in new helicopter design to prevent adverse RPC/PAO events, but also may suggest alleviation techniques of eventual instabilities arising in existing helicopter configurations.

### Airframe structural parameters

First, the airframe stiffness is examined. The investigation consists of modifying airframe modal frequencies slightly above and below their nominal values, considering an unstable configuration with pilot in the loop. Since airframe deformation plays an important role in transmitting vibrations from hub to pilot seat, it is expected that a change in airframe stiffness would affect PAO as well. For the BO105 this is confirmed in Fig. 21, where it is shown that the change of airframe frequencies significantly affects critical and several non-critical modes. While some modes tend to become more stable (the vertical bouncing is one among them) when stiffness is increased, other modes move toward instability (the most critical being the 2nd lag).

Unlike what observed for the BO105, Fig. 22 demonstrates that for the helicopter IAR330 Puma the influence of airframe stiffness modification on vertical bouncing is negligible: this occurs because of the weaker participation of airframe deformation to PAO instability.

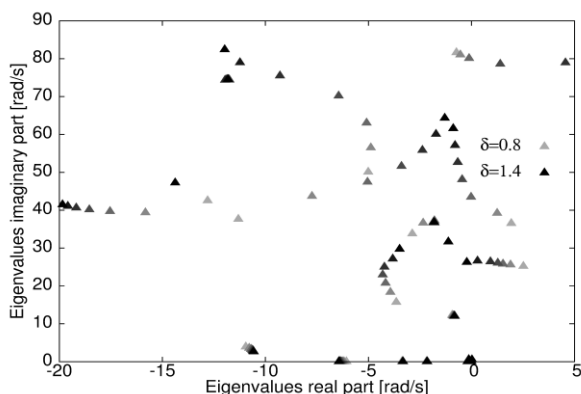


Figure 21: Effect of airframe stiffness, BO105.

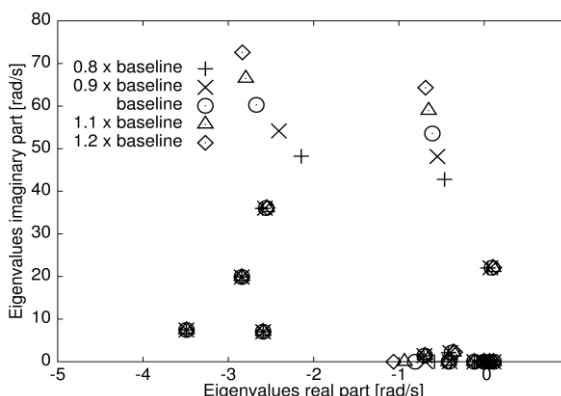


Figure 22: Effect of airframe stiffness, IAR330 Puma.

Then, a similar investigation has been performed considering modifications of the airframe modal damping, as representative of the introduction of some dampers inside the structure. Figures 23 and 24 show that for both helicopters examined, the effect on vertical bouncing is very small, suggesting that damping augmentation is not an effective way to avoid adverse PAO.

### Rotor structural parameters

Next, the attention has been focussed on rotor structural properties. Rotor design is subject to a large number of constraints and then, even in the preliminary design, the modification of rotor properties is not a simple task. However, since main rotor plays a fundamental role in

PAO events, it is of interest to explore the possibility of alleviating their instability by rotor structural properties modification (this is particularly simple for rotors with lag/flap dampers and springs).

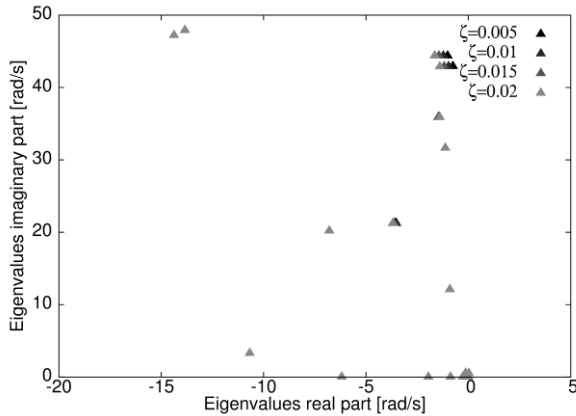


Figure 23: Effect of airframe damping, BO105.

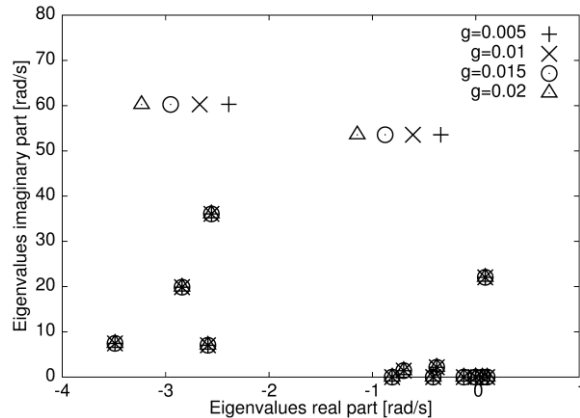


Figure 24: Effect of airframe damping, IAR330 Puma.

Figures 25 and 26 present the effect of changing IAR330 Puma flap hinge stiffness and damping, respectively. Since no flap damper is present on Puma, the values have been referred to the lag damper one. As it is clearly shown, changing flap hinge stiffness doesn't affect vertical bouncing, while the introduction of a flap damper is beneficial.

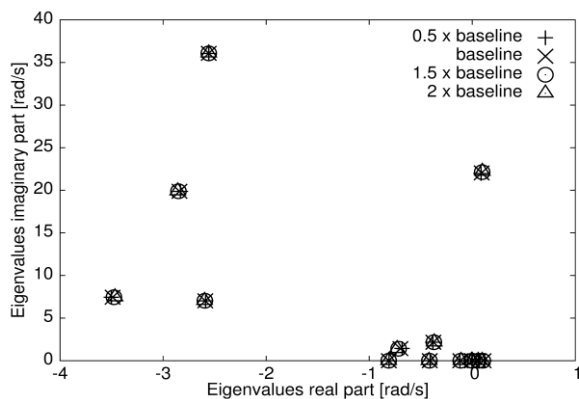


Figure 25: Effect of flap hinge stiffness on RPC, IAR330 Puma.

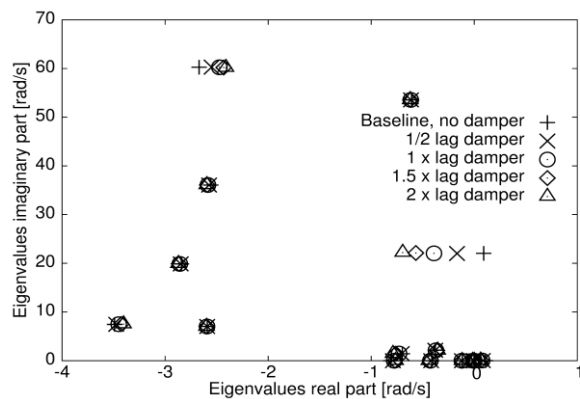


Figure 26: Effect of flap hinge damping on RPC, IAR330 Puma.

Further, the BO105 rotor properties have been investigated. In this case, no flap or lag hinges are present, and thus it consists of variation of distributed flap and lag structural parameters. Figure 27 shows that, although relatively high (with respect to baseline) modifications of blade damping are considered, these do not have relevant effects on the critical vertical bouncing mode.

Then the effect of the rotor torsional compliance has been assessed. Specifically, a rigid torsion blade has been introduced by increasing the torsional stiffness, so as to separate the contribution of blade torsion and of control system to blade pitch. It is worth noticing that this induced a reduction of about 1.2 deg of the trim collective pitch (a clear indication of the important role played by the blade torsional compliance).

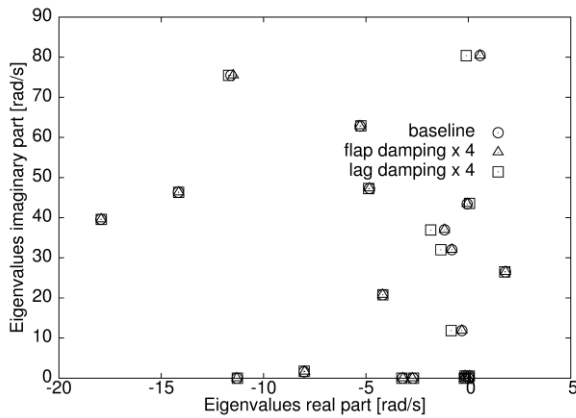


Figure 27: Effect of blade structural damping on RPC, BO105.

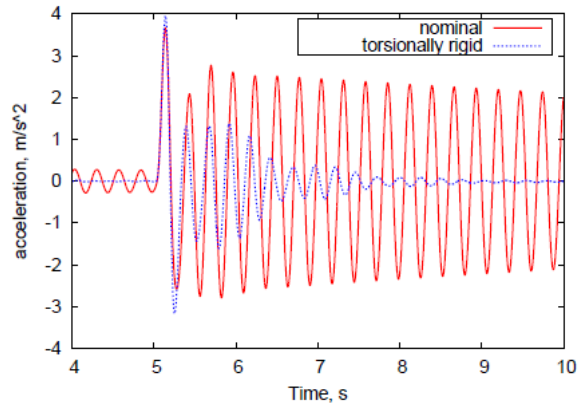


Figure 28: Effect of rotor compliance on RPC, BO105.

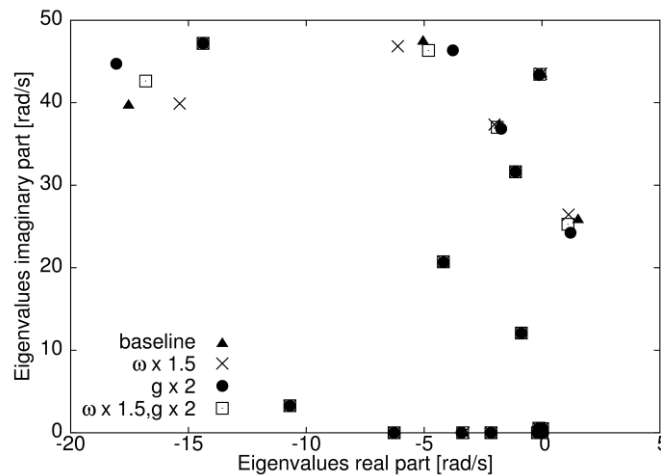


Figure 29: Effect of control system stiffness and damping on RPC.

Although the mode shapes clearly indicate that the collective bounce phenomenon is dominated by rigid blade pitch, Fig. 28 shows that blade elastic torsion deformation significantly affects PAO stability: indeed, in the torsion-rigid blade case the instability appears when the value of the pilot gain (or gearing ratio) is 25% higher than that identified as critical for nominal stiffness blade. It is worth observing that during collective bounce, blade torsion is essentially static, since the frequency of the first blade torsion mode is about 28 Hz, i.e., much higher than that of the unstable mode.

The sensitivity of the stability limit to the properties of the control system has been investigated as well. Figure 29 shows that, for a given gearing ratio, the compliance of the control system and the bandwidth of the swash-plate actuators minimally impact the stability of the coupled pilot-vehicle mode. When the control system compliance is neglected (not shown), thus resulting in higher torsion mode frequency and smaller overall static torsion of the blade, the pilot-vehicle model requires a higher gain to reach the verge of stability. This is consistent with the previous observation about the effects of torsional stiffness of the blade.

Drawing conclusions, it can be stated that blade and hub properties may alter significantly adverse RPC/PAO occurrence: thus, the introduction of suited root dampers could be an effective way to alleviate this kind of instabilities. On the other hand, acting on servoelectricity parameters (for instance by changing damper and spring of control chain) to reduce instabilities has been proved to be non-effective.

### 2.3. Concluding remarks

The results presented and discussed above, may be summarized in the following design guidelines for RPC/PAO analysis and prevention:

#### Pilot-Vehicle System modelling

- Although widely-applied quasi-steady sectional rotor aerodynamic modelling yields helicopter dynamics and RPC/PAO simulations that are generally close to those obtained by more sophisticated aerodynamic solvers, some significant differences may appear in predicting critical behaviours: thus, for next generation helicopters design focused on RPC prevention, the application of accurate, three-dimensional, unsteady, interactional rotor aerodynamic modelling is suggested;
- Pilot workload may play a relevant role in pilot passive response to perturbation, and thus it has to be taken into account when modelling pilot behaviour for RPC/PAO stability analyses;
- The inclusion of active pilot modelling for PAO simulation purposes may be neglected, unless intensive actuation of AFCS occurs.

#### A/RPC prediction

- System eigenvalue analysis has been proven to be an efficient way to assess the overall RPC/PAO stability behavior, especially for design purposes, even when complex rotor aerodynamic models are applied (with the support of a methodology for the identification of aeroelastic/aerodynamic rotor transfer functions);
- Nonlinear time-marching analysis should be introduced, anyway, for design verification purposes, in that capable to examine detailed effects that may play a non-marginal role in the occurrence of adverse RPC/PAO events.

#### Conceptual/Preliminary design

- Airframe stiffness is a parameter that may significantly affect the RPC/PAO stability of helicopters: more rigid airframe tends to stabilize vertical bouncing (however, the opposite effect might be observed on some rotor modes);
- Airframe damping does not significantly affect RPC/PAO stability;
- Rotor stiffness barely affects vertical bouncing, while the introduction of a flap damper may be beneficial;
- Blade torsional compliance significantly affects RPC/PAO occurrence: rotors with rigid torsion blades tend to alleviate RPC/PAO instability;
- The modification of servoelastic system parameters scarcely affects RPC/PAO stability behavior.

### References

1. ARISTOTEL Deliverable No. D3.4, Aircraft and rotorcraft modelling for aero-servo-elastic A/RPC, March 2012.
2. ARISTOTEL Deliverable No. D3.9, Prediction of aero-servo-elastic instabilities with and without pilot in the loop, April 2013.

3. ARISTOTEL Deliverable No. D4.11, Validation of models and criteria for aeroservoelastic A/RPC predictions, July 2013.
4. Bernardini G., Serafini J., Gennaretti M., Ianniello S. (2007). “*Assessment of Computational Models for the Effect of Aeroelasticity on BVI Noise Prediction*”. INTERNATIONAL JOURNAL OF AEROACOUSTICS, vol. 6 (3), p. 199-222
5. Bernardini G., Serafini J., Molica Colella M., Gennaretti M. (2013). “*Analysis of a structural-aerodynamic fully-coupled formulation for aeroelastic response of rotorcraft*”. AEROSPACE SCIENCE AND TECHNOLOGY, in press.
6. Gennaretti M., Serafini J., Masarati P., Quaranta G. (2013). “*Effects of Biodynamic Feedthrough in Rotorcraft/Pilot Coupling: Collective Bounce Case*”. JOURNAL OF GUIDANCE CONTROL AND DYNAMICS, in press.
7. Mayo, J.R. The involuntary participation of a human pilot in a helicopter collective control loop. In 15th European Rotorcraft Forum, pages 81.1–12, Amsterdam, The Netherlands, 12–15 September 1989.
8. Venrooij J., Pavel M. D., Mulder M., van der Helm F. C. T., Bulthoff H.H. “*A practical biodynamic feedthrough model for helicopters*”. In proceedings of 38th European Rotorcraft Forum, Amsterdam, the Netherlands, Sep. 2012.

## List of Abbreviations

AFCS	Automatic Flight Control System;
BEM	Boundary Element Method;
BET	Blade Element Theory;
CFD	Computational Fluid Dynamics;
LTM	Linear Time Marching;
NLTM	Non-Linear Time Marching;
PAO	Pilot-Assisted Oscillations;
RMA	Rational Matrix Approximation;
RPC	Rotorcraft-Pilot Coupling;
SCAS	Stability and Control Augmentation System.

## Appendix E: A general methodology for boundary-triggered PIO investigations (UoL)

It is common for a rotorcraft to perform practical tasks with constraints, such as the Nap-of-the-Earth manoeuvre, approach or land task with constraints (e.g. oil rig), and flying through a valley. These constraints can degrade the pilot performance, or more severe, result in Boundary-Triggered Pilot-Induced-Oscillation (PIO) or even loss of an aircraft. To minimize the probability of task failure under these situations is a major design challenges. This report presents a general methodology for assess the pilot-aircraft performance and susceptibility of the PIOs for a Point-Tracking (PT) dominant task subject to such boundary constraints.

The approach present here is evolved from Gray's boundary-tracking (BT) model [1], as illustrated in Fig. 1.

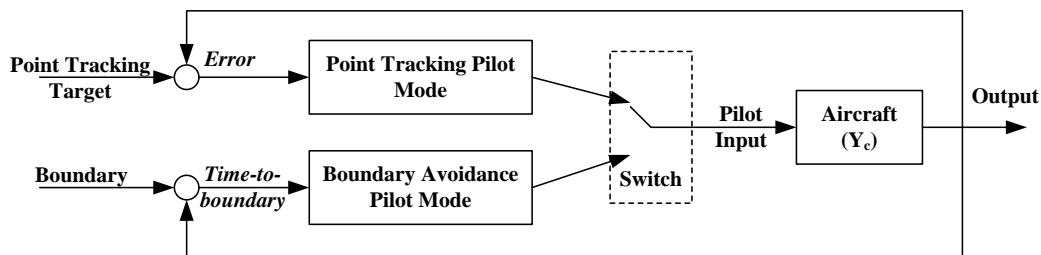


Fig. 1 Gray's boundary-avoidance-tracking model (based on [1])

This BT model has been introduced in D2.3 and thereby ignore here. There are, however, aspects of this BT pilot modelling approach which require further attention. The first is the assumption of instantaneous switching between PT and BT in Gray's pilot model where the PT and BT elements of a pilot's control strategy work almost independently. In Ref. [2], Gray presents a spectrum of BT situations. This assumption would be correct for the boundary escape (BE)-dominant tasks on this spectrum. However, it may be less valid to describe those BT tasks that lie elsewhere on this spectrum i.e. between the traditional pure PT tasks (no or minimal boundary avoidance (BA) control) and Gray's BE tasks (no PT control). In the middle ground, these might be considered to be PT-dominant situations, subject to a BA influence as a secondary, managerial task [3;4]. For such tasks, the boundaries may be given a lower priority than the PT task. For example, ADS-33E Mission Task Elements [5], by having boundaries associated with desired and adequate handling qualities performance criteria (which may not be associated with a dangerous boundary), are examples of potential PT-dominant tracking tasks with a BA element. A skilled and experienced pilot has normally been well trained to deal with situations involving simultaneous primary PT control and secondary managerial tasks. The pilot is able to allocate attention to multiple tasks in which information is simultaneously gathered from a number of perceptual fields. Therefore, as far as the active BT pilot control processes are concerned, the PT (primary task) and BA (secondary task) may run concurrently, at least for a certain period after the initiation of the BA task i.e. the PT and BA perceptual inputs impinge and are acted upon the pilot at the same time. For the purposes of this report, a PIO occurs in this kind of situation. The second area for consideration is the type of PT pilot model used in previous BAT studies. The PT pilot models implemented are usually designed as a simple Proportional-Integral-Derivative (PID) controller [6;7]. These do not take into account the specific and potentially rich cues that an experienced and well-trained pilot can gather simultaneously from several perceptual

fields (e.g., vestibular and proprioceptive cues) [8]. From a practical perspective, the model input parameters and the subsequent interpretation of the results achieved can be difficult to validate because no physical human operator attributes or behaviours can be expressed easily in such systems. The final aspect for consideration is that, due to the BT pilot model using the nonlinear variable  $\tau$ , previous work has not quantitatively investigated the effects of the BT loop on the main PT loop. Therefore, the actual mechanism that drives the whole system into instability during a BT manoeuvre is still not well understood.

The methodology proposed to address the above issues are summarised as follow.

**A. Hess’s Multi-Loop Pilot Model designed for the PT task**

This report, as part of the European Commission 7th Framework Programme project - ARISTOTEL, addresses each of these issues [9]. Within the project, all experimental research has been conducted using simulation, either ‘real-time’ pilot-in-the-loop full-motion flight simulation or ‘offline’ analysis. The need to model simulator parameters (e.g. motion cueing on/off) to try to estimate their effect on the results obtained and hence the ability to make predictions are of key interest to this project. To that end, Hess’s multi-loop pursuit pilot model has been adopted as it has been shown to be “representative” of a real pilot for use in simulations of realistic flight tasks and takes account of a number of practical factors such as the effects of task interference, motion and visual cues, and the level of pilot control aggressiveness and skill. As a consequence, Hess’s pilot model has been extended to design a PT pilot model [10-13] to study the BT (in this case, the BA) phenomenon.

The procedure proposed by Hess for modelling pilot pursuit control behaviour has shown significant value for research in that the pilot model created is not only able to describe pursuit pilot behaviour, but can account for visual, proprioceptive, and vestibular cues in an approximate fashion [11;12;14;15]. Therefore, this approach is adopted in this report to develop the PT pilot model in Fig. 1 and is summarized here.

As a starting point, the structure of the multi-loop pilot model is illustrated in Fig. 2.

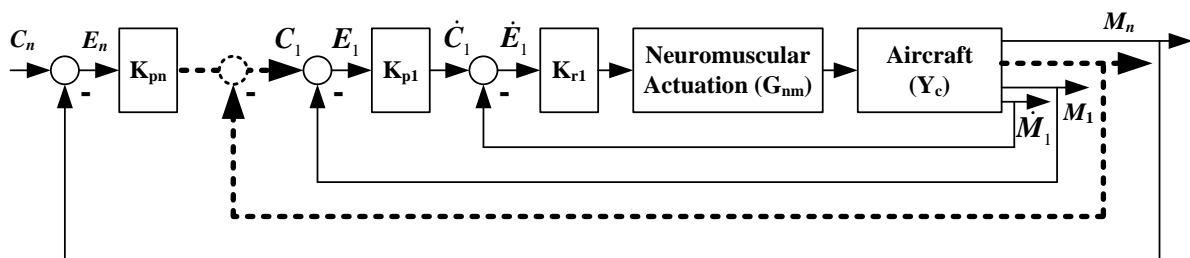


Fig. 2 Hess’ loop-by-loop pursuit pilot model [11]

Fig. 2 describes a pilot model consisting of  $n$ -pair inner (output rate feedback,  $\dot{M}_i$ ) and outer (output position feedback,  $M_i$ ) loops. These position-based loops ( $C_i$  and  $M_i$ ) and their first-order derivatives ( $\dot{C}_i$  and  $\dot{M}_i$ ) are closed because they are usually available to the pilot during a manoeuvring task. The outer loop of each pair ( $C_i$  and  $\dot{C}_i$ ) deals with the feedback position error ( $E_i$ ) between a given tracking signal ( $C_i$ ) and feedback position ( $M_i$ ). For example, the first inner-most loop deals with the tracking position error ( $E_1$ ), through the gain variable  $K_{p1}$ , between the first output position feedback ( $M_1$ ) and the reference signal ( $C_1$ ), generated from the next-outer loop. Similarly, the inner loop of each pair addresses the rate feedback information. The inner loop represents the extra control effort that the pilot may apply due to possible additional cognitive information [5]. Besides these loops, the neuromuscular system ( $G_{nm}$ ) of the pilot is modelled as a second-order transfer function by neglecting very-high frequency input information [11;12]:

$$G_{nm} = \frac{\omega_{nm}^2}{s^2 + 2\zeta_{nm}\omega_{nm}s + \omega_{nm}^2} \quad (1)$$

in which  $\zeta_{nm}$  is the neuromuscular damping ratio and  $\omega_{nm}$  its natural frequency. Moreover, the rate and position information mentioned above is described in a relative manner. They can refer to various sources that a pilot is able to sense. For example, the rate feedback may be based upon proprioceptive and vestibular cues. When these cues are required for the pilot model, ad-hoc techniques are used to model the sensory systems. The details relating to the work reported in this report will be provided as required hereafter. When visual cues are being used, the following visual model [15] is adopted on each visual channel to reflect the quality of visual information sensed by the pilot:

$$E_i^i = E_i \left( 1 + n_w \frac{1}{0.5s + 1} \right) \quad (2)$$

in which  $n_w$  is a zero-mean, normally distributed random variable with variance  $\sigma_{vis}$ .  $E_i$  is the position tracking error of the  $i^{th}$ -pair feedback loop. This equation also applies on the rate tracking error ( $\dot{E}_i$ ), if sensed by the pilot. This signal is saturated with limits  $2\sigma_{vis}$ . The better the useable cue environment, the lower is the value of  $\sigma_{vis}$ .

The successful implementation of the multi-loop pilot model depends upon a sensible selection of the pilot gains in Fig. 2. Moreover, the pilot model, constructed with those gains, needs to satisfy at least 2 requirements. First, the final pilot model should be able to perform the required tracking task. Second, the pilot model should match the real behaviour of a pilot as closely as possible, unlike the PID controllers that represents the PT pilot model in the work performed to date. To meet these requirements, the following rules are used to select pilot gains (starting from the inner-most loop). The gain  $K_{r1}$  is chosen such that all of the damping ratios of the transfer function  $\dot{M}_1/\dot{C}_1$  are larger than 0.15. The gain  $K_{p1}$  is selected so that the open-loop crossover frequency of the system,  $M_1/E_1$ , is equal to 2 rad/s. This is a representative value of high-gain pilot control activity derived from flight test data [11]. When the gains for the first pair of loops have been determined, the same procedure is applied to the next 2<sup>nd</sup>-pair outer loop, only its open-loop crossover frequency is reduced by a factor of 3 (0.667 rad/s for the 2<sup>nd</sup>-pair loop). This frequency separation is adopted to ensure that the outer loop exhibits a desirable integral-like behaviour around the outer-loop crossover frequency [8]. The same procedure is repeated until all of the necessary pilot gains are found.

If a multi-axis control situation is being considered, the gains of all of the rate-control loops in Fig. 2 are reduced by a factor,  $f$ , modelling the task interference between the different control axes. The value  $f$  is given as follows [12;13],

$$f = 1 + 10(\sigma_{vis} + \sigma_{task}) \quad (3)$$

in which  $\sigma_{task} = 0.01n$  if the number of control channels ( $n$ ) is larger than one, else it will be zero. In addition, the aggressiveness of the pilot control activity can be modelled by multiplying the gains of all position-control loops with an aggression degree factor  $k_{agress}$ .

Therefore, based on Hess' multi-loop PT pilot model in Fig. 2, the closed-loop BAT model in Fig. 1 can be modified to Fig. 3.

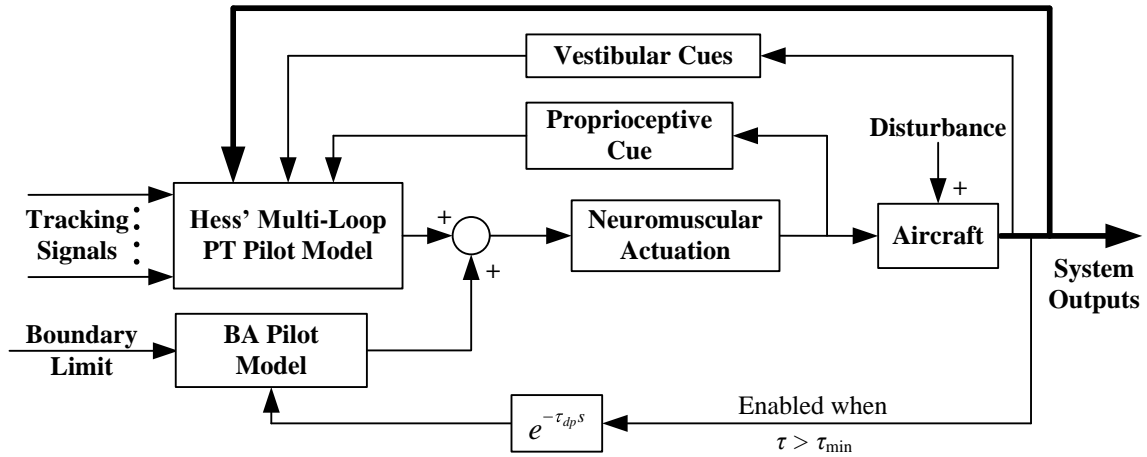


**Fig. 3 The BAT pilot model for a closed-loop tracking system**

The vestibular and proprioceptive cues in Fig. 3 are separated from Hess’s multi-loop pilot model to better illustrate the information perceived by the pilot. Moreover, a perception time delay  $\tau_{dp}$  has been introduced in the BA loop to account for the delays associated with the pilot’s perceptual system response times.

**B. Modelling the Boundary-Avoidance Tracking Process**

A specific procedure is proposed in this report to handle the issue of the nonlinearity of the BA model. Thus, these advanced modelling features provide a feasible way to identify the essence of the BA phenomenon and are a major contribution of this report. This procedure is summarized in the following

The BA pilot activity in Gray’s model is modelled as a pure BA gain ( $K$ ) (Refer to D2.3). While the variation of this gain is linear, the essence of this operation is nonlinear, due to the dependence on  $\tau$  in Eq. (4)

$$\tau_b = \frac{x_b}{\dot{x}_b} \tag{4}$$

which is based on the distance to boundary ( $x_b$ ) at the current rate of approach ( $\dot{x}_b$ ), defined as follows: This brings with it a difficulty in analysing the stability of the closed-loop systems of Fig. 1 and Fig. 3. It is proposed that this nonlinearity issue be addressed by linearizing the information transfer characteristics of the BA attributes of the human controller. The linearization is performed as follows.

As assumed in Gray’s BAT pilot model, the BA process is triggered when  $\tau > \tau_{min}$ . Therefore, Eq. (4) is linearized first using a Taylor series expansion at the initial state ( $x_{b0}, \dot{x}_{b0}$ ) corresponding to the triggering moment ( $\tau = \tau_{min}$ ) as shown in the following:

$$\Delta\tau(x_b, \dot{x}_b) \approx \tau(x_b, \dot{x}_b) - \tau(x_{b0}, \dot{x}_{b0}) = \dot{x}_{b0}^{-1}\Delta x_b - x_{b0}\dot{x}_{b0}^{-2}\Delta\dot{x}_b \tag{5}$$

Finally, the Laplace transform of Eq. (5) can be described as follows,

$$\Gamma(s) = (\dot{x}_{b0}^{-1} - x_{b0}\dot{x}_{b0}^{-2}s)X(s) \tag{6}$$

in which  $\Gamma(s)$  and  $X(s)$  represent the Laplace transform of  $\Delta\tau$  and  $\Delta x_b$ , respectively. Three points relating to the above procedure are worthy of note. First, at the moment that the observer becomes aware of the existence of the impending boundary, the initial gap ( $x_{b0}$ )

measuring the current distance to the boundary and the optical variable  $\tau$ , by definition, is negative. However, the increments of both  $\Delta\tau$  and  $\Delta x_b$  as well as the boundary-approach speed ( $\dot{x}_{b0}$ ) are positive. Second, the formulae given in Eqs. (5) and (6) that rely on  $\Delta\tau$  are consistent with the finding of the recent study regarding the information used in detecting an upcoming collision (the boundary for this study) by Bootsma and Craig [16]. They found that the information carried in  $\Delta\tau$  is the most effective predictor for collision avoidance. Finally, the perception of the optical tau information, as modelled in Eq. (6), is equivalent to the introduction of a lead equalization by the pilot. This lead term is entirely consistent with the prospective nature of the hypothesized  $\tau$ -perception process in the optical field [17], i.e. guided motion requires prospective control in the sense that the observer must have information about its future motion trajectory to be able to instantaneously guide its movement successfully.

The above linearization at the moment of activation of the boundary feedback loop gives  $\tau_{min} = \tau(x_{b0}, \dot{x}_{b0})$ . After replacing  $\tau$  in Gray's model with the linearized  $\tau$  term, the following relationship can be determined,

$$K = \frac{(-\dot{x}_{b0}^{-1}\Delta x + x_{b0}\dot{x}_{b0}^{-2}\Delta\dot{x})K_m}{\tau_{min} - \tau_{max}} \quad (7)$$

in which the perception time delay  $\tau_{dp}$  is temporarily ignored. The linear form of Eq. (7) can be transformed into the following, combined with  $\tau_{dp}$ , in the Laplace plane.

$$K(s) = (T_{Lb}s + 1)K_b e^{-\tau_{dp}s} X(s) \quad (8)$$

The final BA pilot model can then be described in the form,

$$K(s) \approx \frac{T_{Lb}s + 1}{T_{Ib}s + 1} K_b X(s) \quad (9)$$

in which  $T_{Lb} = -x_{b0}\dot{x}_{b0}^{-1} = -\tau_{min}$ ,  $K_b = \frac{-\dot{x}_{b0}^{-1}K_m}{\tau_{min} - \tau_{max}}$ , and  $\tau_{dp} = T_{Ib}$ . Therefore, the BA feedback part of

Gray's pilot model with the nonlinear  $\tau$  variable can be approximately simplified into a lead-lag perception term. The resultant closed-loop pilot model is illustrated in Fig. 4.

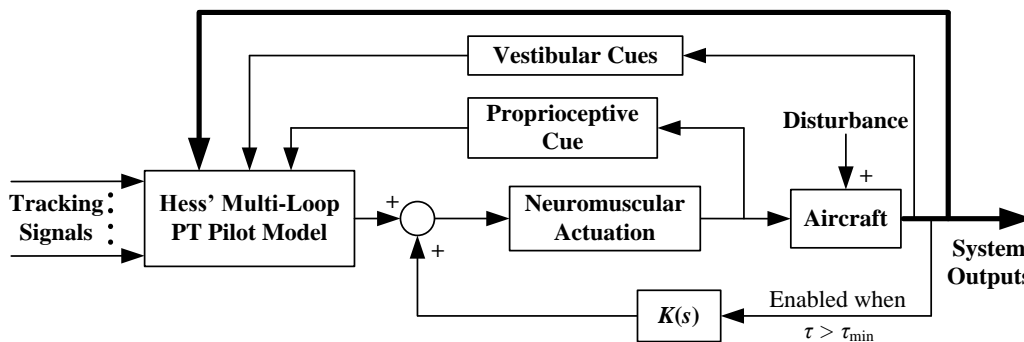


Fig. 4 Closed-loop BAT pilot model with the linearized BA model for a tracking task

This rudimentary level of BA description from the derivation process, combined with Fig. 4, shows the essential features in the study of Boundary-Triggered PIOs in this report. First, the effect of the impending boundary is modelled as an additional positive inner feedback to the closed-loop system. This formula, in essence, describes the BA process as a disturbing influence created by the impending boundary, activated at the moment that  $\tau > \tau_{min}$ , on the primary (outer loop) pursuit task to which the pilot is, until that moment, giving full attention. The positive property of this feedback lies in that, with positive  $K_b$ , the resulting control effects

will become larger as the detected boundary is approached (larger  $X(s)$ ). Therefore, the stability of the closed-loop system pilot-vehicle dynamics can be changed and the BA process can therefore serve as a PIO trigger. The Boundary-Triggered PIO onset detection can be estimated by analysing the effects of the inner linear BA perception-action form on the stability of the outer feedback loop system. Second, the structure in Fig. 4 allows the investigation of the continuous contribution of the PT part of the pilot model, even after the BA process has been triggered. This is different from previous work, which assumes that the PT and BA work independently, which may not reflect real pilot control activity in certain circumstances. Overall then, the new structure appears to be an appropriate means to describe the pilot dynamics during a Boundary-Triggered PIO process.

### C. Case Study for Illustration

A case is studied here to help the user to implement the methodology described above. The pilot model capable of ‘flying’ a pitch tracking task is constructed for a 3 degree-of-freedom (DOF) helicopter model with motion cueing simulated to be both off and on. The description of the implementation proceeds as follows. Each individual element of the controller design in Fig. 4 is documented and then the complete pilot model described. The multi-loop PT controller is designed with Hess’s multi-loop procedure first and then a complete BAT pilot model is presented. The Boundary-Triggered PIO incipience is then analysed by investigating the effects of the variation of BAT parameters ( $\tau_{min}$ ,  $K_b$ ) on the stability properties of the closed-loop system.

The 3DOF longitudinal Bo105 model linearized from the non-linear Bo105 model [18] at 80 kts has been used for the investigation. The model is described in more detail in Appendix A. The neuromuscular damping ratio ( $\zeta_{nm}$ ) and natural frequency ( $\omega_{nm}$ ) in Fig. 4 are selected as typical values of 0.707 and 10 rad/s, respectively [11;12]. The actuator for the longitudinal control input is selected as [11]:

$$G_{ACT} = \frac{20^2}{(s+20)^2} \tag{10}$$

By following the procedure outlined above, the model structure used for the investigation is shown in Fig. 5 (motion off) and Fig. 6 (motion on).

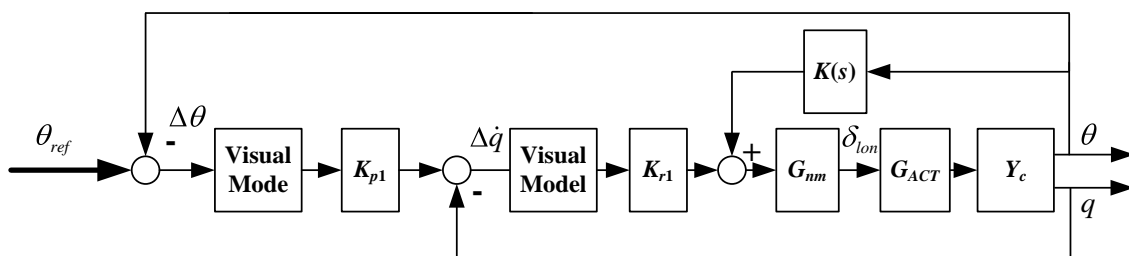


Fig. 5 Pilot model for 3DOF pitch tracking task (motion off)

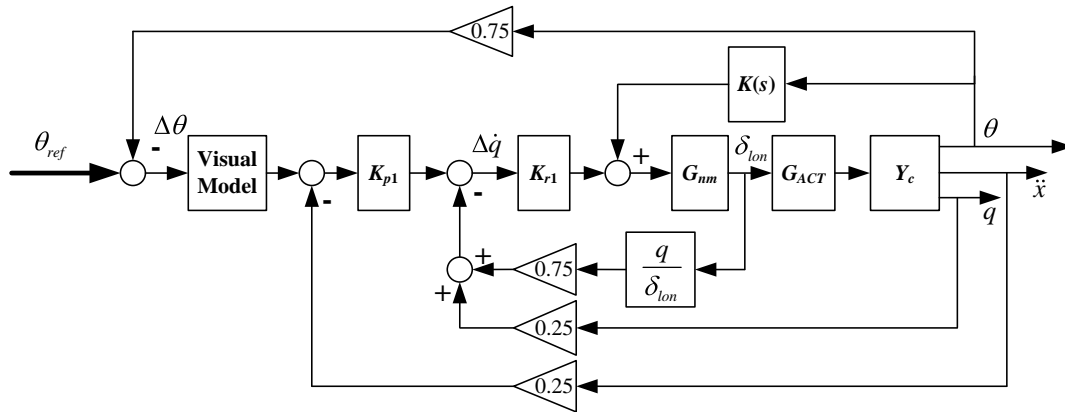


Fig. 6 Pilot model for 3DOF model pitch tracking task (motion on)

Here,  $\theta$  and  $q$  are pitch attitude and rate responses to longitudinal stick input ( $\delta_{lon}$ ). The symbol  $\ddot{x}$  is the surge acceleration. Compared with the simple form in Fig. 5, the structure of Fig. 6 provides more detailed information for pilot modelling. It actually represents a human pilot model that is now able to sense the available vestibular and proprioceptive cues. The transfer function in the proprioceptive feedback loop is suggested in Ref. [13] to be the lowest-order model that matches the pitch-rate response with the longitudinal input and its form is defined as:

$$\frac{\theta}{\delta_{lon}}(s) = \frac{1.268(s + 0.774)}{(s + 5.726)[0.390, 0.734]} \quad (11)$$

in which the parameter set  $[0.390, 0.734]$  determines the damping and natural frequency of the short-term second-order pitch attitude response. Moreover, gain factors with a 0.75/0.25 split in Fig. 6, as described in Ref. [13;15], are used to weight the degree of the importance of each information channel.

Following the design guidelines provided, the gain pairs of  $K_{p1}$  and  $K_{r1}$  in Fig. 5 and Fig. 6 are chosen to be 2.6 and 12.6, and 3.0 and 7.6, respectively. The initial visual model and pilot control behaviour parameters were selected to be:  $\sigma_{vis} = 0.02$  (good visual simulation environment),  $f = 1.2$  (no inter-axis coupling), and  $k_{agress} = 1$  (normal aggression level).

### C.1. Effect of BA Parameters on Basic Pilot-Vehicle System Stability

With the designed PT pilot, the closed-loop system stability in relation to the BAT phenomenon can now be investigated, subject to the variations of the 3 most interesting parameters:  $\tau_{min}$ ,  $K_b$ , and  $\theta_d$ . Previous research has found that the pilot gain and pilot lead effort are the most important factors of the pilot dynamics that correlate with aircraft handling-quality evaluation [8]. For the BA pilot model shown in Eq. (9), the pilot gain and pilot lead are associated with  $T_{Lb}$  ( $\tau_{min}$ ) and  $K_b$ , respectively. Moreover, the main effect of the impending boundary (assuming the pilot needs to be aware of the boundary) is that the pilot needs to immediately adopt a lead compensation control strategy to overcome it with an appropriate control gain. This effect is investigated first by searching the smallest critical  $K_b$  values ( $K_{bc}$ ) that bring the closed-loop system ( $\theta_{ref}/\theta$ ) to the neutral stability condition, with regard to various  $\tau_{min}$  values (up to  $-10s$ ). This is shown in Fig. 7.

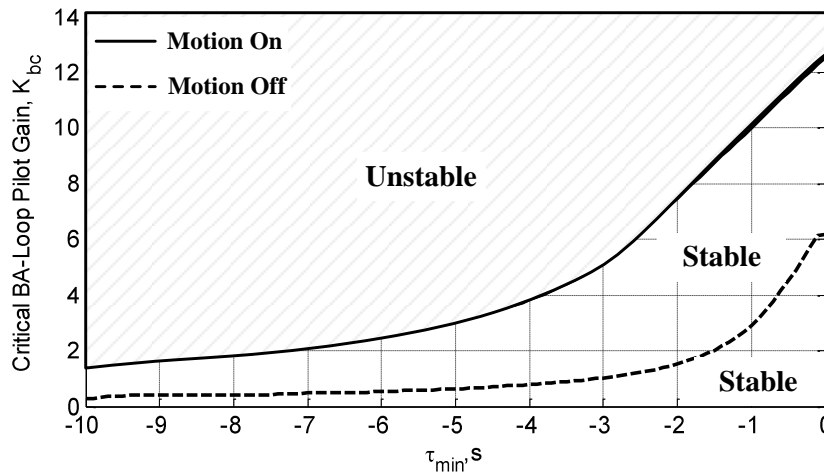


Fig. 7 Pilot-vehicle system stability regions with motion modelled as on and off

Fig. 7 is obtained with the  $\tau_{min}$  range  $(-10, -0.2 \text{ s})$ . The selection of this  $\tau_{min}$  region is based upon the findings of previous research. For example, research into terrain following flight has shown that the pilots rely on motion perception 6-8 seconds ahead but only take action 2-3 seconds ahead [19]. The BAT flight-based trials at the USAF TPS has shown the typical  $\tau_{min}$  range  $(-4, -1.0 \text{ s})$ . Therefore, the expanded range  $(-10.0, 0.0 \text{ s})$  was selected for investigation here to give adequate coverage of all of the likely expected values. The perception time delay  $\tau_{dp}$  value was selected to be 0.1s [3;8]. As shown by Fig. 7, both  $K_{bc}$  curves have an approximately similar shape, but with a significantly improved stability region for motion on. Moreover, the gradient of the stability-separation curves sharply increase as  $\tau_{min}$  increases. This indicates, perhaps counter-intuitively, that the earlier the pilot initiates the BA process, the lower the level of control margin (the stable range of the gain  $K_b$ ) will be available. This provides the pilot with less possibility of recovering from the influence of the approaching boundary. The primary reason for  $K_{bc}$  reducing as  $\tau_{min}$  (negatively) increases is due to the fact that this situation requires more pilot control effort to generate a lead equalized visual cue, leaving less control margin available for other tasks. The increased amount of lead requirement actually increases the effective time delay of the pilot-vehicle system [3;8;20]. Under these situations, pilot performance can be significantly degraded.

The related open-loop  $(\Delta\theta/\theta$  in Fig. 5) crossover frequency ( $\omega_c$ ) and the open-loop neutral stability frequency ( $\omega_u$ ) where the open-loop phase angle is  $-180^\circ$  with regard to  $K_b$  and  $\tau_{min}$  are plotted in Fig. 8.

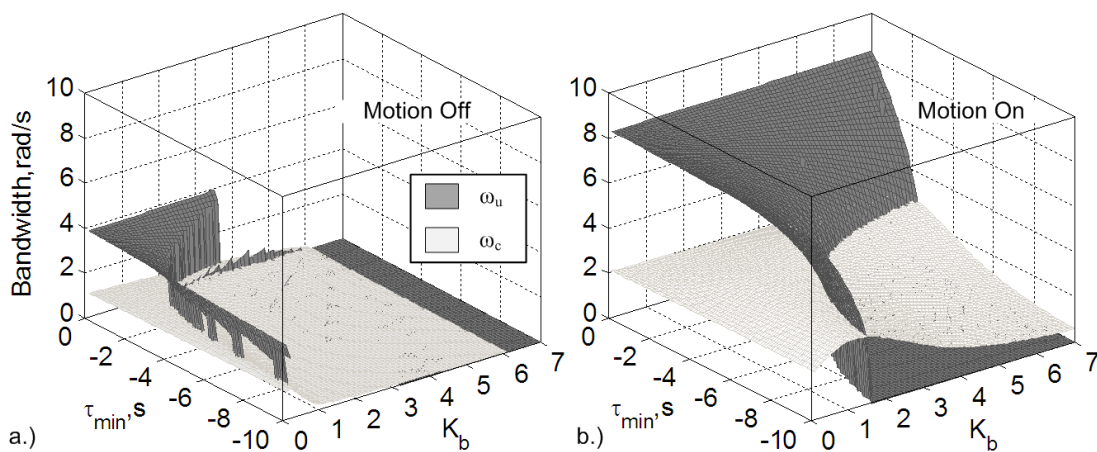


Fig. 8 Change in bandwidth as key BA parameters are varied

Two features can be observed in Fig. 8. First, the substantial influence of the inclusion of the BA loop can be immediately observed by the reduction of two bandwidth characteristic parameters, even reaching close to zero, as  $K_b$  or  $\tau_{min}$  (negatively) increases. The reduction of these performance criteria indicates reduced system stability, or more severely, loss of control (the flat areas in the right-hand corners of Fig. 8). This can be explained as follows. First, the decrease of the distances between  $\omega_c$  and  $\omega_u$  (the left corners in Fig. 8) indicates the rapid reduction of the degree of system stability (i.e. a lower gain margin). Second, according to the following approximate neutral stability relationship that was derived from the crossover model [8], the decreasing  $\omega_u$  value would increase the effective time delay,  $\tau_e$ , and thus the average phase rate. The latter describes the sensitivity of the pilot vehicle system to gain changes near the instability frequency. This again shows the degradation of the system stability. Thirdly,  $\tau_{min}$  has been found to hold as approximately constant for the same task [1;7;21-23]. If analysing Fig. 8 in terms of  $\tau_{min}$ , the results not only show that  $K_b$  governs the sensitivity to pilot adjustments near  $\omega_u$  but also the potential Boundary-Triggered PIO frequency (approximately  $\omega_u$ ), assuming an invariance of the tracking part of the pilot model. Finally, the concomitant reduction in both  $\omega_c$  and  $\omega_{bw}$  is reasonable because the metric  $\omega_c$  has a feedback-system physical interpretation. The decreasing  $\omega_c$  value indicates that the frequency band which can be duplicated in the output response becomes narrower (up to a reduced  $\omega_c$ ). This degrades the benefits of the outer-loop feedback ( $M$  in Fig. 2) and hence the tracking performance. Meanwhile, the ability of the resultant pilot-vehicle system to suppress the high-frequency pilot dynamics and aircraft characteristics will be poorer.

The second feature, noted from Fig. 8, is that the motion-on pilot-vehicle configuration achieves a superior stability performance, being improved by a factor of around 2. Its  $\omega_c$  curve surface initiates from 2 rad/s (at the left corner,  $K_b$  starting from 0.20), complying with the design objective, and then stays at this value over a large region of the parameter space until crossing the  $\omega_u$  surface as  $K_b$  and  $\tau_{min}$  vary. This is the opposite to what can be found in Fig. 8a, where  $\omega_c$  initiates from around 1 rad/s, even though it is designed to be 2 rad/s (without the BA loop,  $K_b = 0$ ). This indicates that with motion on, the introduced BA loop has no significant influence on the pilot control activity (reflected by  $\omega_c$ ) and the consequent closed-loop tracking performance within this region. As  $K_b$  and  $\tau_{min}$  increase, the  $\omega_c$  surface slowly decreases but  $\omega_u$  rapidly drops to zero. Moreover, the transitions of these two frequency parameters vs  $K_b$  and  $\tau_{min}$ , compared with those with motion off in Fig. 8a are smoother.

The main reason for the stability region and bandwidth differences noted in Fig. 7 and Fig. 8 is likely to be due to the increased number of cues being available in the latter case (in Fig. 6) i.e. the inclusion of the vestibular and proprioceptive feedback loops. Refs. [3;8;24] have found that the availability of these cues can lead to a reduction in the effective time delay and thus improved closed-loop stability performance because there is no need to generate angular rate or acceleration information by means of a lead equalized visual cue. These feedback loops can also be thought of as an inner loop which tends to reduce the effective operator time delay. Moreover, the authors, in Ref. [25], have successfully modelled these cues as a negative pitch attitude feedback parallel to the main visual perception channel in their proposed pilot model. The studies in the current report have modelled the BA feedback as positive resulting from the increased lead-equalization control effort used by the human operator due to the impending boundary, through Eq. (9). The results above have demonstrated that the extra BA effort correlates with a reduction in the open-loop frequency bandwidths (in Fig. 8) and the influence of the BA loop on the closed-loop stability and tracking performance equally increases the effective time delay (Eq. **Fehler! Verweisquelle konnte nicht gefunden werden.**). Taken together, the inclusion of the vestibular and proprioceptive feedback loops compensate for the penalty imposed by the addition of the BA loop.

## C.2. Pilot-Vehicle System Stability Characteristics Including Task Boundaries

The discussion above highlights the significant effects that the BA activity can have on the pilot-vehicle system performance. However, the investigation carried out so far only focuses on the stability of the system, without taking into consideration any boundaries or limits. The key facets of the BAT phenomenon stem directly from operational requirements and are hence mission-specific. Therefore, the results shown in Fig. 7 and Fig. 8 may be conservative in that the closed-loop system can be stable but its response, depending on the type of input, may violate the boundary that could be considered to be a fatal error in normal flight operations (if the boundary happened to be the ground level, for example) [1]. Therefore, the boundary-constraint condition must now also be included in the investigation.

Fig. 9 illustrates an idealized BAT experiment, the pitch tracking task.

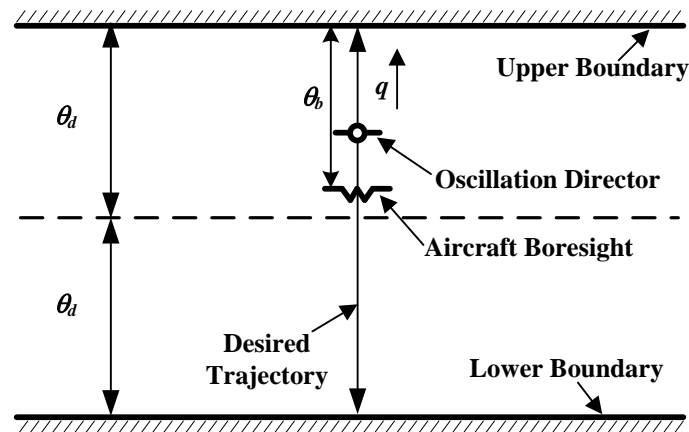


Fig. 9 Illustration of a pitch tracking task including boundary limits

The pitch tracking task of Fig. 9 shows that the pilot (or pilot model) is required to command the aircraft bore sight symbol through the vehicle dynamics to capture a moving target (oscillation director), constrained within 2 boundaries. This is similar to a task flown in a simulation facility for an earlier investigation into rotorcraft pilot couplings, reported in Ref. [26]. For the purposes of this report, the path of the director is composed of four sinusoids as described in Eq. 15,

$$\sin(0.1\pi t) + 3\sin(0.05\pi t) + 2\sin(0.15\pi t) + 3\sin(0.3\pi t) \quad (12)$$

to try to reduce the 'predictability' of a single sinusoidal signal. In order to investigate the properties of the pilot model, the PT pilot model maintains the same ( $K_{r1}$  and  $K_{p1}$ ) for repeated simulations whilst the parameters  $\tau_{min}$ ,  $K_b$ , and  $\theta_d$  have been varied. It is acknowledged that, in reality, as previously discussed, a pilot will most likely adapt his or her dynamic behaviour, e.g. open-loop gain and lead-lag efforts, to changes in the task, environmental and operator-centred variables [3]. However, this does not violate the methodology outlined above in that the approach proposed here essentially focuses on the changes that occur in pilot control behaviour and tracking performance due to the BA process being triggered. With the assumed constant PT pilot effort gains, any observed changes will be exclusively associated with the variations of the BA parameters.

A series of boundary sizes, 6 - 15 deg, with an increment of one degree were selected for this investigation. The lowest boundary size takes the maximum amplitude (6 deg) of the desired combined signal in Eq. (12) into consideration. The exceedance and safe regions under these boundary sizes are illustrated in Fig. 10.

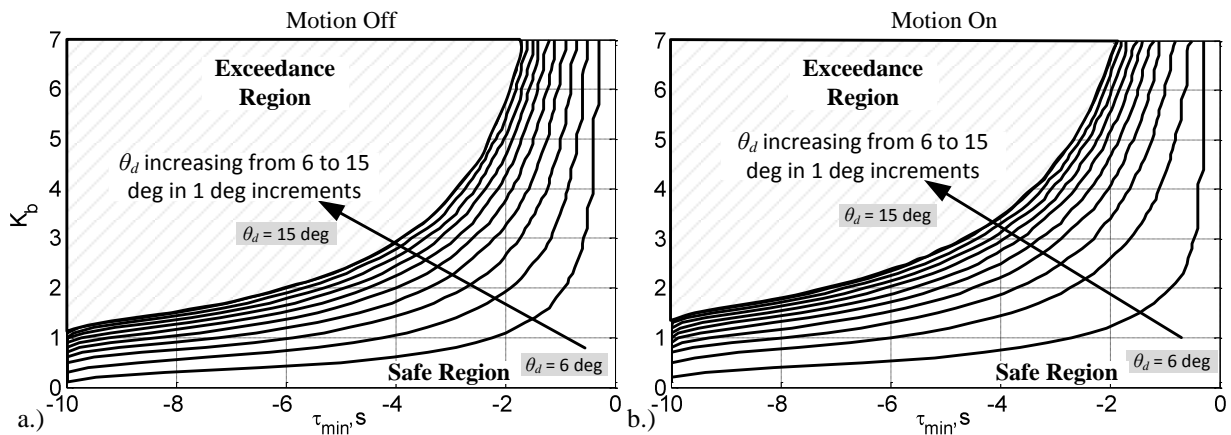


Fig. 10 Boundary-exceedance and safe region variation with boundary size for modelled pitch-tracking task

Fig. 10 shows the profound influence of  $K_b$  and  $\tau_{min}$  values on the safe flight region (entering into either system instability or violation of the boundary limit), subject to the various boundary sizes. These figures show that the safe  $K_b - \tau_{min}$  regions within the designated boundary size become larger as the boundary size increases. This indicates the decreasing influence of the increased boundary size on pilot control activity. Four interesting features can be summarized from Fig. 10. First, for the same  $\tau_{min}$  value, an increased boundary size allows larger attainable pilot effort ( $K_b$ ) and gives the pilot more control margin to avoid the impending boundary. This is reflected by the smaller  $\tau_{min}$  values in particular, where there is no limitation on the  $K_b$  value that can be applied. This is actually a consequence of the BA process not being activated at all. The designed PT pilot model 'ignores' the boundary for a given boundary size where the  $\tau_{min}$  values are relatively small. For example, for the designed experimental configuration, the boundary has no influence on the closed-loop tracking task when  $\tau_{min} > -1.0$  s in the case of  $\theta_d = 8$  deg, as shown in Fig. 10. Moreover, the larger boundary size will result in a larger negative  $\tau_{min}$  threshold. Second, compared with those in Fig. 10, the proposed stability curve in Fig. 7 follows a similar shape, but appears to be too conservative, as expected, especially within the low  $\tau_{min}$  range. The main reasons have been given above. However, the curve in Fig. 7 is still useful because it illustrates the gross degree of the closed-loop system stability associated with the BA process, without requiring the prior knowledge of the desired tracking signal and the boundary size or other mission-specific details. Third, for the same  $K_b$  value, the safe range over which the modelled pilot does not exceed the boundary will decrease as  $\tau_{min}$  becomes negatively larger. This is reasonable in that for the same boundary size, the negatively larger  $\tau_{min}$  means more lead-equalization effort is required. This will increase the effective time delay, as discussed above. Finally, the better closed-loop performance shown in Fig. 7 and Fig. 8, compared with each boundary size, is also reflected in the larger safer region in Fig. 10.

With the derived safe region of Fig. 10, the tracking performance for these boundary sizes is predicted in Fig. 11. The tracking performance is defined as the root-mean-squared (RMS) difference between the desired (Ref) and simulated (Sim) pitch attitude responses.

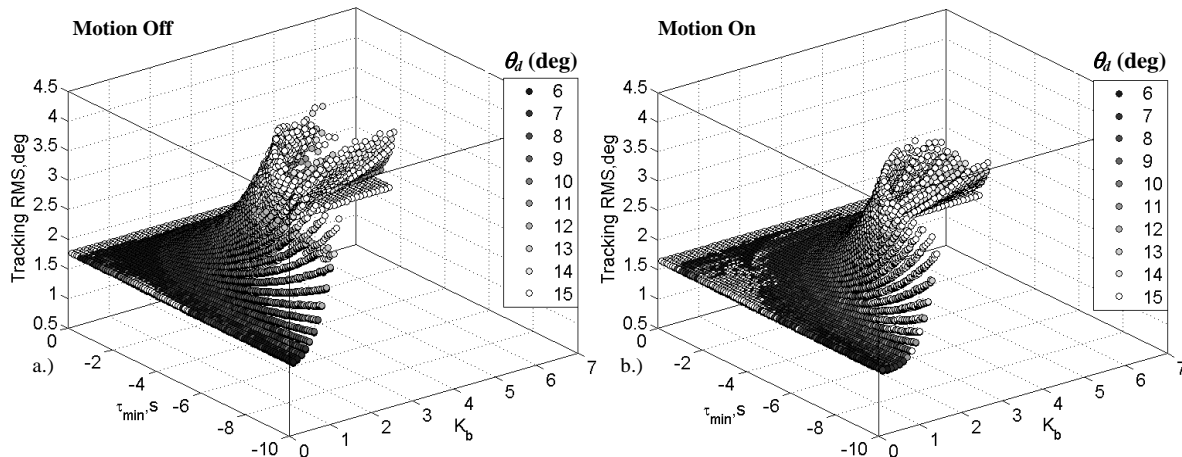


Fig. 11 Tracking RMS variation with different  $K_b$  and  $\tau_{min}$  values with motion simulated to be on and off

Fig. 11 shows the variation of the root-mean-square error obtained for the pitch tracking task for different boundary sizes as key model parameters are varied. The results obtained can be summarized as follows. First, because the positive feedback property of the BA loop has a significant influence on the closed-loop stability in Fig. 8 and Fig. 10, it is to be expected that the larger positive feedback from the inner loop will result in a larger tracking error, arising from the reduced open- and closed-loop bandwidths. The distribution of the tracking RMS performance in Fig. 11 confirms this expectation as  $K_b$  increases. In addition, the tracking performance also deteriorates as the lead effort increases. This is also in accordance with the shapes of the safe-exceedance boundary lines predicted in Fig. 10.

Second, the smaller boundary size results in a narrower safe region in Fig. 10 and a worse tracking performance, shown by the darker region in Fig. 11. Previous studies [7;21;22] also found that the tracking performance degrades when a certain ‘critical’ boundary size is reached and this can even lead to Boundary-Triggered PIO situations. This primarily results from the reduced control margin for the smaller boundary size that makes the pilot more susceptible to system safety maintainability problems (i.e. a narrower safer region) as illustrated in Fig. 10. If the boundary size is too narrow, for the same  $\tau_{min}$  value, a small increase in  $K_b$  as the boundary approaches will cause a violation of the safe region.

Third, the two configurations depict a similar RMS-value distribution. However, the RMS values with motion on in Fig. 11b, at the base of the distribution curve, are slightly improved (by approximately 4%) when compared with those of Fig. 11a. This is to be expected since the frequency bandwidths associated with  $\omega_c$  and  $\omega_u$  of the motion-on configuration in Fig. 8b are larger than those in Fig. 8a. The larger  $\omega_c$  values lead to better closed-loop tracking performance.

To illustrate how the pilot-model BA control effort varies with various boundary sizes, 3 cases with  $\tau_{min} = -2.0$  and  $K_b = 2$  with boundary sizes of 6, 10, and 15 deg have been selected. The simulation results with motion off and on are presented in Fig. 12 and Fig. 13, respectively.

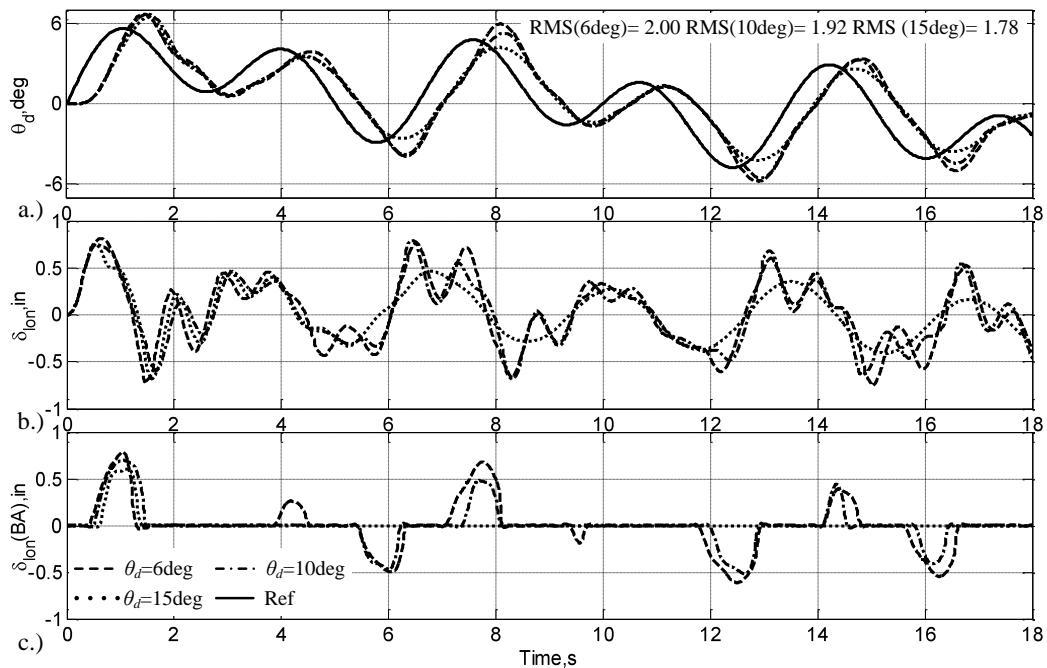


Fig. 12 Effect of the boundary with normal pilot aggressiveness (motion off,  $k_{agress} = 1$ )

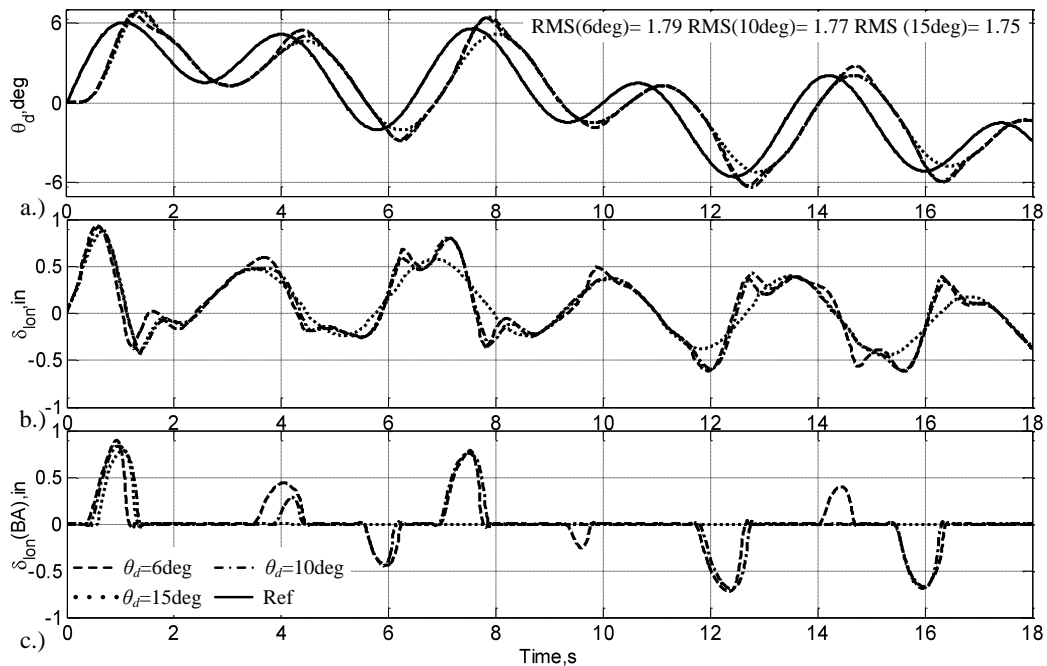


Fig. 13 Effect of the boundary with normal pilot aggressiveness (motion on,  $k_{agress} = 1$ )

Fig. 12 and Fig. 13 show the significant influence of the impending boundary on the pilot control behaviour and the resultant tracking performance. The location of the selected  $\tau_{min}$  and  $K_b$  values in Fig. 10, for both configurations, predict that the case with  $\theta_d = 6$  deg will result in a boundary-exceedance situation whilst the other 2 cases will be successful. The results here confirm these predictions. Moreover, the observed decreasing influence of the BA task on the outer-loop control activities when far from the boundary, is analogous to the recommended strategy to address PIO situations i.e. to back out of the control loop [27]. Finally, the impending boundary introduces extra pulse-like pilot BA control effects and these further results in the severe variations in the pilot's longitudinal stick control ( $\delta_{lon}$ ), especially

for the motion-off case. As the boundary size progressively increases, Fig. 12 and Fig. 13 also show that the resultant influence becomes significantly weaker ( $\theta_d = 10$  deg) and then quickly disappears after experiencing an initial influence ( $\theta_d = 15$  deg).

In addition to these results, the comparisons between Fig. 12 and Fig. 13 indicate that, for this tracking task, the motion and proprioceptive cues available have resulted in better tracking performance (smaller RMS values shown in these figures) and less pilot control activity, in good agreement with the larger  $\omega_c$  bandwidth in Fig. 8.

If the BA gain ( $K_b$ ) is further increased to be as large as 3.5, as illustrated in Fig. 14, a Boundary-Triggered PIO is 'predicted' with motion off.

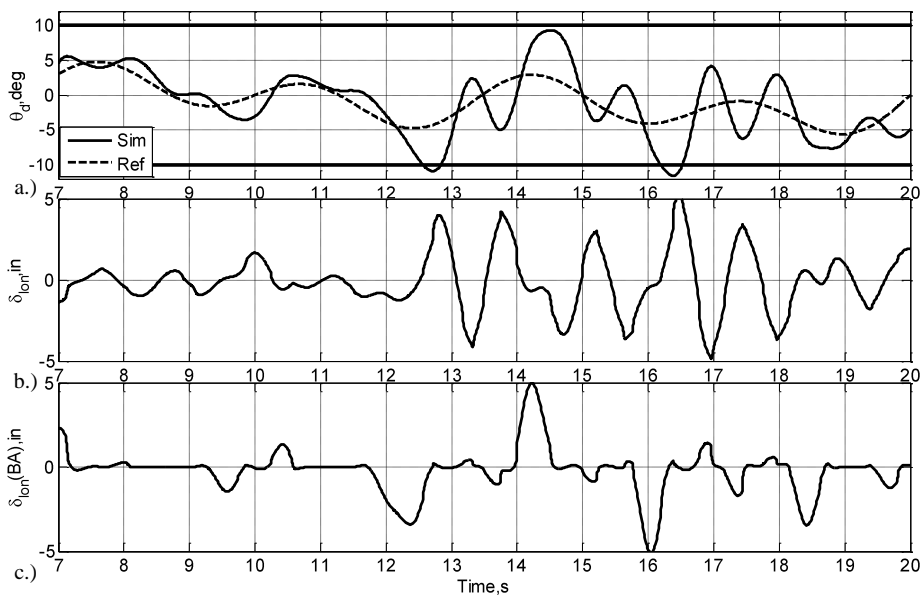


Fig. 14 Simulation results for illustrating Boundary-Triggered PIO (motion off,  $k_{agress} = 2$ )

Fig. 14 shows the motion progressively turns from BAT into a Boundary-Triggered PIO due to the strong influence of the sequentially impending boundaries. This PIO is triggered by the lower boundary (after 12.2 s) and then the closed-loop system enters into oscillatory behaviour (between approximately 12 s and 18.5 s). The effect of these sequential large BA control inputs is so profound that the entire closed-loop system approaches neutral system stability for around 6s. Moreover, this PIO is associated with transitions occurring in the pilot dynamics due to the inclusion of the BA feedback loop that degrades the closed-loop stability, as shown in Fig. 10. The "bang-bang" features of the total control input and the oscillating pitch responses show that the pilot-vehicle system model is adopting an input/output synchronous behaviour with high control effort, which is typical of conventional (C-PIO) cases.

## Appendix A

The 3DOF Bo105 longitudinal model used in this report is described as follows.

$$\dot{\mathbf{x}}(t) = \mathbf{A}\mathbf{x}(t) + \mathbf{B}\delta_{lon} \quad (\text{A1})$$

in which  $\mathbf{x} = u \ w \ q \ \theta$ . The variable  $u$  is the  $x$  body axis velocity,  $w$  is the  $z$  body axis velocity,  $q$  is the pitch rate, and  $\theta$  is the pitch attitude. The matrices  $\mathbf{A}$  and  $\mathbf{B}$  have the following values:

$$\mathbf{A} = \begin{bmatrix} -0.0397 & -0.0012 & 5.9132 & -28.9264 \\ -0.0149 & -0.8543 & 140.9837 & 10.7268 \\ 0.0082 & 0.0318 & -5.5064 & -4.0324 \\ 0 & 0 & 0.9997 & 0 \end{bmatrix} \quad \mathbf{B} = \begin{bmatrix} -1.0278 \\ -3.2261 \\ 1.2680 \\ 0 \end{bmatrix}$$

## Appendix B

The classical pilot cutoff frequency ( $\omega_{cut}$ ) is defined as the frequency point at which the RMS value of the input signal ( $\psi_1$ ) from the frequency range of  $0 - \omega_1$ , is equal to the half of the total RMS of this signal ( $\psi_{tot}$ ), as follows,

$$\frac{\psi_{cut}^2}{\psi_{tot}^2} = 0.5 \quad (\text{B1})$$

in which

$$\psi_{tot}^2 = \frac{1}{2\pi} \int_0^{\infty} G_{\delta\delta} d\omega \quad \text{and} \quad \psi_1^2 = \frac{1}{2\pi} \int_0^{\omega_1} G_{\delta\delta} d\omega \quad (\text{B2})$$

and  $G_{\delta\delta}$  is the auto spectrum of the signal, which is normally obtained the standard Fourier transform.

## References

- [1] Gray III, W. R., "Boundary-Avoidance Tracking: A New Pilot Tracking Model," *AIAA Atmospheric Flight Mechanics Conference and Exhibit*, San Francisco, California, Aug., 2005, pp. 86-97.
- [2] Gray III, W. R., "Boundary-Escape Tracking: A New Conception of Hazardous PIO," Technical report, Air Force Flight Test Center, EDWARDS AFB CA, Sep 2004.
- [3] McRuer, D. T., Clement, W. F., Thompson, and R. E. Magdaleno, "Minimum Flying Qualities Volume II: Pilot Modelling For Flying Qualities Application," Flight Dynamics Laboratory, Air Force Systems Command, Wright-Patterson Air force Base, OHIO, WRDC-TR-89-3100, Jan.1990.
- [4] Allen, R. W., Clement, W. F., and Jex, H. R., "Research on Display Scanning, Sampling, and Reconstruction Using Separate Main and Secondary Tracking Tasks," NASA Contractor Report CR-1569, NASA Contractor Report CR-1569, Jul. 1970.
- [5] Anon., "Aeronautical Design Standard Performance Specification Handling Qualities Requirements for Military Rotorcraft", ADS-33E-PRF, US Army Aviation and Missile Command, Aviation Engineering Directorate, Redstone Arsenal, Alabama, Mar. 2000.
- [6] Brinkerink, N., and Pavel, M. D., "Capturing the Switch between Point Tracking and Boundary Avoiding Pilot Behaviour in A PIO Event," *Proceedings of the 4th Rotorcraft Handling Qualities Conference*, Liverpool, UK, November 4-8, 2008.
- [7] Dotter, J. D., "An Analysis of Aircraft Handling Quality Data Obtained From Boundary Avoidance Tracking Flight Test Techniques," Air Force Inst. of Tech., Wright-Patterson AFB, OH. Graduate School of Engineering and Management, Mar. 2007.
- [8] McRuer, D. T., and Krendel, E. S., "Mathematical Models of Human Pilot Behaviour," AGARD-AG-188, Jan.1974.
- [9] Pavel, M. D., Malecki, J., Dang Vu, B., Masarati, P., Gennaretti, M., and Jump, M., "A Retrospective Survey of Adverse Rotorcraft Pilot Couplings in European Perspective," *68<sup>th</sup> Annual Forum of the American Helicopter Society*, Fort Worth, Texas, May 2012.

- [10] Hess, R.A., "Unified Theory for Aircraft Handling Qualities and Adverse Aircraft - Pilot Coupling," *Journal of Guidance, Control, and Dynamics*, published online Nov. 1997; Vol. 20, No. 6, pp. 1141-1148. doi: 10.2514/2.4169
- [11] Hess, R.A., "Simplified Approach for Modelling Pilot Pursuit Control Behaviour in Multi-Loop Flight Control Tasks," *Proceedings of the I MECH E Part G Journal of Aerospace Engineering*, published online 2006; Vol. 220, No. 2, pp. 85-102. doi: 10.1243/09544100JAERO33
- [12] Hess, R.A., "Obtaining Multi-Loop Pursuit-Control Pilot Models From Computer Simulation," *Proceedings of the I MECH E Part G Journal of Aerospace Engineering*, published online Feb. 2008; Vol. 222, No. 2, pp. 189-199. doi: 10.1243/09544100JAERO260
- [13] Hess, R. A., and Marchesi, F., "Analytical Assessment of Flight Simulator Fidelity Using Pilot Models," *Journal of Guidance, Control, and Dynamics*, published online May. 2009; Vol. 32, No. 3, pp. 760-770. doi: 10.2514/1.40645
- [14] Hess, R.A., and Stout, P. W., "Assessing Aircraft Susceptibility to Nonlinear Aircraft-Pilot Coupling/Pilot-Induced Oscillations," NASA/CR-97-207296, 1997.
- [15] Hess, R.A., and Siwakosit, W., "Assessment of Flight Simulator Fidelity in Multiaxis Tasks Including Visual Cue Quality," *Journal of Aircraft*, published online Jul. 2007; Vol. 38, No. 4, pp. 607-614. doi: 10.2514/2.2836
- [16] Bootsma, R. J., and Craig, C. M., "Information Used in Detecting Upcoming Collision," Perception, published online 2003; Vol. 32, No. 5, pp. 525-544. doi: 10.1068/p3433
- [17] Lee, D. N., "Guiding Movement by Coupling Taus," *Ecological Psychology*, published online 1998; Vol. 10, No. 3, pp. 221-250. doi:10.1207/s15326969eco103&4\_4
- [18] Jones, M., Jump, M., Lu, L., Pavel, M., and Yilmaz, D., "The Use of the Phase-Aggression Criterion for Identification of Rotorcraft Pilot Coupling Events," *38th European Rotorcraft Forum*, Amsterdam, Netherlands, Sept. 4<sup>th</sup>-7<sup>th</sup> 2012.
- [19] Padfield, G. D., Lee, D. N., and Bradley, R., "How Do Helicopter Pilots Know When to Stop, Turn or Pull Up?," *Journal of the American Helicopter Society*, published online 2003; Vol. 48, No. 2, pp. 108-119. doi: 10.4050/JAHS.48.108
- [20] McRuer, D. T., "Pilot-Induced Oscillations and Human Dynamic Behaviour," NASA Contractor Report 4683, Jul.1995.
- [21] Blake, R.D. *Boundary Avoidance Tracking: Consequences (and Uses) of Imposed Boundaries on Pilot-Aircraft Performance*, MSc Thesis, Department of the Air Force, United States Air Force Institute of Technology, Wright-Patterson Air Force Base, Ohio, 2009.
- [22] Gray III, W. R., "Handling Qualities Evaluation at the USAF Test Pilot School," Proceedings of the AIAA Atmospheric Flight Mechanics Conference 10 - 13 August 2009, Chicago, Illinois.
- [23] Warren, R. D., "An Investigation of the Effects of Boundary Avoidance on Pilot Tracking," Air Force Inst. of Tech., Wright-Patterson AFB, OH. Graduate School of Engineering and Management, Dec., 2006.
- [24] McRuer, D. T., and Jex, H. R., "A Review of Quasi-Linear Pilot Models," *IEEE Transactions on Human Factors in Electronics*, published online Sept. 1967; Vol. 8, No. 3, pp. 231-249. doi: 10.1109/THFE.1967.234304
- [25] Zaal, P. M. T., Pool, D. M., Van Paassen, M. M., and Mulder, M., "Comparing Multimodal Pilot Pitch Control Behaviour Between Simulated and Real Flight," *Journal of Guidance, Control, and Dynamics*, published online Sept. 2012; Vol. 35, No. 5, pp. 1456-1471. doi: 10.2514/1.56268
- [26] Jump, M., Hodge, S., Dang Vu, B., Masarati, P., Quaranta, G., Mataboni, M., Pavel, M. D., and Dieterich, O., "Adverse Rotorcraft-Pilot Coupling: Test Campaign Development at the University of Liverpool," *34<sup>th</sup> European Rotorcraft Forum*, Liverpool, England, Sept. 16<sup>th</sup> -18<sup>th</sup> 2008.

## Appendix F: Aero-servo-elastic RPC criteria investigation

### (STRAERO)

This appendix presents the parametric investigation of pilot-vehicle interaction based on rotorcraft handling qualities criteria.

The approach has been developed using IAR330 PUMA configuration adopted in ARISTOTEL project, built by POLIMI [1].

Section 1 presents the sensitivity analysis of aero-servo-elastic RPC using eigenvalues analysis.

Section 2 is an application of Bandwidth Phase Delay Criteria (BPD) to determine Cat. I RPC susceptibility.

Section 3 presents the analysis of aero-servo-elastic RPC using Hess criterion for linear dynamics to determine Cat. I and Cat. II RPC susceptibilities.

#### 1. Introduction

The Handling Qualities and Pilot Induced Oscillations criteria based on piloting models have been proposed over the past six decades. The analytical criteria for the specification of handling qualities have two forms: the first are the open-loop criteria such as limits on measured responses or on modes and the second are the closed-loop criteria assuming a pilot feedback structure which are dependent on the accuracy and adequacy of the pilot model forms. These models have been developed extensively to describe, understand and predict pilot behaviour in many classes of vehicles including aircraft and rotorcraft [2,3,4].

This work uses the aero-servo-elastic (ASE) models built by POLIMI through MASST simulation tool [1]. For the PUMA rigid body model with 6 rigid modes a rudimentary Stability and Control Augmentation System was assumed [5] with respect to the Helicopter Aeronautical Design Standards [6].

In this work we have considered both the full ASE model (74 modes) and the rigid body model is take in account for the pilot vehicle coupling Cat. I and II RPC analysis.

Figure 1 shows the block diagram of the active/passive pilot vehicle system into hover/flight level where the vertical and lateral position and pitch and roll attitudes tracking loop acting through collective or longitudinal and lateral cyclic control to cause the position of the vehicle to track a reference signal.

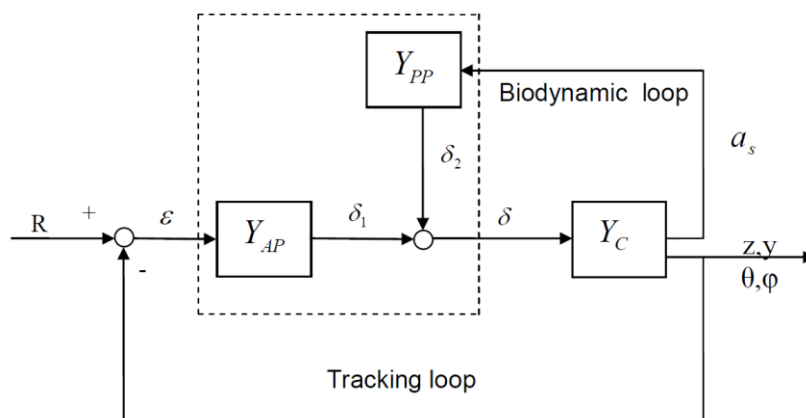


Figure 1 Coupled active/passive pilot –vehicle system

Figure 2 shows a modified block diagram representation using [1] of the aero-servo-elastic model developed for Hess non-linear dynamics criterion.

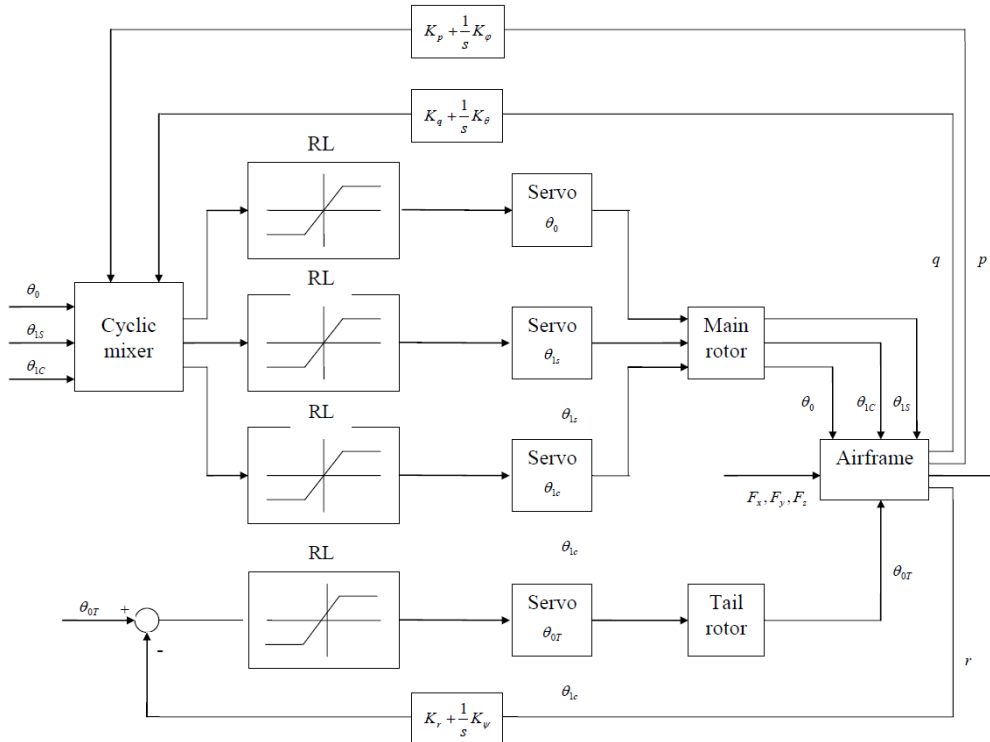


Figure 2 Modified aero-servo-elastic PUMA model with rate limiters [5]

The sensitivity analysis of the active/passive pilot coupled with the vehicle in the loop model has been analysed for hover tasks and the forward flight task only the active pilot in the loop has been coupled with the vehicle.

## 2. Stability analysis

This section investigates the sensitivity analysis on which variations are applied on the following parameters: gain and delay on active control.

The linearised model around the trimmed flight (hover and 80 kts) has been derived from MASST nonlinear simulation model. The loops are closed by voluntary control of active pilot by using the crossover model [1] and involuntary control of the passive pilot by using the transfer function "ectomorphic" model proposed by Mayo as showed in figure 1.

The overall rotorcraft aero-servo-elasticity with the active/passive pilot in the loop are then performed with an eigenvalues analysis method.

### 2.1 Stability analysis in forward flight with active pilot in the loop

In this section the sensitivity analysis of rotorcraft coupled with the active pilot in the loop is performed for the pitch-up and roll-step manoeuvres. The increase of the gain  $K$  and delay lead to marginal stability as show in the following figures. The loops are closed in every case by voluntary control of the crossover active pilot with longitudinal cyclic input for pitch-up task and lateral cyclic input for roll-step task.

The results obtained on the cases description above are showed below (root loci figures contain follow dimensions: Real Axis-1/sec, Imaginary Axis-rad/sec).

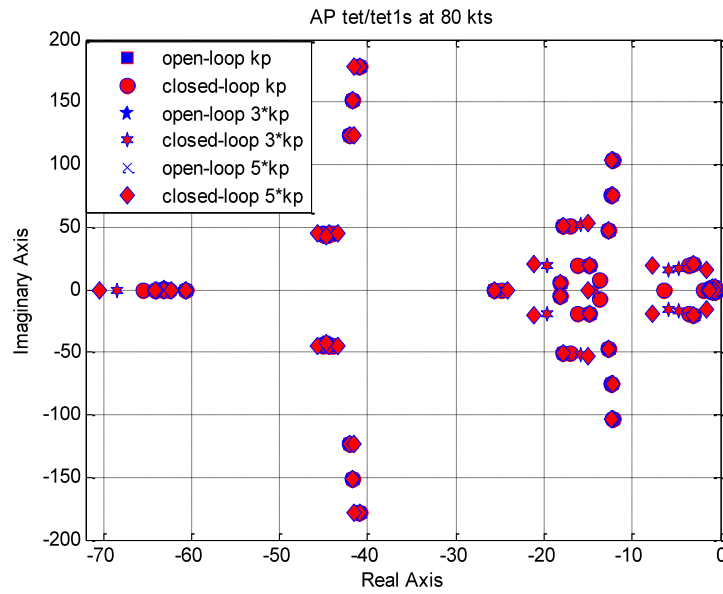


Figure 3 a) Root loci with longitudinal cyclic control with K gain as parameter

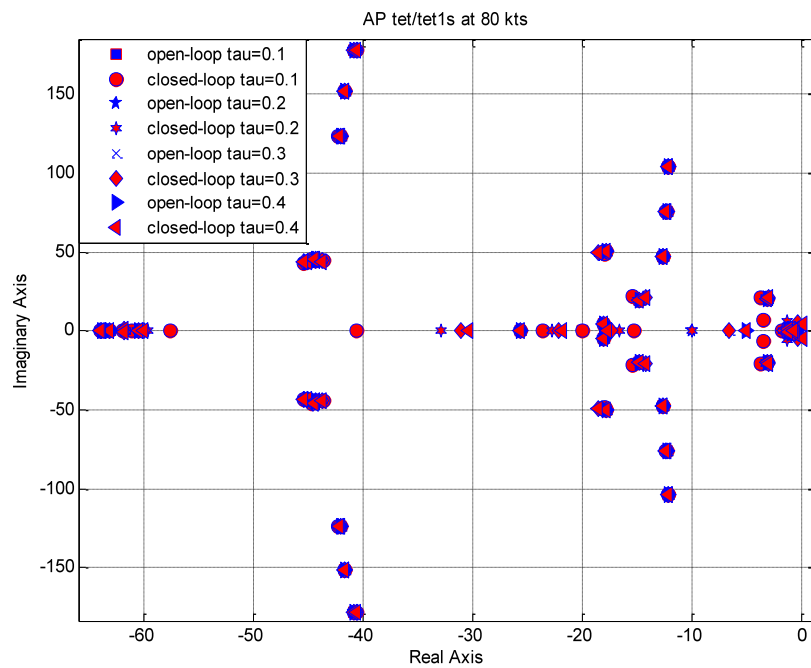


Figure 3 b) Root loci with longitudinal cyclic control with delay as parameter

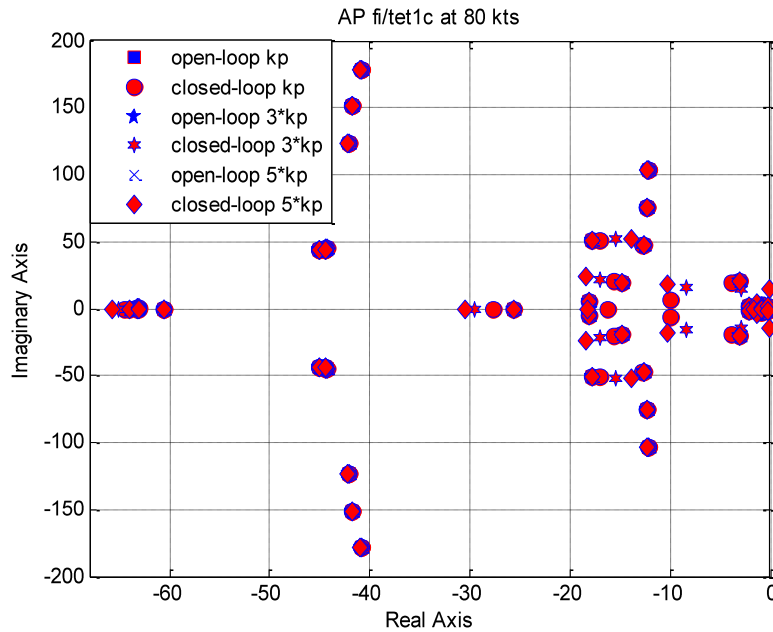


Figure 4 a) Root loci with lateral cyclic control with K gain as parameter

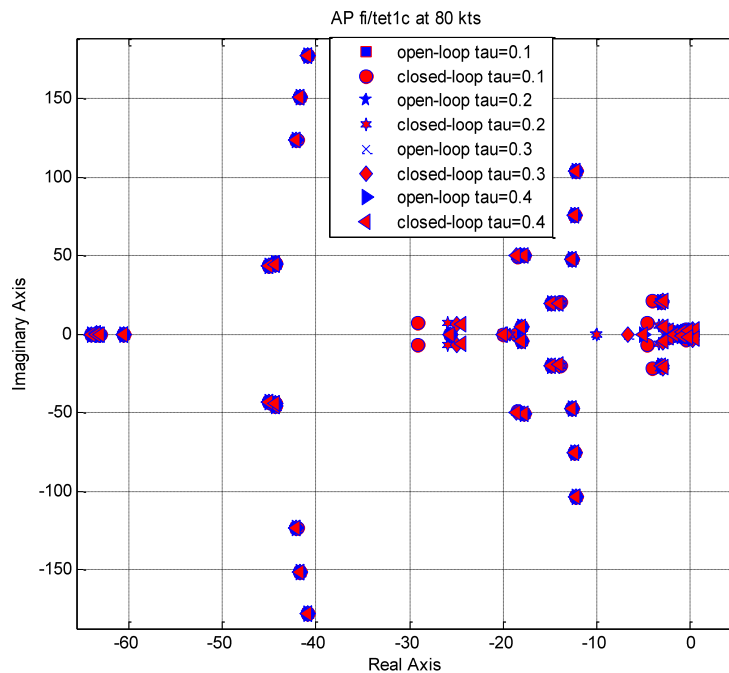


Figure 4 b) Root loci with lateral cyclic control with delay as parameter

## 2.2 Stability analysis at hover with active/passive pilot in the loop

In this section the sensitivity analysis of rotorcraft coupled with the active/passive pilot in the loop is performed in hover flight with pilot closing the loop through the collective and lateral cyclic controls separately. The loops are closed by voluntary control of active pilot by using the crossover model and involuntary control of the passive pilot.

The increase of the gain  $K$  and delay lead to marginal stability or instability as show in the following figures. The results obtained on the cases description above are showed below.

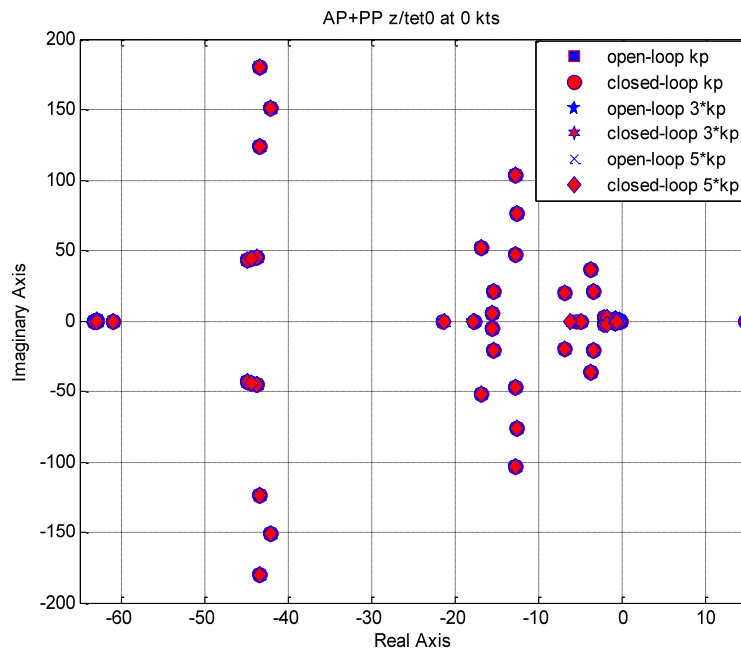


Figure 5 a) Root loci with collective control with  $K$  gain as parameter

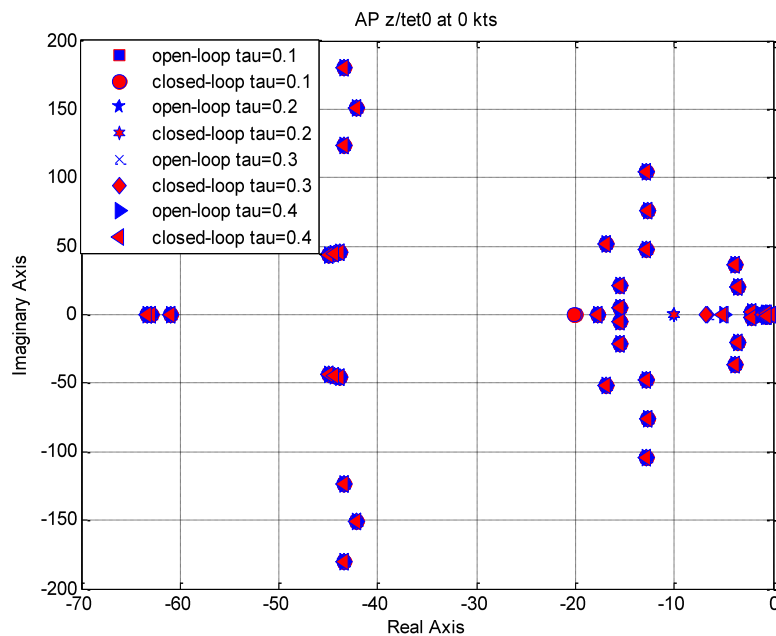


Figure 5 b) Root loci with collective control with delay as parameter

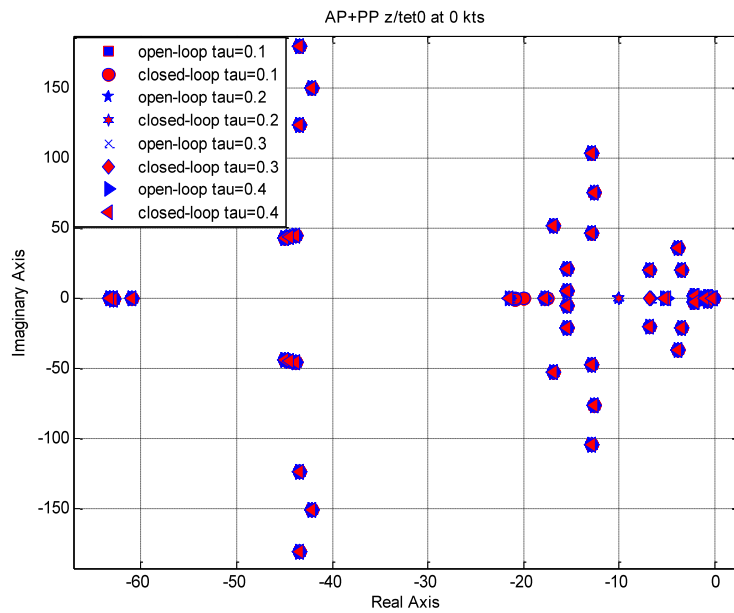


Figure 5 c) Root loci with collective control with delay as parameter

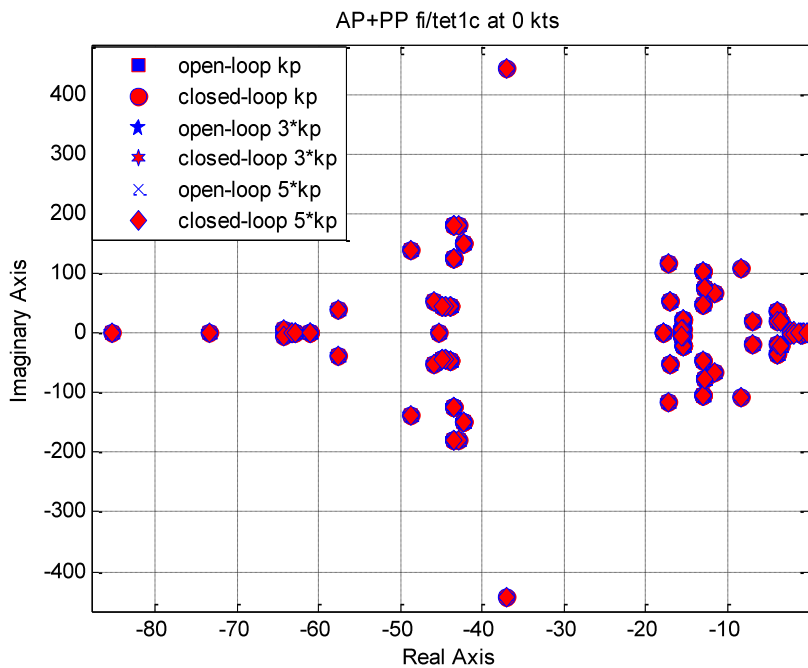


Figure 6 a) Root loci with lateral cyclic control with K gain as parameter

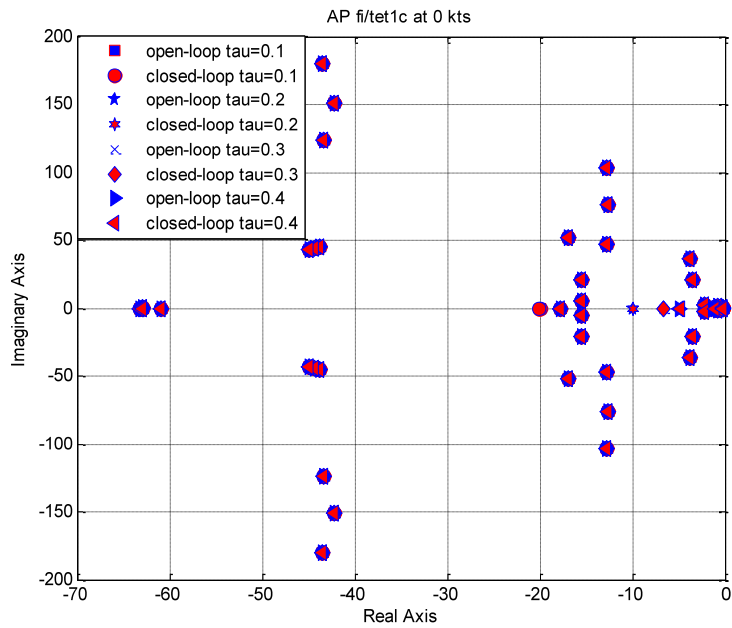


Figure 6 b) Root loci with lateral cyclic control with delay as parameter

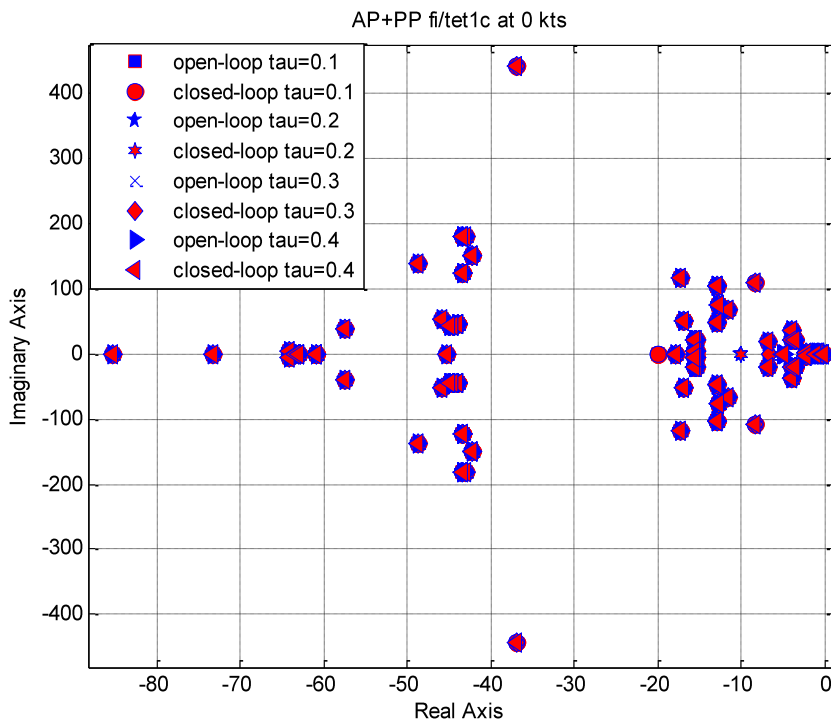


Figure 6 c) Root loci with lateral cyclic control with delay as parameter

### 3. Bandwidth Phase Delay criteria

The bandwidth parameter is indicative of the highest frequency at which the rotorcraft-pilot loop can be closed without threatening stability. The phase-delay parameter represents a measure of the phase angle shape at frequencies above the bandwidth.

The ADS-33 BPD criterion is applied for the pitch and roll attitude responses to the cyclic control in hover and high speed level flight with limits specified in every figures depicted bellow [6].

It can be seen from figure 7 b) that flight configuration has the poorest HQ at high delay.

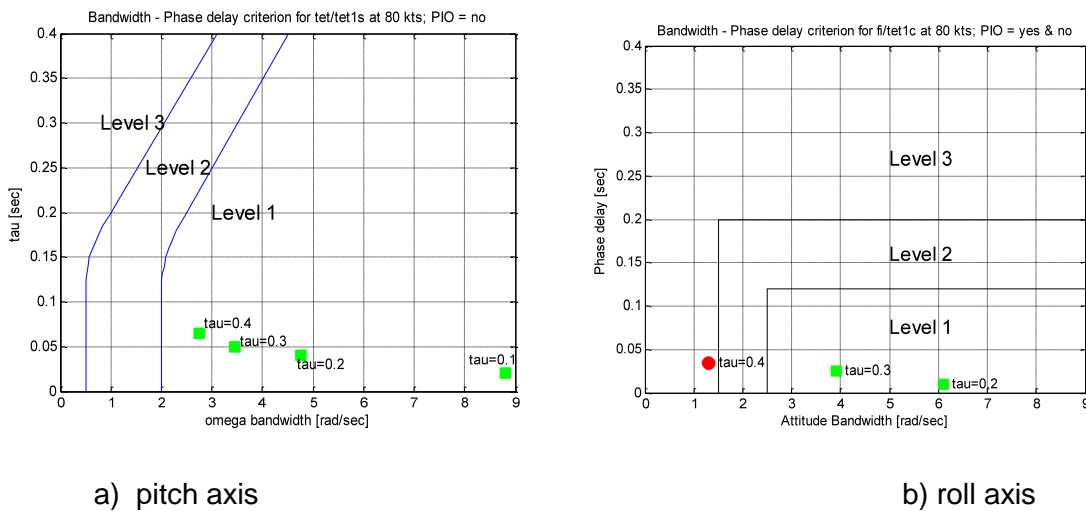


Figure 7 Bandwidth Phase Delay

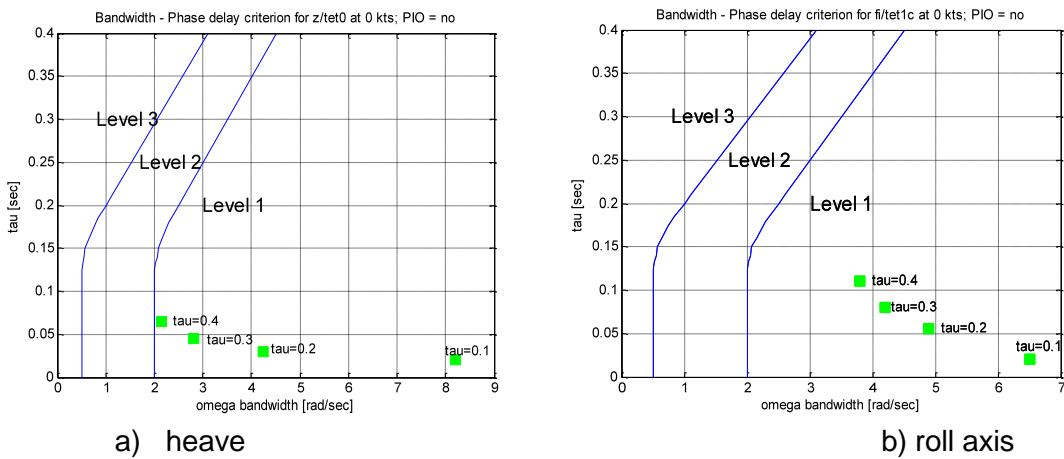


Figure 8 Bandwidth Phase Delay

### 4. Power Spectral Density criteria

The GARTEUR AG-15 and GARTEUR HC-16 action groups were dedicated to deeply research of adverse vehicle-pilot couplings (A/RPC). A refined method for Pilot-in-the-Loop analysis in above programs has been using the Power Spectral Density (PSD) method to predict handling qualities level based on the revised structural model of human operator developed by R. Hess [7]. The key element in this method is evaluation of pilot's control activity in different mission tasks. The metric used to determine PIO susceptibility is the

power spectral density of proprioceptive feedback signal. A pilot-vehicle PSD analysis is studied using the vehicle configurations from POLIMI database for IAR330 PUMA linearized dynamics [1]. This can provide the prediction of handling qualities level in single axes task with linear or nonlinear dynamics. The study of category I and II RPC/PIO susceptibility is developed by selection of different configuration of linearized rotorcraft dynamics with additional displacement limits element in servo-actuators of control chains. The human pilot model so-called “structural pilot model” developed by R. Hess (derived from a theory introduced by Smith) is capable of capturing the prominent features of human pilot dynamics characteristics for a large class of aerial vehicles and tasks [8,9,10,11,12].

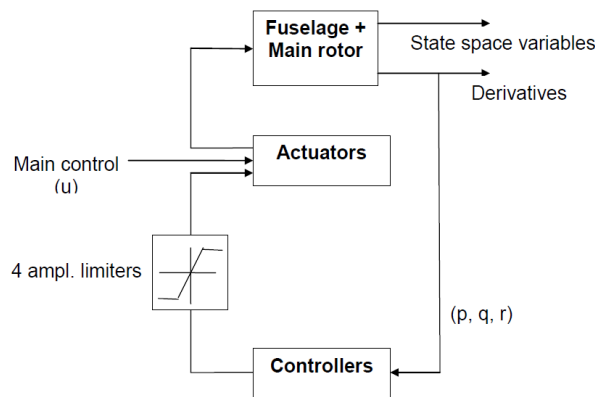


Figure 9 Modified PUMA model with displacement limiters

The structural pilot model gives a more realistic representation of the signal processing structure in the pilot. Its advantage is that for single axis compensatory tracking, the model correlates well with test data. Figure 10 presents the structural pilot model which consists from two parts: the central nervous system and the neuromuscular system, where  $Y_c(s)$  and  $Y_p(s)$  are transfer function of rotorcraft and pilot.

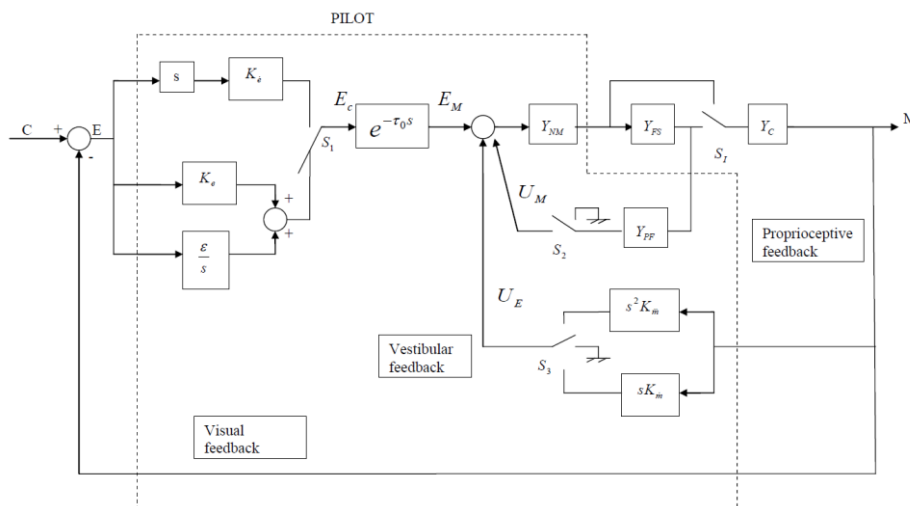


Figure 10 Revised structural pilot model of the human pilot

The behaviour of the rotorcraft coupled with the “structural” pilot in the loop is performed for the “pitch up” manoeuvre.

The handling qualities sensitivity function (HQSF), removing the effects of control sensitivity is defined by:

$$(1) \quad HQSF = \left| M(j\omega) \cdot \Phi(j\omega) \cdot \left( \frac{1}{K_e} \cdot \frac{Y_{PF}(j\omega)}{Y_c(j\omega)} \right) \right|$$

where  $Y_c$  denotes the transfer function of vehicle dynamics,  $M$  is the output of the structural pilot model (SPM),  $C$  is the input to the SPM,  $Y_{PF}$  denotes the transfer function of the proprioceptive feedback element in SPM, whereas  $K_e$  is the error gain in SPM. RPC/PIO assessment technique utilizes the power spectral density (PSD) of a signal  $u_m$  as in reference [7] with control sensitivity removed.

The first member of the eq. 2 represents the normalized PSD of the input.

$$(2) \quad \Phi_{u_m u_m}(\omega) = \frac{2^4}{\omega^4 + 2^4} \cdot |HQSF|^2$$

An estimation of HQSF from the simulation of nonlinear pilot/vehicle system may be obtained, using [3] with:

$$(3) \quad HQSF = \frac{\left| \int_0^T u_m(t) e^{-j\omega t} dt \right|_{\omega=\omega_i}}{\left| \int_0^T c(t) e^{-j\omega t} dt \right|_{\omega=\omega_i}} \cdot \left| \frac{1}{K_e} \right| \quad i = 1, \dots$$

with  $u_m$  denoting the proprioceptive feedback signal in the SPM and  $c(t)$  denoting the time evolution of the input to the SPM.

Here we have a ratio of Fourier transformation with the upper limit of  $T=10$  sec. in our study cases. The bounds on HQSF and the normalized  $\Phi_{u_m u_m}(\omega)$  define the HQ levels and PIOR

levels established for linear systems demonstrate their utilities as well as for nonlinear systems. Figures 11 – 18 presents HQ and PIO levels for the IAR 330 PUMA helicopter MASST generic model in hover and flight level 80 kts conditions. Of course the boundaries plotted in this figures are valid for the fixed wing but they have been plotted to understand where helicopter reference model shows different levels in above specified conditions. In our study cases we choose the time delay  $\tau_e$  and error gain  $K_e$  in structural pilot model obtained from [13].

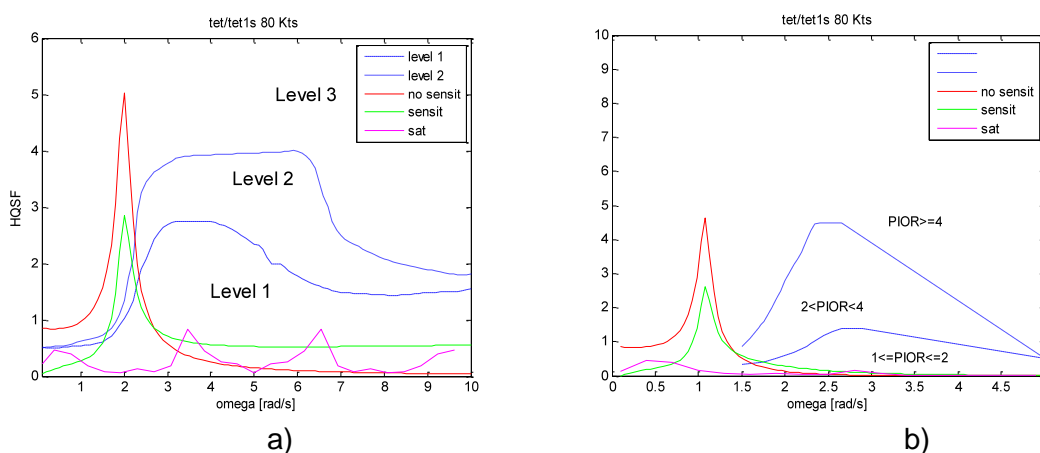


Figure 11 (RB) - a)HQSF for flight level configuration with longitudinal cyclic displacement limit; b) Normalized  $\Phi_{u_m u_m}(\omega)$  for flight level configuration with longitudinal cyclic displacement limit

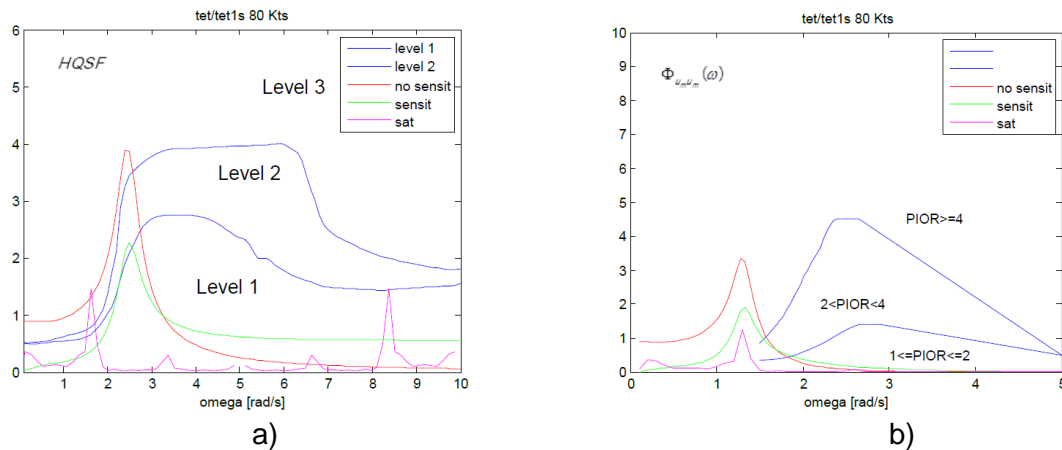


Figure 12 (ASE) - a)HQSF for flight level configuration with longitudinal cyclic displacement limit; b) Normalized  $\Phi_{u_m u_m}(\omega)$  for flight level configuration with longitudinal cyclic displacement limit

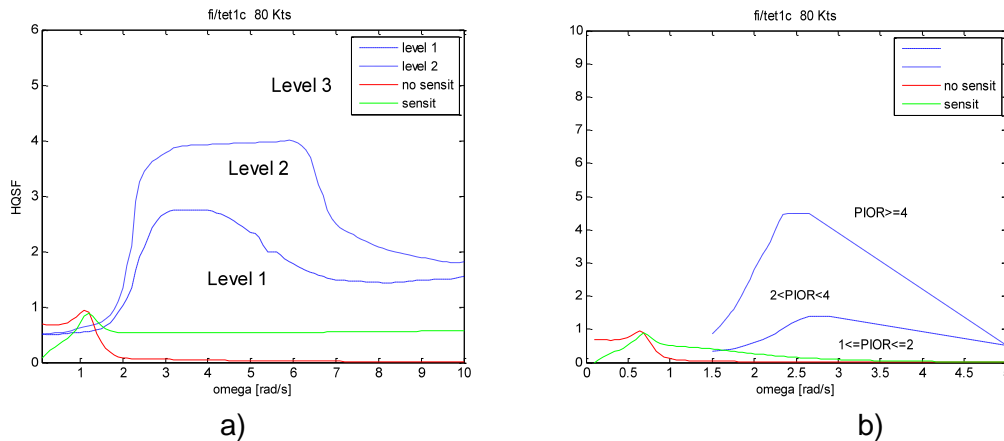


Figure 13 (RB) - a)HQSF for flight level configuration with lateral cyclic displacement limit; b) Normalized  $\Phi_{u_m u_m}(\omega)$  for flight level configuration with longitudinal cyclic displacement limit

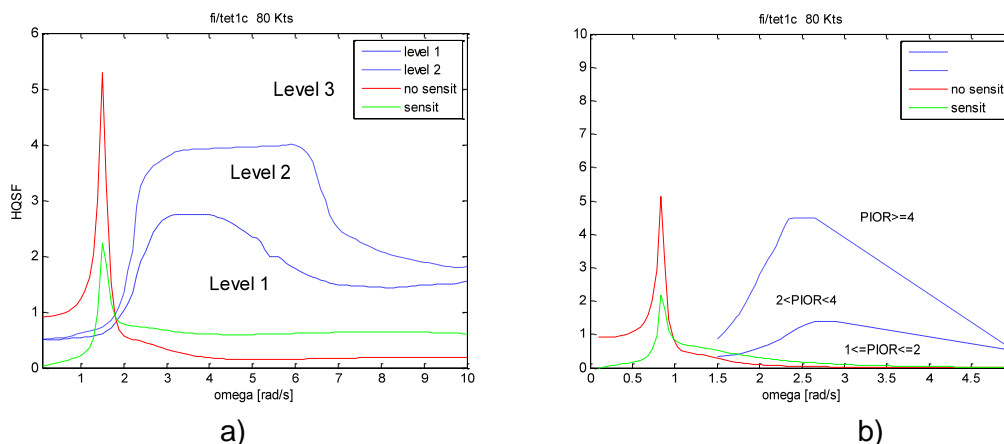


Figure 14 (ASE) - a)HQSF for flight level configuration with lateral cyclic displacement limit; b) Normalized  $\Phi_{u_m u_m}(\omega)$  for flight level configuration with longitudinal cyclic displacement limit

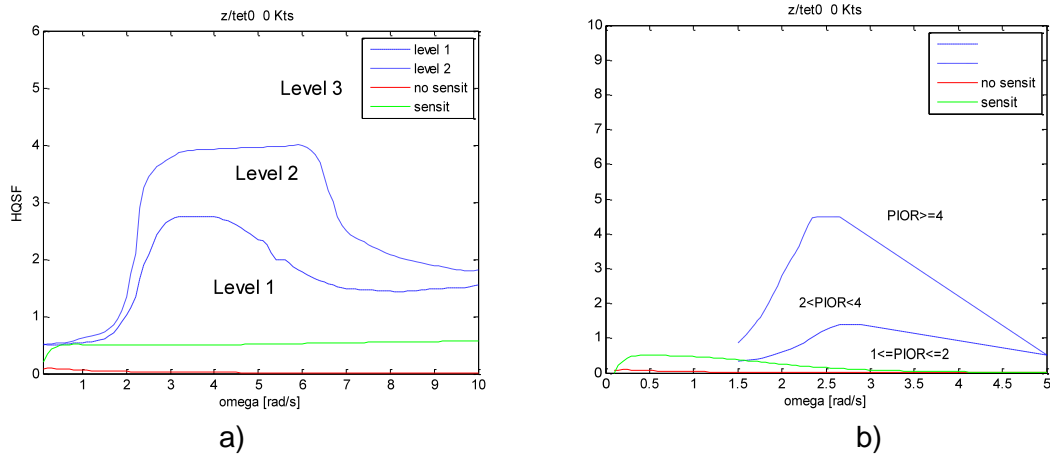


Figure 15 (RB) - a) HQSF for hover configuration with collective displacement limit; b) Normalized  $\Phi_{u_m u_m}(\phi)$  for hover configuration with longitudinal cyclic displacement limit

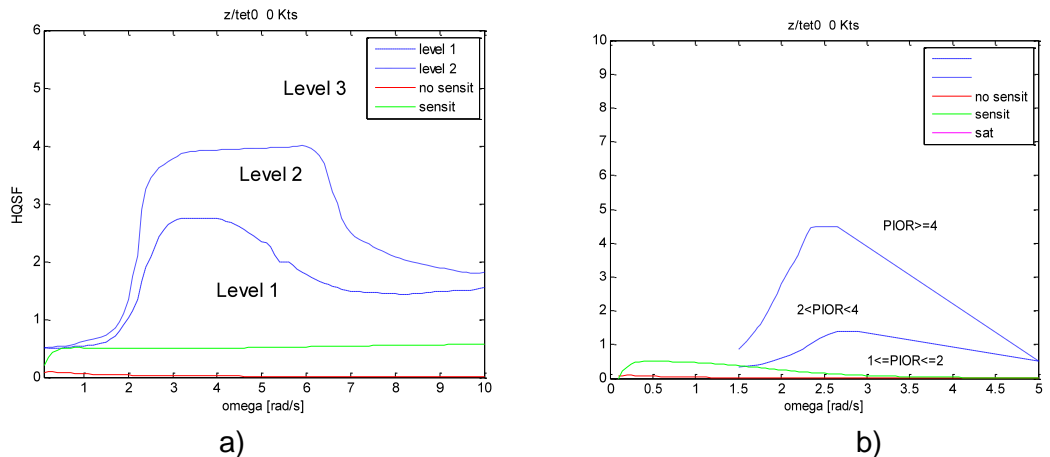


Figure 16 (ASE) - a) HQSF for hover configuration with collective displacement limit; b) Normalized  $\Phi_{u_m u_m}(\phi)$  for hover configuration with longitudinal cyclic displacement limit

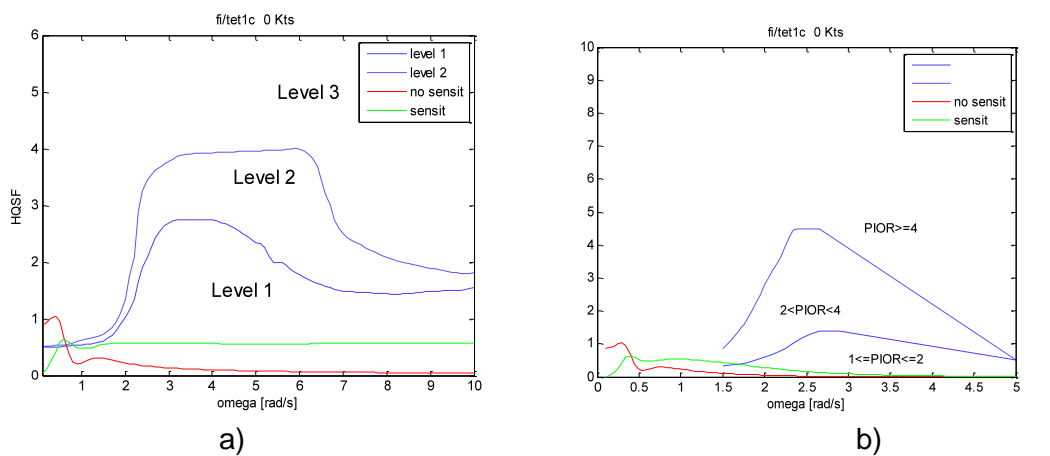


Figure 17 (RB) - a) HQSF for hover configuration with lateral cyclic displacement limit; b) Normalized  $\Phi_{u_m u_m}(\phi)$  for hover configuration with longitudinal cyclic displacement limit

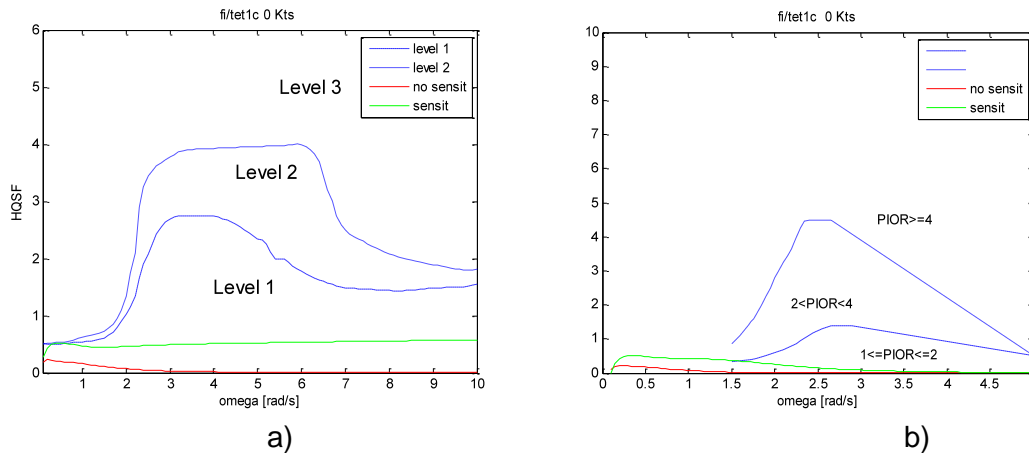


Figure 18 (ASE) - a)HQSF for hover configuration with lateral cyclic displacement limit; b) Normalized  $\Phi_{u_m u_m}(\phi)$  for hover configuration with longitudinal cyclic displacement limit

The above mentioned figures plot for every configuration HQSF and PIOR calculation with and no effects of control sensitivity and in any cases with saturation (with control sensitivity removed).

In flight level conditions with effect of sensitivity HQ rating show a region of level 3 for RB and ASE configurations. The PIO rating if take not in account 0.1- 1.5 rad/sec frequency region show a region of  $2 \leq \text{PIOR} \leq 4$  for RB and ASE configurations.

In hover conditions with effect of sensitivity HQ rating show a region of level 1 for RB and ASE configurations. The PIO rating if take not in account 0.1- 1.5 rad/sec frequency region show a region of  $1 \leq \text{PIOR} \leq 2$  for RB and ASE configurations.

Using a delay in control system these results show that IAR330PUMA is more sensitive in flight level than in hover to RPC according to the low frequency range of the pilot input and correspond to a quick degradation in HQs.

## 5. Conclusion

In summary of the sensitivity analysis the variable K gain produces a root locus of the closed loop system by sweeping from K=1 up to K shows that the stability is lost [14] listed in below table:

Table 1

		RB	ASE
Heave	AP+PP	1,41	1,75
Level Flight 80 kts	Pitch axis	2,37	1,56
	Roll axis	3,15	2,3

The Bandwidth Phase Delay criteria shows a degradation of HQ on roll axis in flight level conditions when delay increase.

The structural pilot model has been applied to the analysis of RPC susceptibility of the IAR330 PUMA in two flight conditions: hover and level flight at 80 kts. The advantage of this model compared with crossover model [3] is that it involves a refined observation of the human central nervous and neuromuscular systems. Compared with Bandwidth Phase Delay criteria, in the structural pilot model criterion the human pilot is tuned to the control system by means of the crossover frequency, so the assumption made for the gains in control system are less important for the predicted results [15].

## References

- [1] Aircraft and Rotorcraft modelling for aero-servo-elastic A/RPC, D3.4/March 2012, ARISTOTEL, FP7/266073/2010.
- [2] “State of the art pilot model for RPC prediction”, report A/RPC, D2.3/April 2011, ARISTOTEL, FP7/266073/2010.
- [3] GARTEUR, Helicopters Panel action group 16: Rigid and aero-elastic rotorcraft pilot coupling – prediction tools and means of prevention, Technical report TP 167, 2008.
- [4] Yamaucchi, G.K., Young L.A. – A Status of NASA Rotorcraft Research, NASA/TP-2009-215369, Ames Research Center; Moffet Field, California, September, 2009.
- [5] ARISTOTEL, Complete Bio-Dynamical Test Data Analysis and Critical Review, Deliverable D4.4, January 2013.
- [6] AGARD, “Flight Vehicle Panel Workshop Pilot Induced Oscillations”, AGARD-AR-335, Feb.1995.
- [7] R. A. Hess, Unified theory for aircraft handling qualities and adverse aircraft pilot coupling, AIAA-Paper 97-0389, 1997.
- [8] Hess R. A. – “Theory for Aircraft Handling Qualities Based on Upon a Structural Pilot Model”, Journal of Guidance and Control, vol.12, No. 6, November-December 1989.
- [9] Hess, R.A., - “Unified Theory for Aircraft Handling Qualities and Adverse Aircraft-Pilot Coupling”, Journal of Guidance, Control, and Dynamics, vol. 20, No. 6, Nov.-Dec., 1997.
- [10] Hess, R.A., Malsbury, T., - “Closed-Loop Assessment of Flight Simulator Fidelity”, Journal of Guidance, Control, and Dynamics, vol. 14, No. 1, Jan.-Feb, 1991.
- [11] Hess, R.A., Marchesi, F., - “Analytical Assessment of Flight Simulator Fidelity Using Pilot Models”, Journal of Guidance, Control, and Dynamics, vol. 32, No. 3, May-June 2009.
- [12] Hess, R.A., - “Modeling Pilot Control Behavior with Sudden Changes in Vehicle Dynamics”, Journal of Aircraft, vol. 46, No. 5, Sept.-Oct., 2009.
- [13] ARISTOTEL – “Aircraft and Rotorcraft modelling for Aero-servo-elastic A/RPC”, Deliverable No. D3.4, March 2012.
- [14] ARISTOTEL – “Prediction of aero-servo-elastic instabilities with and without pilot in the loop”, Deliverable No. D3.9, April 2013.
- [15] Y. Zeyda, R.A. Hess, W. Siwakosit, - Aircraft Handling Qualities and Pilot-Induced Oscillations Tendencies with Actuator Saturation, Journal of Guidance, Control and Dynamics, vol. 22, No. 6, Nov.-Dec. 1999.

### List of Abbreviation

APC	Aircraft Pilot Coupling
A/RPC	Aircraft/Rotorcraft Pilot Coupling
ASE	Aero-Servo-Elastic
BPD	Bandwidth Phase Delay
HQSF	Handling Qualities Sensitivity Function
PIO	Pilot Induced Oscillation
PIOR	Pilot Induced Oscillation Rating
RB	Rigid Body
RPC	Rotorcraft Pilot Coupling

## **Appendix G: Design guidelines for APC prevention (TsAGI, in cooperation with NLR)**

This section presents the application of the approach developed by TsAGI to assess the effect of aircraft structural elasticity characteristics on an elastic aircraft HQ and pilot-aircraft biodynamical interaction and the role of the control inceptor type and its feel system characteristics in this effect. The approach and HQ criterion has been developed in cooperation with NLR and based on the experimental results received in the course of the project.

### **1. Introduction**

It is known that high-frequency accelerations due to structural elasticity can cause involuntary body and limb-manipulator system displacements (i.e. biodynamical feedthrough, BDFT), which interfere with pilot voluntary control activity, and may be the reason for pilot rating worsening. As control inceptor is in the closed control loop, its type and characteristics can amplify the negative effect of the high-frequency accelerations due to structural elasticity and, as a consequence, pilot ratings of elastic aircraft handling qualities HQ. The HQ criterion developed in the course of the project is to assess the pilot rating worsening caused by aircraft structural elasticity and estimate the role of the inceptor type and its feel system characteristics in this effect.

The idea of the HQ criterion is similar to that proposed earlier for the rigid-body aircraft to assess the effect of so-called aircraft abrupt response [1,2,3], but has a number of substantial differences. The main difference is that the criterion takes into account biodynamical interaction in pilot-aircraft system, which depends on inceptor type and its feel system characteristics.

The HQ criterion is based on the results of extensive experiments of different kind: biodynamical tests to estimate BDFT for the systems with different types of control inceptors [4,5] and to identify “biodynamical” and “active” pilot transfer function [6], and piloted experiments to assess the effect of structural elasticity, inceptor type and feel system characteristics on HQ pilot ratings of an elastic aircraft [7,8].

Chapter 2 is, in fact, a Manual for the aircraft designer to assess possible pilot rating worsening of the elastic aircraft at the first stages of its development. It gives a short description of the handling quality criteria, list of parameters required for the assessment and expressions used in calculations.

Chapter 3 is the HQ criterion substantiation and validation, based on the principles determined earlier and experimental data received in the course of the present project.

## 2. Approach to Assess APC Tendency

To assess the APC tendency in the roll control axis and the role of the control inceptor, the following characteristics are required:

- $Y_{ny}$ , aircraft transfer function for the lateral accelerations;
- $Y_p$ , aircraft transfer function for roll rate.

According to the HQ criterion, pilot rating deterioration can be determined according to the empirical function shown in Fig.1 or to the following expression:

$$\Delta PR = \begin{cases} 0, & \text{if } \lambda < 0.02 \\ 2 \lg \lambda + 3.0, & \text{if } \lambda \geq 0.02 \end{cases} \quad (1)$$

Calculation of parameter  $\lambda$  is made in accordance with the following expressions:

$$\lambda = \frac{\sigma_{ny}}{\sigma_p}, \quad (2)$$

where  $\sigma_p$  is the root-mean-square (RMS) of roll rate,  $\sigma_{ny}$  is the RMS of lateral accelerations in the pilot's location caused by structural elasticity oscillations.

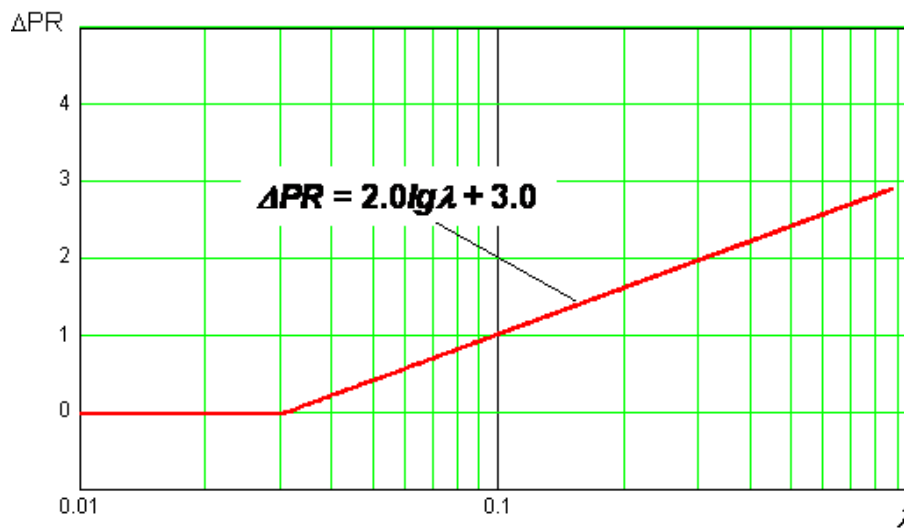


Fig.1. Pilot rating worsening due to biodynamical effect of aircraft structural elasticity and other factors.

Values of  $\sigma_p$  and  $\sigma_{ny}$  in (2) can be found as follows, regardless of the complexity of the aircraft transfer function:

$$\sigma_{ny}^2 = \frac{1}{2\pi} \cdot \int_{-\infty}^{+\infty} |Y_{ny}(j\omega) \cdot Y_{bp}(j\omega)|^2 d\omega \quad (3)$$

$$\sigma_p^2 = \frac{1}{2\pi} \cdot \int_{-\infty}^{+\infty} |Y_p(j\omega) \cdot Y_{ap}(j\omega)|^2 d\omega$$

where  $Y_{ap}$  and  $Y_{bp}$  are transfer functions of the “active” and “biodynamical” pilot models, which are white noise (Fig.2) passing through the filters of the following type:

$$Y_{ap} = \frac{1}{s + \omega_* \cdot K / K_*} \tag{4}$$

where  $K$  is aircraft roll control sensitivity (aircraft gain),  $K_*$  is the “characteristic” value of the aircraft gain, which depends on the control inceptor type: for the wheel it is  $K_* = 0.72 \text{ rad/mm}$ , for the sidestick it is  $K_* = 0.41 \text{ rad/mm}$ .

$$Y_{bp}(s) = \left( \frac{0.4s + 1}{0.5s + 1} \right) \cdot \left[ \frac{1}{T_1^2 s^2 + 2T_1 \zeta_1 s + 1} \right] \tag{5}$$

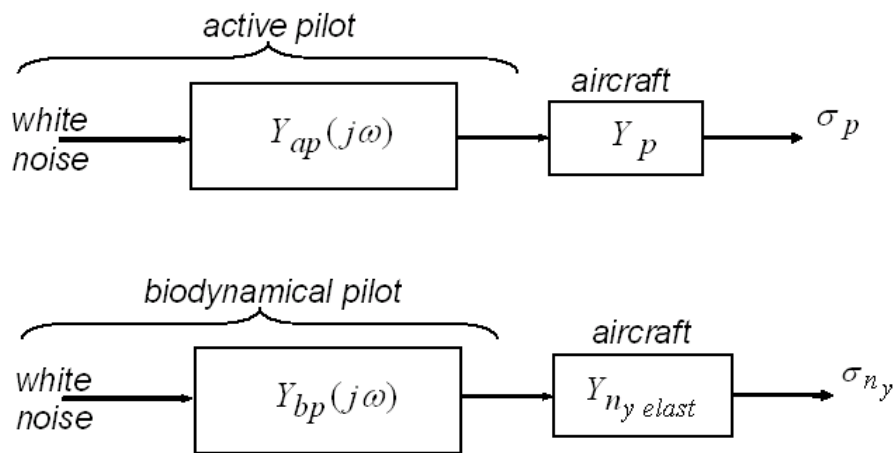


Fig.2. Block scheme to determine RMS of the roll rate and lateral accelerations.

For the control systems with a traditional wheel, the values of parameters  $T_1$  and  $\zeta_1$  can be assumed equal  $T_1 = 0.1 \text{ s}$ ,  $\zeta_1 = 0.7$  regardless of the feel system characteristics; for the systems with sidesticks, they are function of force damping and can be determined in accordance with functions in Fig.3.

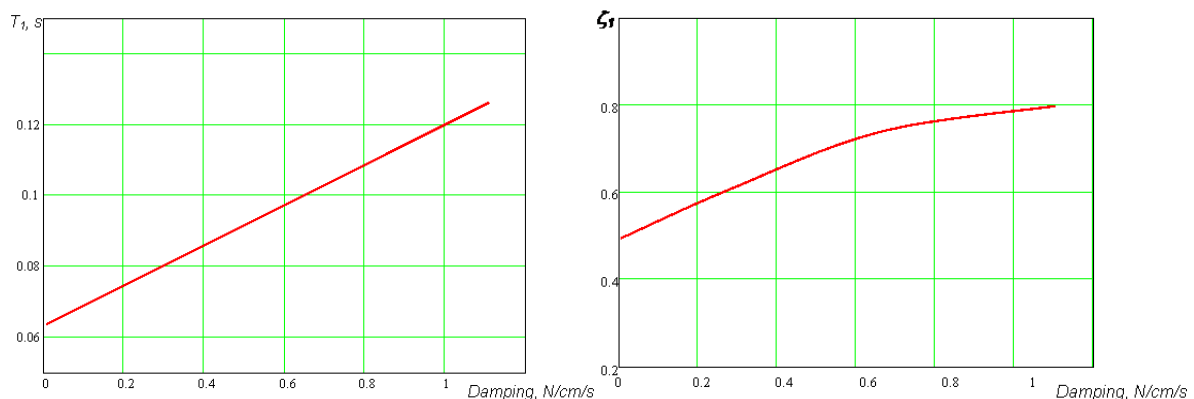


Fig.3. Parameters  $T_1$  and  $\zeta_1$  in (1.5) as functions of sidestick damping.

### 3. Validation of the Approach.

#### 1. Why is the effect of structural elasticity determined by parameter $\lambda$ (2)?

As high-frequency lateral accelerations due to structural elasticity arise as a result of aircraft angular motion, they are perceived by the pilot through angular motion. That is why it is necessary to take into account the effect of angular motion on lateral accelerations perception.

As experimental data received in earlier experiments [1,2,3] show, the perception of the lateral accelerations is proportionate to roll rate amplitude. Thus we can assume that the degree of lateral acceleration negative effect is determined by the ratio ( $\lambda$ ) between the levels of high-frequency lateral accelerations and roll rate. If we express the levels of high-frequency lateral accelerations and roll rates in terms of their RMS, we arrive at expression (2).

#### 2. How to calculate parameter $\lambda$ ?

When a pilot controls an elastic aircraft (Fig.4), (s)he, on the one hand, performs a piloting task, and, on the other hand, he is exposed to the disturbing high-frequency oscillations due to structural elasticity. In other words, pilot control activity (inceptor displacements) consists of two components: deliberately created by a pilot to control an aircraft, and involuntary inceptor displacements due to disturbing high-frequency structural oscillations. The two components can be described by different models corresponding to so-called “active” and “passive” (or “biodynamical”) pilot models.

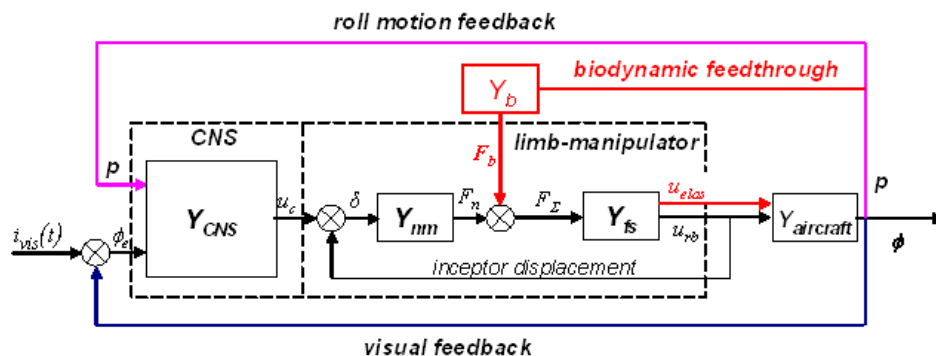


Fig.4. Block-diagram of pilot control activity for an elastic aircraft.

The models have different inputs: for “active” pilot it is a visual signal; for “biodynamical” pilot it is high-frequency oscillations due to structural elasticity. The characteristic frequency ranges of the pilot models are also different: for the “active” pilot it is limited by 1.0-1.5 Hz; for the “biodynamical” pilot is above 1.5 Hz. Thus, in the first approximation, they can be considered independent.

To calculate RMS of the lateral accelerations ( $\sigma_{ny}$ ) and roll rates ( $\sigma_p$ ) in (2), we use random function theory. Assuming the pilot control activity is a stationary random process, the models of the active and biodynamical pilots can be presented as white noise passing through the corresponding filters, as it is shown in Fig.2. For the active pilot model, it is a filter, which reflects pilot activity to control aircraft in roll; for the biodynamical pilot model, it is a filter, which describes pilot’s involuntary control activity caused by high-frequency lateral accelerations.

Expressions (3) logically follow from the Random Functions theory.

3. How “active” pilot model was selected?

In the experiments to select active pilot model [5] the effects of feel system characteristics and roll control sensitivity (aircraft gain) were considered.

Usually, the force gradient is selected from point-of-view of the rigid-body aircraft handling qualities; its optimum values vary in the rather narrow range. As force gradient deflects from the optimum values, the pilot ratings deteriorate: due to (low-frequency) PIO tendency for values smaller than optimum; due to too large inceptor forces for gradient values greater than optimum. The pilot ratings deterioration can be estimated in accordance with the function presented in Fig.5 [9].

It should be mentioned that the subjective pilot ratings appeared to be more “sensitive” to force gradient variation than the pilot describing function.

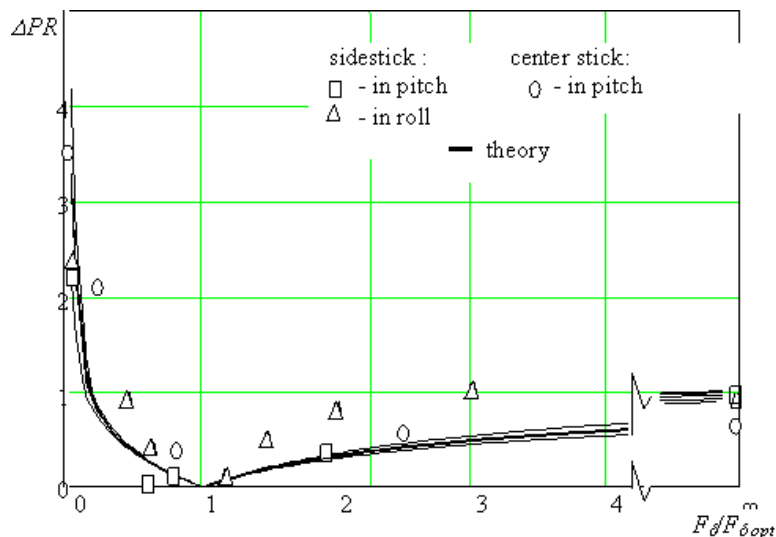


Fig.5. Pilot ratings of the rigid-body aircraft vs inceptor force gradient.

The inceptor damping does not affect active pilot describing function as well for the rather wide range of the parameter variation (from 0 up to very large damping, which is unusual for practice). The point is that at the frequencies typical of active control, the introduction of additional damping does not lead to any noticeable increase of inceptor forces felt by a pilot, and, thus, does not affect handling qualities pilot ratings.

As experimental data showed (Fig.6), within the frequency range of pilot control activity, a pilot can adjust his gain in accordance with the aircraft gain.

Thus, the only factor, which has any noticeable impact on active pilot describing function, is the aircraft control sensitivity. To take this into account, we can use transfer function (4) to describe pilot control activity.

In (4),  $K$  is an aircraft gain (control sensitivity) in the roll rate transfer function;  $K_*$  is a certain constant, which can be interpreted as a “characteristic” value of control sensitivity;  $\omega_* = 1$  rad/s. Parameter  $K_*$  depends on inceptor type and is selected to provide one and the same pilot-aircraft bandwidth for different inceptors and optimum control sensitivity; parameter  $\omega_*$  is to provide identical dimension in the denominator of the formula.

4. How “biodynamical” pilot model was selected?

As opposed to the active pilot model, the biodynamical pilot model is much dependent on the inceptor type and feel system characteristics.

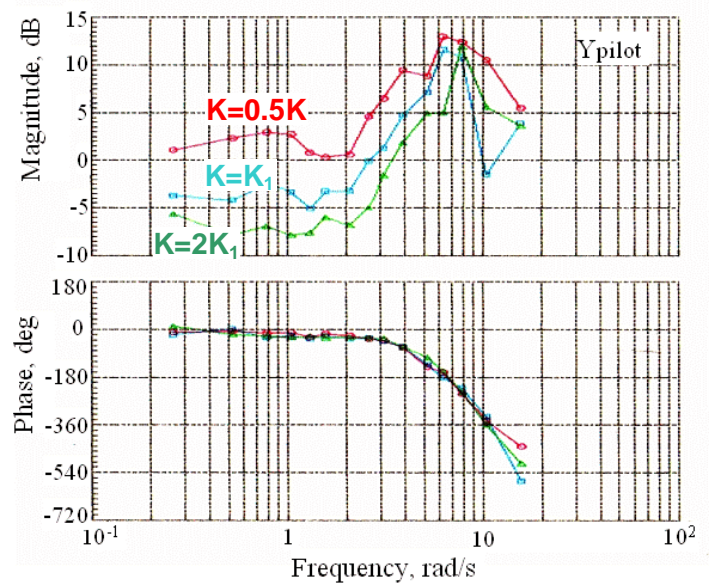


Fig.6. Effect of control sensitivity on active pilot model.

This dependence is natural. Due to the fact the inceptor is in the closed loop of biodynamic interaction (BDI) (Fig. 4), its feel system characteristics can affect the intensity of the BDI, i.e. biodynamical pilot model.

Analysis of the experimental data, received in the course of biodynamical experiments, showed the following.

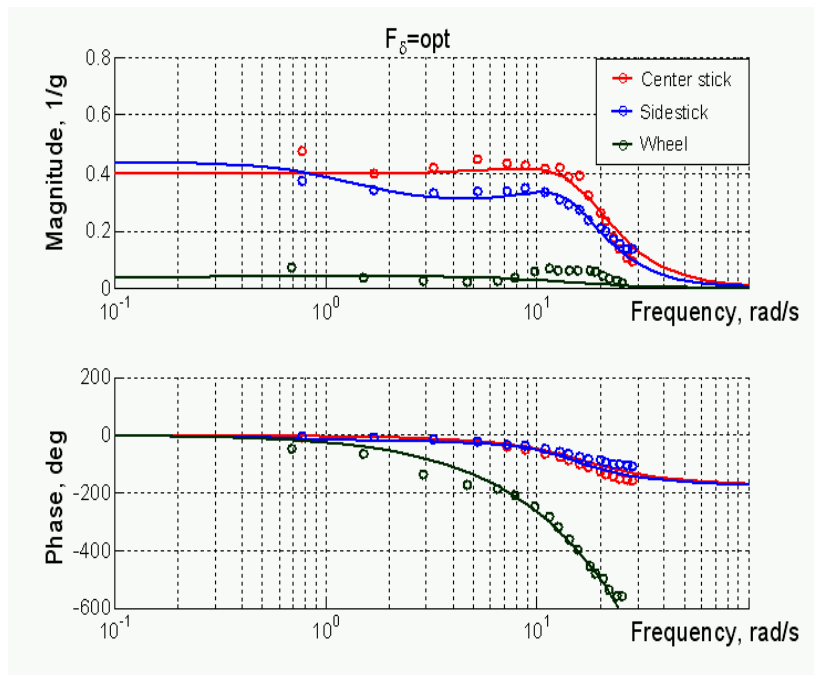


Fig.7. Effect of different types of inceptors on BDI.

- 1) Biodynamical interaction (biodynamical pilot model) depends on inceptor type. Figure 7 shows biodynamical pilot describing functions for the center stick, sidestick and wheel in terms of the inceptor involuntary displacements normalized by the maximum inceptor displacements. It is seen that in biodynamical interaction, sidestick and center sticks' displacements are almost 40 percent of their total displacement, whereas wheel displacements are only 6 percent. It means that in case of biodynamic interaction in the pilot-aircraft system, the aircraft with a wheel would provoke considerably less accelerations than aircraft with a center or side stick. (It should be mentioned that this conclusion is true only if the control sensitivity and inceptor feel system characteristics are selected optimum.)
- 2) Among other feel system characteristics, inceptor damping is the most effective method to suppress biodynamical interaction, since it considerably reduces the high-frequency component, and, at the same time, does not cause deterioration of pilot ratings of rigid-body HQ in a wide range of its variation (Fig.8.).

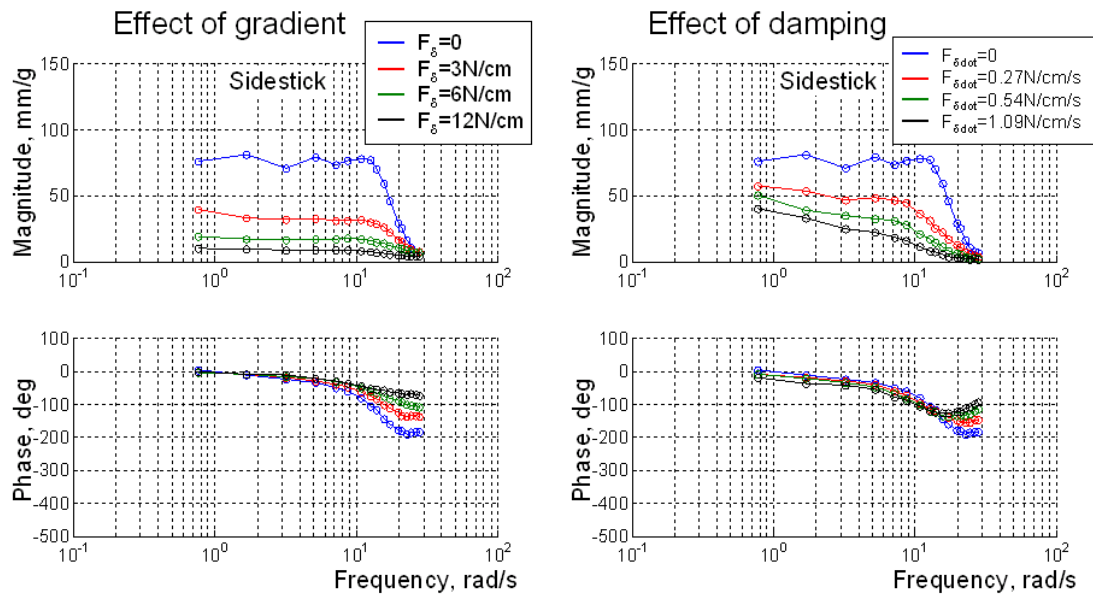


Fig.8. Effect of force gradient and damping on BDI for a sidestick.

Comparison of the calculated and experimental describing functions showed that their adequate agreement is achieved if we use the following transfer function:

$$Y_{bp}(s) = K \cdot \left( \frac{Ts+1}{T_I s+1} \right) \cdot \left[ \frac{1}{T_1^2 s^2 + 2T_1 \zeta_1 s + 1} \right]. \quad (6)$$

Gain  $K$  in Eq.(6) is a function of force gradient only. Qualitatively, the function is similar for all types of inceptors: the greater force gradient, the less gain  $K$ . Variation of other parameters in Eq.(6) depends on the inceptor type: variation of inceptor damping leads to variation of parameters  $T_1$  and  $\zeta_1$  for the sidestick, and  $T$  and  $\zeta_1$  for the center stick and the wheel, provided gain  $K$  constant. To take into account the fact the phase for the wheel is greater than for the other inceptors, a delay should be included into Eq.(6) for the wheel:  $e^{-P\tau}$ , where  $\tau = 0.35s$ . In greater detail, the adjustment rules for the coefficients in Eq.(6) for the center and side sticks are presented in [8].

At the same time, as simulator experiments have shown [7,8], pilot ratings of an elastic aircraft are almost the same regardless of the inceptor type if the roll control sensitivity and feel system characteristics (force gradient, breakout force, damping) are selected optimum (see Fig.9).

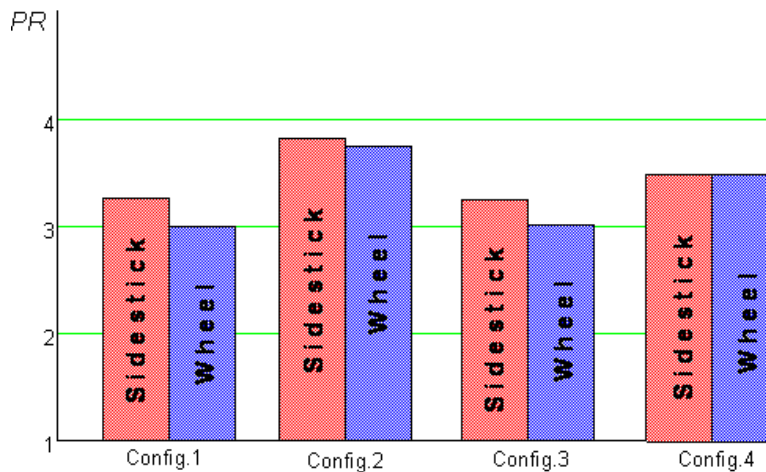


Fig.9. Pilot ratings of elastic aircraft HQ received for the wheel and sidestick for one and the same configurations of structural elasticity characteristics (feel system characteristics and control sensitivity are optimum for each of the inceptors).

This fact enables us to assume one and the same biodynamical pilot model regardless of the inceptor type to provide one and the same parameter  $\lambda$  for the considered configuration of the structural elasticity characteristics. At the same time, the selected model should allow estimation of the effect of sidestick damping.

Model (5) is proposed to calculate RMS of the lateral accelerations and parameter  $\lambda$ . For the systems with a traditional wheel, the values of parameters  $T_1$  and  $\zeta_1$  can be assumed equal  $T_1 = 0.1$  s,  $\zeta_1 = 0.7$  regardless of the feel system characteristics; for the systems with sidesticks, they are function of force damping and can be determined in accordance with functions in Fig.3.

##### 5. How was received function (1) in Fig.1?

The function was received by approximation of experimental data received and discussed in [8]. The data combine the data received for different structural elasticity characteristics, roll control sensitivity, inceptor types and feel system characteristics, see Fig.10.

Figure 10 shows pilot rating increment as a function of parameter  $\lambda$  (calculated as described above), which is, in fact, the intensity of the lateral accelerations. In the Figure, the boxes are the data for the wheel, the circles are data for the sidestick.

The effect of structural elasticity and aircraft gain is natural: as the level of structural oscillations increases, the pilot rating is getting worse.

The solid blue circles show the effect of sidestick damping. It is seen that the damping introduction contributes to  $\lambda$  reduction and to pilot rating improvement.

In the most cases in our experiments, high-frequency lateral accelerations due to structural elasticity caused biodynamical effect on aircraft handling qualities. But there were several cases when biodynamical effect switched to *interaction*, which made further piloting problematic or impossible at all, and led to dramatic pilot rating degradation (see red circles). Between the two types of inceptors considered, this is a sidestick which provoked the switching to biodynamical interaction and, as a consequence, pilot rating worsening. No one case of the biodynamical interaction was observed in experiments conducted with the wheel.

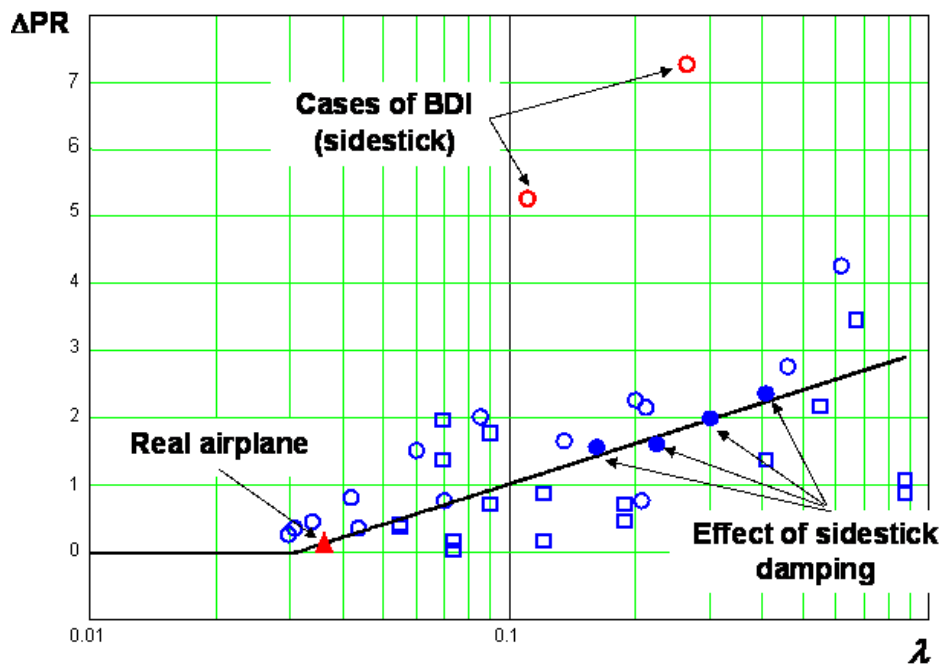


Fig.10. Experimental data (pilot rating increments) as a function of calculated parameter  $\lambda$ .

Switching from biodynamical *effect* to biodynamical *interaction* depends on a number of factors. Conducted experiments allowed us to assume type of control inceptor and acceleration level to be the triggers for the biodynamical effect to switch to interaction.

It is seen as well, that for the sidestick the tendency to biodynamical interaction becomes greater if parameter  $\lambda$  exceeds 0.1. For real airplanes, values of parameter  $\lambda$  do not usually exceed this value, i.e. parameter  $\lambda$  is within the “safe” area. In this area, the data received for the wheel and sidestick for the same structural elasticity characteristics and optimum inceptor feel system and control sensitivity characteristics are almost equal for the wheel and sidestick. In other words, for real airplanes the type of inceptor does not affect pilot rating worsening caused by lateral accelerations due to structural elasticity.

If  $\lambda < 0.02$ , lateral accelerations are not felt by the pilot (they are below the sensitivity threshold) and, thus, do not produce any negative effect on aircraft handling qualities. For  $\lambda > 0.02$  pilot ratings worsen in accordance with the logarithmic law, which is in agreement with psychophysiological law by Weber-Fechner and Stevens [10].

Figure 10 shows that the empirical function  $\Delta PR = \Delta PR(\lambda)$  adequately agrees with expression (1).

#### 4. Conclusions

- Handling quality criterion is developed which allows estimation, at the early stages of aircraft development, of the effect of the structural elasticity and other aircraft characteristics on HQ of an elastic aircraft.
- The HQ criterion is validated by experimental data received on flight simulator for the generic aircraft model with variation in a wide range of all aircraft characteristics, which

can affect HQ of an elastic aircraft: structural elasticity characteristics (number of modes, their amplitude and frequency, roll control sensitivity, control inceptor types and feel system characteristics). Good agreement between the calculated and experimental data proves the validity of mathematical expressions in the HQ criterion and all assumptions made for the pilot model transfer functions used in the criterion.

- Biodynamical experiments showed that tendency to biodynamical interaction in the pilot-aircraft system is more pronounced in the control systems with a sidestick and center stick.
- For the control systems with sidesticks, the biodynamical effect of the high-frequency accelerations caused by aircraft structural elasticity can be reduced by introduction of the additional damping into the sidestick loading system. (The conclusion can be addressed as well to the control systems with center sticks.)
- The main ideas of the developed HQ criterion can be applied to different control axes and to different types of vehicle (including rotorcraft), since it is based on the fundamental principles of pilot's perception.

## References

- [1] Rodchenko, V. V., Zaichik, L. E., Yashin, Y. P., Rufov, I. V., and White, A. D., "Theoretical Approach To Estimation of Acceleration Effects on Piloting", *AIAA Motion Simulation Technology Conference*, AIAA-2000-4292, Denver CO, 2000.
- [2] Rodchenko, V. V., Zaichik, L. E., and Yashin, Y. P., "Handling Qualities Criteria for Highly Augmented Aircraft", *Journal of Guidance, Control, and Dynamics*, Vol. 26, No.6, 2003, pp.928-934.
- [3] Rodchenko, V. V., Zaichik, L. E., Yashin, Y. P., and Lee, B.P., "Simulation – To – Flight Correlation", *AIAA Motion Simulation Technology Conference*, AIAA-5823-2003, Austin TX, 2003.
- [4] Preliminary bio-dynamical tests data analysis and critical review. ARISTOTEL Deliverable D4.2, September 2011.
- [5] Simulator test plan/matrix of the 1<sup>st</sup> test campaign. ARISTOTEL Deliverable 4.5, May 2012.
- [6] Pilot modeling for aero-servo-elastic A/RPC. ARISTOTEL Deliverable D3.6, February 2013.
- [7] Simulator test plan/matrix of the 2<sup>nd</sup> test campaign. ARISTOTEL Deliverable 4.7, February 2013.
- [8] Validation of Models and Criteria for Aeroservoelastic A/RPC Predictions. ARISTOTEL Deliverable 4.11, August 2013.
- [9] Rodchenko V.V., Zaichik L.E., Yashin Y.P., "Similarity Criteria for Manipulator Loading and Control Sensitivity Characteristics," *Journal of Guidance, Control, and Dynamics*, vol.21, No.2, 1998, pp.307-314.
- [10] "Human Physiology", Edited by R.F.Schmidt and G.Thews. London, Paris, Tokyo, 1989.